Title
Investigating the Local and High Redshift Universe With Deep Survey Data and Ground-Based Spectroscopy

Author
Masters, Daniel Charles

Publication Date
2014

Peer reviewed|Thesis/dissertation

UNIVERSITY OF CALIFORNIA
RIVERSIDE

Investigating the Local and High Redshift Universe With Deep Survey Data and Ground-Based Spectroscopy

A Dissertation submitted in partial satisfaction
of the requirements for the degree of

Doctor of Philosophy

in

Physics

by

Daniel Charles Masters

March 2014

Dissertation Committee:

Dr. Bahram Mobasher, Co-Chairperson
Dr. Patrick McCarthy, Co-Chairperson
Dr. Brian Siana

The Dissertation of Daniel Charles Masters is approved:

Committee Co-Chairperson

Committee Co-Chairperson

University of California, Riverside

Acknowledgments

I thank my advisor, Bahram Mobasher, whose sound advice guided me toward the fruitful areas of research presented here, and whose generosity and sense of humor were always appreciated. I am grateful to Patrick McCarthy for giving me the incredible opportunity to conduct a major observing campaign on Magellan, as well as for his incisive questions and suggestions from which I learned a tremendous amount. I also acknowledge the excellent support staff at the Las Campanas observatory in Chile, who made observing there a pleasure.

I am indebted to Peter Capak, who encouraged my first attempts at research, and whose optimism and seemingly endless knowledge have been a source of inspiration. I thank Brian Siana for many enlightening conversations. I also thank Mara Salvato for her enthusiasm and patience with me at the beginning of my research, and Nick Scoville for his early encouragement and support throughout my graduate work.

I am grateful for the friendship and camaraderie of my cohort of graduate students at UCR, without whom this experience would not have been nearly as fun. The FZX house parties were always a welcome diversion from the rigors of graduate work. Louis Abramson, Roozbeh Davari and Sean Johnson, my officemates at Carnegie, made coming to work a pleasure. I especially thank my wife Jessica for her patience and love, and for the many bike rides together during which the stresses of graduate school faded from mind.

This research was largely supported through generous fellowships from both the Infrared Processing and Analysis Center (IPAC) and the Carnegie Observatories, for which I am extremely grateful.

Dedicated to my family

ABSTRACT OF THE DISSERTATION

Investigating the Local and High Redshift Universe With Deep Survey Data and Ground-Based Spectroscopy

by

Daniel Charles Masters

Doctor of Philosophy, Graduate Program in Physics
University of California, Riverside, March 2014
Dr. Bahram Mobasher, Co-Chairperson
Dr. Patrick McCarthy, Co-Chairperson

Large multiwavelength surveys are now driving the frontiers of astronomical research. I describe results from my work using data from two large astronomical surveys: the Cosmic Evolution Survey (COSMOS), which has obtained deep photometric and spectroscopic data on two square degrees of the sky using many of the most powerful telescopes in the world, and the WFC3 Infrared Spectroscopic Parallels (WISP) Survey, which uses the highly sensitive slitless spectroscopic capability of the Hubble Space Telescope Wide Field Camera 3 to detect star-forming galaxies over most of the universe's history. First I describe my work on the evolution of the high-redshift quasar luminosity function, an important observational quantity constraining the growth of the supermassive black holes in the early universe. I show that the number density of faint quasars declines rapidly above $z \sim 3$. This result is discussed in the context of cosmic reionization and the coevolution of galaxies and their central black holes.

Next I present results of a multi-year campaign of near-infrared spectroscopy with FIRE, a world-class near-infrared spectrometer on the Magellan Baade 6.5 meter telescope in Chile, targeting emission-line galaxies at $z \sim 2$ discovered with the Hub-

ble Space Telescope. Our results showed that the typical emission-line galaxy at this redshift has low-metallicity, low dust obscuration, high ionization parameter, and little evidence for significant active galactic nucleus (AGN) contribution to the emission lines. We also find evidence that high redshift star-forming galaxies have enhanced nitrogen abundances. This result has interesting implications for the nature of the star formation in such galaxies – in particular, it could mean that a large fraction of such galaxies harbor substantial populations of Wolf-Rayet stars, which are massive, evolved stars ejecting large amounts of enriched matter into the interstellar medium.

Finally, I will discuss the discovery of three distant, ultracool brown dwarfs in the WISP survey. These objects, larger than massive planets but smaller than dwarf stars, are very difficult to detect, but their numbers and distribution in our galaxy have profound implications for our understanding of the formation of low-mass stars and planets. The brown dwarfs were found in the WFC3 grism spectroscopy, where they were identified through their strong atmospheric absorption features of water and methane. A systematic search for such objects in all WISP fields yielded three in total, allowing statistical inferences to be made regarding their distribution and number density in the Milky Way.

Contents

List of Figures

List of Tables

Chapter 1

Introduction

1.1 Modern surveys and their role in understanding galaxy evolution

Breakthroughs in our understanding of how galaxies form and evolve are now driven, in large part, by deep photometric and spectroscopic surveys. By observing thousands or millions of sources in a relatively uniform way, surveys enable global trends to be identified that point the way to an understanding of the physics underlying the diversity of galaxies in the universe. Modern surveys are used to study how galaxies evolve with redshift, probe large-scale structure, constrain the demographics of galaxies and active galactic nuclei (AGN), measure cosmological parameters, and discover rare objects, among other goals.

Survey designers must balance the trade-offs between sky coverage, depth, and spectral resolution for particular scientific objectives. The Sloan Digital Sky Survey (SDSS; York et al. 2000; Abazajian et al. 2009), for example, has observed over a third of the sky with imaging and fiber spectroscopy from the 2.5 meter Apache Point telescope, revolutionizing our understanding of galaxies in the local universe. By design, SDSS favors wide area and spectral resolution over depth, and thus generally does not probe galaxies in the high-redshift universe. However, the comoving volume probed by the survey, $\sim 10^8$ Mpc^3, is large enough for statistical studies of unprecedented precision in the local universe. At the other end of the survey spectrum is the Hubble Ultra-Deep Field (HUDF; Beckwith et al. 2006), an 11 arcmin^2 patch of sky in the constellation of Fornax observed to extraordinary depth with the Hubble Space Telescope (HST) Advance Camera for Surveys (ACS) and Wide Field Camera 3 (WFC3). In the composite exposure we see galaxies as far back as more than 13 billion years ago, when the universe was less than 5% its current age. The comoving volume probed in the HUDF is $\sim 3 \times 10^5$ Mpc^3, significantly lower than the SDSS. Moreover, because of its "pencil beam" design, the HUDF observes a relatively small comoving volume at any redshift, limiting its usefulness as a statistical probe of galaxy populations over cosmic time.

This thesis presents research I have done making use of data from two modern astronomical surveys: the Cosmic Evolution Survey (COSMOS; Scoville et al. 2007), a large multi-waveband survey covering two square degrees, anchored by deep HST-ACS I-band imaging, and the WFC3 Infrared Spectroscopic Parallels survey (WISP; Atek et al. 2010), which targets high-galactic latitude fields with the low-dispersion grisms on WFC3 in order to detect star-forming galaxies with minimal bias from $0.3 \lesssim z \lesssim 2.3$. For the first project presented here, I used the deep, multi-waveband data of COSMOS to probe the demographics of quasars in the distant universe. The COSMOS field strikes a balance of relatively wide area and deep observations across the electromagnetic spectrum, allowing it to probe a similar comoving volume as SDSS but extending to much higher redshifts. Thus COSMOS is uniquely well-suited to studying populations of rare, high-redshift objects such as faint quasars. For the second project, I used the sensitive grism spectroscopy of the WISP survey to select star-forming galaxies near the peak of cosmic star formation at $z \sim 2$, for ground-based spectroscopic follow-up. Each WISP pointing covers ~ 4 arcmin^2, for a comoving volume of $\sim 10^4$ Mpc^3 in which high-redshift emission-line galaxies could be discovered. This should detect roughly $5 - 10$ L^* galaxies per field, according to published luminosity functions at similar redshift. With over 300 fields observed to date, WISP provides a robust statistical sample of the star-forming galaxy population at $z \sim 2$. Our campaign of near-infrared spectroscopy with the Magellan Baade telescope in Chile allowed us to investigate the properties of galaxies at $z \sim 2$ in greater detail than possible with the HST data alone, in order to draw meaningful conclusions about their physical properties.

The final project I present grew out of the serendipitous discovery of distant brown dwarfs in the WISP survey data. After the initial discovery, we conducted a systematic search for such objects in the WISP fields and analyzed the results to constrain the distribution of brown dwarfs in our galaxy. In the following section I give short background for each of these research topics.

1.2 Background

1.2.1 Quasars in the distant universe

Quasars are the most luminous non-transient objects observed in the universe – often hundreds or thousands of times more luminous than the entire Milky Way galaxy, despite the fact that the source of the light is so small that it remains unresolved in images from even the most powerful telescopes. The tremendous energy emitted by quasars is thought to be generated by matter accreting onto a supermassive black hole at the center of the host galaxy, although the details governing this process are still not fully understood. Intriguingly, a number of lines of evidence now suggest that the quasar phase of supermassive black hole growth may influence the host galaxy substantially, and thus that galaxy and black hole evolution are closely related.

Since their discovery and identification as cosmologically distant objects, the number density of quasars as a function of redshift has been of great interest. It was shown decades ago that the number density of quasars increases dramatically with redshift (Schmidt 1968), meaning that quasar activity was much higher in the past. Later research of bright optical and X-ray selected AGN revealed that this trend eventually ends, with a peak in quasar activity around $z \sim 2$ and a decline in number density to higher redshifts. It is now known that these trends mirror the global star formation history (Madau et al. 1998), again suggesting an evolutionary link between galaxies and the black holes at their centers.

Besides having potentially profound implications for galaxy formation, these trends also relate to another important question in modern astrophysics: What was responsible for reionizing the universe around $z \simeq 6 - 10$? The observed decline of bright quasars above $z \sim 2 - 3$ has been taken as evidence that AGN do not contribute significantly to reionization (Fan et al. 2001), but until recently the question of whether the number density of faint quasars increases or decreases at $z \gtrsim 4$ has not been explored, due to the observational difficulties associated with constraining a population of rare, faint sources. New surveys going deeper over larger areas are allowing the population of faint AGN at high redshift to be investigated for the first time.

1.2.2 High-redshift starbursting galaxies

High redshift ($z \gtrsim 1$) galaxies only became accessible for study in the last two decades, primarily with the advent of the Hubble Space Telescope and the discovery of techniques to reliably identify high-redshift objects (e.g., Madau et al. 1996; Steidel et al. 1996). Because these galaxies are seen as they were billions of years ago, they give direct insight into the nature of galaxies at much earlier stages of their evolution, at a time when the global star-formation rate was significantly higher and galaxies were still actively forming. The physical properties of galaxies at high-redshift are valuable clues as to how galaxies evolved into the diverse, stable forms seen in the local universe.

The Wide Field Camera 3 on HST, which was installed during Servicing Mission 4 in May 2009, has accelerated the discovery of high redshift galaxies dramatically, for two primary reasons. First, the sensitive, high-resolution near-infrared imaging capability of WFC3 allows dropout galaxies at $z > 7$ to be robustly identified. Second, WFC3 slitless grism spectroscopy is extremely sensitive to galaxies with emission lines at $z \sim 1 - 2$, filling in an important search space that has historically been difficult to probe in an unbiased way with ground-based telescopes.

Much effort is now being spent trying to understand the population of high-redshift galaxies. Questions that are being investigated range from the nature of the interstellar medium (ISM) at this epoch, the role of galaxy environment in triggering or suppressing star formation, the relative importance of mergers for galaxy growth, to what extent stellar and/or AGN feedback regulate star formation, how quiescent galaxies formed at early epochs, and how the intergalactic medium (IGM) interacts with and is chemically enriched by galaxies. The limits of current instrumentation are being reached in an effort to answer these questions. The next generation of large ground- and space-based telescopes – for example, the Giant Magellan Telescope (GMT), the Thirty Meter Telescope (TMT), and the James Webb Space Telescope (JWST) – will certainly advance our knowledge of the high-redshift universe dramatically.

1.2.3 Substellar objects in the Milky Way

Brown dwarfs are failed stars, typically larger than giant planets but smaller than dwarf stars. They do not produce nuclear energy through hydrogen fusion and thus cool continuously after their formation. Thermal (infrared) radiation from their atmospheres is the only signal (other than gravitation) by which they can be detected directly. Only in the last decade or so have significant numbers of cool brown dwarfs been found (Kirkpatrick et al. 2011).

Cool brown dwarfs are of interest for a number of reasons. Dwarfs stars never return material to the ISM, and thus are "fossils" recording the elemental abundances of the material from which they formed. This property can be used the study the early chemical enrichment of our galaxy. Ultracool subdwarfs, a class of very cool and metal-deficient dwarfs, generally have halo kinematics and are thought to have formed very early in the Milky Way's history, making them particularly intriguing as probes of this epoch (Burgasser 2008). Brown dwarfs are, therefore, indirectly relevant to our understanding the high redshift universe. Moreover, brown dwarfs may represent the most common interlopers in searches for high redshift quasars (e.g., Caballero et al. 2008), so developing a detailed understanding of their properties and distribution in our galaxy is important for direct investigations of the high redshift universe as well.

The detailed physics governing star formation is still not well understood, and significant debates remain regarding the shape of initial mass function (IMF) of star formation and whether or not it changes in different star-forming conditions. The distribution of cool brown dwarfs in our galaxy is a vital clue regarding the behavior of the low-mass end of the initial mass function. Moreover, the coolest dwarf stars can be used to understand the atmospheres of giant exoplanets, many of which have been discovered due to the phenomenal success of the Kepler mission. These planets are difficult to study directly because of the interfering light from their host stars (Barman et al. 2005), so comparably-sized brown dwarfs may prove very useful as analogues.

1.3 Outline of the dissertation

I will first present my determination of the high redshift quasar luminosity function using data from the COSMOS survey field. This work combined the extensive photometric and spectroscopic data of COSMOS to show that the space density of faint quasars decreases rapidly above $z = 3$. In combination with other results, such as the high redshift X-ray luminosity function, and the QLF from SDSS, the result I present here strongly suggests that all AGN activity declines rapidly for $z \gtrsim 3$, although a significant fraction of AGN at high redshift may be optically obcured. This result has implications both for the early co-evolution for AGN and galaxies, as well as the contribution of AGN activity to the ionizing background at the epoch of reionization.

In the second part of the thesis I present results from a campaign of follow-up near-infrared spectroscopy of emission-line galaxies at $z \sim 2$. The galaxies were selected from the WISP survey based on strong rest-frame optical emission lines, and follow-up spectroscopy was performed with a state-of-the-art infrared spectrometer on the Magellan Baade 6.5 meter telescope in Chile. I discuss the global properties of the galaxies derived from our extensive follow-up campaign, including dust obscuration, metallicity, star formation rates, ionization parameters, and kinematics, as derived from the rest-frame optical spectroscopy. I present evidence that most such galaxies have little evidence for AGN activity, but that they do have higher ionization parameters than found in most star-forming regions in the local universe, indicating that the star-forming conditions are different at high redshift. I also discuss a possible nitrogen enhancement detected in the galaxies, which might explain some well-known differences of high redshift star-forming galaxies in comparison with their local counterparts in a classic diagnostic diagram. We interpret the nitrogen enhancement as being a result of large numbers of Wolf-Rayet stars in dense super star clusters in such galaxies.

In the last part of the thesis I present a study of distant brown dwarfs discovered in the WISP survey. I describe the serendipitous discovery of the first brown dwarf in the WFC3 data and the subsequent search for additional brown dwarfs, which resulted in the discovery of three ultracool T dwarfs in the WFC3 grism data. These three dwarfs, including the most distant T dwarf known, were used to place constraints on the space density and distribution of such objects in our galaxy.

The chapters in this dissertation are adapted from articles that have been or are in the process of being published in the Astrophysical Journal (ApJ). Chapter 2 is adapted from Masters et al. 2012b (ApJ, 755, 169) and Chapter 4 is adapted from Masters et al. 2012a (ApJ, 752, L14). Chapter 3 has been accepted by ApJ and is currently in press. In the appendix I describe a software routine, SpecPro, that I developed to aid in the analysis of astronomical spectra. This work was published in the Proceedings of the Astronomical Society of the Pacific (PASP) journal (Masters & Capak, PASP, 123, 638).

Chapter 2

The High-Redshift Quasar Luminosity Function

2.1 Introduction

Supermassive black holes are now known to reside at the centers of virtually all galaxies (Kormendy & Richstone 1995; Ho et al. 1997; Magorrian et al. 1998; Ho 2008). While mostly dormant in the local universe, the energetic growth of black holes is on display at high redshifts in the powerful radiation of active galactic nuclei (AGN). The most luminous AGN – the quasars – were first recognized as cosmologically distant objects by Maarten Schmidt in the 1960s (Schmidt 1963, 1968). Characterizing the demographics and space evolution of AGN has been an active and important area of research since then (see, for example, Koo & Kron 1982, Boyle et al. 1988, Hartwick & Schade 1990, Richards et al. 2006 and references therein). In recent years the study of quasar evolution has taken on new importance as strong correlations between black holes and the galaxies that host them have been discovered (Ferrarese & Merritt 2000; Gebhardt et al. 2000; Wyithe & Loeb 2003), and as feedback from quasars on their host galaxies has been identified as a potentially crucial mechanism regulating the growth of galaxies (Benson et al. 2003; Bower et al. 2006; Hopkins et al. 2006; McNamara & Nulsen 2007).

The main observational quantity used to study quasar demographics is the quasar luminosity function (QLF), defined as the comoving space density of quasars as a function of intrinsic luminosity. The QLF is a fundamental cosmological measurement of mass assembly in the universe, as the evolution of the QLF with redshift directly constrains the growth of supermassive black holes (SMBHs) over cosmic time (Richstone et al. 1998; Kauffmann & Haehnelt 2000; Yu & Tremaine 2002; Wyithe & Loeb 2003; Marconi et al. 2004). Changes in the shape and normalization of the QLF reflect the duty cycles of quasars, the growth history of SMBHs, and the coevolution of black holes and their host galaxies (Hopkins et al. 2006, Ueda et al. 2003 and references therein).

At low redshifts ($z \lesssim 2$) the QLF is found to be well-described by a double power law of the form:

$$\Phi(M, z) = \frac{\Phi(M^*)}{10^{0.4(\alpha+1)(M-M^*)} + 10^{0.4(\beta+1)(M-M^*)}} \quad (2.1)$$

where $\Phi(M^*)$ is the normalization, M^* is the break luminosity between the bright and faint ends, α is the bright-end slope and β is the faint-end slope (Boyle et al. 1988). The bright-end slope α and the normalization $\Phi(M^*)$ have been well-constrained out to $z \sim 5$ (Richards et al. 2006) using photometric and spectroscopic data from the Sloan Digital Sky Survey (SDSS; Abazajian et al. 2009). However, the break luminosity and faint-end slope β can not be constrained at high redshifts with SDSS due to the magnitude limit of the survey.

The QLF can be integrated to give the cumulative ionizing background radiation from quasars at a given redshift. The faint-end slope β and break luminosity M^*

of the QLF at high redshift are of particular interest in this regard, because the total ionizing background from quasars strongly depends on their values. The peak in quasar activity around $z \sim 2-3$ is known to be responsible for HeII reionization at $z \sim 3$ (Reimers et al. 1997; Sokasian et al. 2002), but the relative contribution of quasars to hydrogen reionization at $z \sim 6-10$ is not as well constrained. The observed decline in space density of highly luminous quasars at $z > 3$ has been taken as evidence that quasars contribute negligibly to hydrogen reionization (Madau et al. 1999; Fan et al. 2006); however, because only the most luminous quasars at $z \gtrsim 4$ can be found in surveys such as SDSS, the contribution of faint quasars to the ionizing background has been uncertain.

Recent years have seen the advent of the first surveys that combine the required depth and sky coverage to probe the faint end of the QLF above $z = 3$. One of the first studies to probe the faint end of the QLF at $z \sim 4$ was presented in Glikman et al. (2010). This group used high-quality subregions of the Deep Lens Survey (DLS, Wittman et al. 2002) and NOAO Deep Wide-Field Survey (NDWFS, Jannuzi & Dey 1999) fields, with a combined sky coverage of 3.76 deg^2, to search for quasars using a color selection technique to a limiting AB depth of $R = 23$ mag. The candidate quasars found in these fields were followed up with optical spectroscopy with the Low-Resolution Imaging Spectrometer (LRIS; Oke et al. 1995) on the Keck I telescope to confirm high redshift quasars and determine the level of contamination in the sample. A surprising result was found: the QLF measured in this work showed essentially no break between the bright and faint ends, as found at lower redshifts. This result was unexpected, and if verified would have profound implications for the early growth of black holes and the contribution of quasars to hydrogen reionization.

Glikman et al. (2011) (hereafter G11) presented further LRIS spectroscopy of quasar candidates that resulted in a significant downward revision in the faint-end QLF presented in Glikman et al. (2010). A break luminosity of $M^* = -24.1^{+0.7}_{-1.9}$ was found in this work, with a faint-end slope $\beta = -1.6^{+0.8}_{-0.6}$. Nevertheless, the $z \sim 4$ QLF presented in G11 displayed a high normalization, suggesting that little evolution occurs in the number density of faint quasars from $z \sim 3$ to $z \sim 4$. Such a trend would run counter to what is found for more luminous quasars and X-ray luminous high-redshift sources.

Another investigation of the QLF at $z \sim 4$ was conducted by Ikeda et al. 2011 (hereafter I11) using the HST-ACS region of the COSMOS field (Scoville et al. 2007) with a sky coverage of 1.64 deg^2. Ikeda et al. employed a quasar color selection using the COSMOS photometry, and further required candidates to be point-like in *HST*-ACS imaging, since quasars dominate the light of their host galaxies at high redshift. I11 found a faint-end slope β of $-1.67^{+0.11}_{-0.17}$, in agreement with the revised estimate of G11. However, I11 found a substantially lower normalization of the faint end QLF – in other words, a much lower absolute space density of faint quasars at $z \sim 4$, by roughly a factor of four. The discrepancy between QLFs derived by the two groups is too large to be attributed to cosmic variance given the comoving volumes probed, and the two results point to different pictures of quasar evolution. The result of G11 implies that the decline in the space density of faint quasars with redshift at high redshift is significantly slower than what is observed for bright quasars, perhaps indicating that the contribution of faint quasars to cosmic reionization is significant, while the result of I11 indicates a rapid decline in the number of faint quasars above $z = 3$.

Both I11 and G11 use broad-band optical color selection to identify quasars. A major uncertainty in this approach is the selection function, or the fraction of quasars that are selected as a function of redshift and magnitude. The selection function is determined with Monte Carlo simulations, which are sensitive to the assumed distribution of quasar spectral energy distributions (SEDs) in the survey field. This distribution is uncertain, and mismatches between the assumed and actual distributions can give rise to errors in completeness estimation and thus the derived luminosity function. In addition to selection function uncertainty, contamination from stars and galaxies can be substantial and difficult to quantify. Spectroscopy allows a robust determination of the contamination, but due to the large amount of telescope time required, often only a subset of the candidates can be observed, and extrapolating to the complete sample can be problematic. This is particularly true if the success rate of the spectroscopic follow-up depends on magnitude.

Here we develop an alternative approach, using the COSMOS survey data to select and identify high-redshift quasars with high completeness and low contamination. Our principal goals are to (1) determine the faint end of the QLF from $3.1 < z < 5$ in COSMOS, thereby providing an independent check of the result reported by I11, as well as a direct determination of the evolution of the faint-end over this redshift range, (2) compare the rest–frame UV quasar luminosity function with the rest-frame 2-10 keV X-ray luminosity function for sources at $z > 3$ in order to investigate the obscured fraction of bright AGN at these redshifts, and (3) use our results to make inferences regarding the evolution of the QLF and the likely contribution of quasars to reionization, both of HeII at $z \sim 3$ and HI at $z \sim 6 - 10$.

This chapter is based on Masters et al. (2012b) and is structured as follows. In § 2.2 we discuss the COSMOS survey in some detail, as background for the analysis that follows. In § 2.3 we provide an overview of the method used to determine the QLF, and present our quasar selection technique and its completeness and reliability. In § 2.4 we discuss the X-ray properties of the selected objects. In § 2.5 we compute the luminosity function at $z \sim 3.2$ and $z \sim 4$ with the sample. In § 2.6 we discuss sources of error that may influence our results. In § 2.7 we compare the X-ray and UV luminosity functions at $3 \lesssim z \lesssim 5$ and discuss the implications for the obscured fraction of quasars at these redshifts. In § 2.8 we discuss the ionizing background due to quasars, and in § 2.9 we summarize our main conclusions. We assume a cosmology with $\Omega_\Lambda = 0.7$, $\Omega_M = 0.3$, and $H_0 = 70$ km s^{-1} Mpc^{-1}. Magnitudes are in the AB system.

2.2 The COSMOS survey

The Cosmic Evolution Survey (COSMOS, (Scoville et al. 2007)) is one of the most ambitious photometric and spectroscopic surveys ever conducted. Built around very deep, high-resolution Hubble Space Telescope Advanced Camera for Surveys HST-ACS I-band imaging of a 2 deg^2 equatorial patch of sky, the COSMOS field has been followed up extensively with many of the best ground– and space–based observatories in the world. The combination of depth, relatively large area, and observations spanning the electromagnetic spectrum in COSMOS enable detailed study of galaxy evolution and the growth of structure across cosmic time. Moreover, these features make COSMOS an appropriate field for investigating the evolution of AGN to high redshift, where it is necessary to search a large comoving volume to minimize the effects of cosmic variance. Here we give a brief overview of the data of the COSMOS survey.

2.2.1 Photometric data

The COSMOS survey is anchored by extremely deep (point source depth of $I_{\rm AB}$=28) HST-ACS imaging covering 1.64 deg^2 at a resolution of $0.05''$ with the F814W filter. The high resolution and depth of the HST I-band imaging enables detailed morphological study of galaxies, detection of mergers, and weak gravitational lensing measurements tracing the growth of dark matter structure (e.g., Massey et al. 2007; Scarlata et al. 2007; Sheth et al. 2008; Scoville et al. 2013). The field has been followed up with many of the best telescopes in the world, including: X-ray from 0.5-7 keV with the Chandra space telescope and shallower X-ray data from XMM-Newton; near-UV (135-175nm and 175-280nm) with the Galaxy Evolution Explorer (GALEX) space telescope; UV from Mega-Prime on the Canada-France-Hawaii Telescope (CFHT); optical narrow and intermediate band photometry with Suprime-Cam on the Subaru 8.3 meter telescope; near-infrared from WIRCAM on the CFHT, WF-CAM on the United Kingdom Infrared Telescope (UKIRT), NEWFIRM on the Cerro Tololo Inter-American Observatory (CTIO) and UltraVista on the VISTA survey telescope; infrared from the Infrared Array Camera (IRAC) and the Multiband Imaging Photometer (MIPS), both on the Spitzer Space Telescope; submillimeter from the Herschel Space Observatory and SCUBA2 on the James Clerk Maxwell Telescope; and radio with the Very Large Array (VLA). The well-matched photometry spanning the electromagnetic spectrum gives an unprecedented view of galaxies, enabling the determination of highly accurate photometric redshifts (Mobasher et al. 2007; Salvato et al. 2009; Ilbert et al. 2009) and detailed galaxy properties such as mass, star formation rate (SFR), and dust obscuration (Pannella et al. 2009; Ilbert et al. 2010; Karim et al. 2011). Both the accurate photometric redshifts and well-constrained morphologies are important elements of our approach to investigating the QLF at high redshift.

2.2.2 Spectroscopic data

In addition to the extensive multiwaveband imaging in COSMOS, spectroscopic campaigns have been conducted in the field for a wide range of scientific investigations. The largest such program is zCOSMOS (Lilly et al. 2007). This survey, conducted with the VIMOS spectrograph on the 8 meter VLT, consists of a "bright" sample of ∼20,000 galaxies from $0.1 \lesssim z \lesssim 1.2$ with $I_{AB} < 22.5$, and a "deep" sample of ∼10,000 galaxies with photometric redshifts of $1.4 \lesssim z \lesssim 3.0$. A further spectroscopic campaign, primarily targeting XMM-Newton detected AGN candidates in COSMOS, was conducted from 2005-2007 using the Inamori-Magellan Areal Camera & Spectrograph (IMACS) on the Magellan Baade 6.5 meter telescope in Chile (Trump et al. 2009). This survey resulted in 485 high–confidence redshifts. Spectroscopy of more than 4000 sources from COSMOS, including AGN candidates and high redshift Lyα emitters, was also obtained in a series of observing runs with the DEIMOS spectrometer on the Keck II telescope over 2007-2010. Spectroscopy specifically targeting high-redshift quasar candidates was undertaken using the Faint Object Camera and Spectrograph (FOCAS) on the Subaru 8.2 meter telescope (Ikeda et al. 2011, 2012). Finally, SDSS overlaps the COSMOS field and has obtained independent fibre-fed spectra of a number of objects in the field with the 2.5 meter Sloan telescope at Apache Point. These spectroscopic surveys were searched exhaustively for known high redshift quasars in the work presented here. This sample represents the known quasars; our goal is to use the extensive photometry of COSMOS in conjunction with the confirmed high–z quasars to constrain the total population.

2.3 Quasar candidate selection

2.3.1 Methodology

We utilize the COSMOS broad, intermediate, and narrow band photometric catalog (Capak et al. 2007; Sanders et al. 2007) for the selection of quasars and identification of contaminants. With 29 bands of well-matched photometry, these data constitute low-resolution spectra for all objects over the wavelength range 0.1-8μm (Figure

2.1), which is generally sufficient to distinguish stars from high-redshift quasars. With spectra of sufficient quality for all sources in the field, the population of quasars can be well-constrained down to the limiting magnitude. Our approach is similar to that of Wolf et al. (2003), who used the 17 filters (5 broad and 12 intermediate band) of the COMBO-17 survey to identify quasars. COSMOS is of similar resolution to the COMBO-17 survey in the optical, but significantly deeper and covering a wider wavelength range.

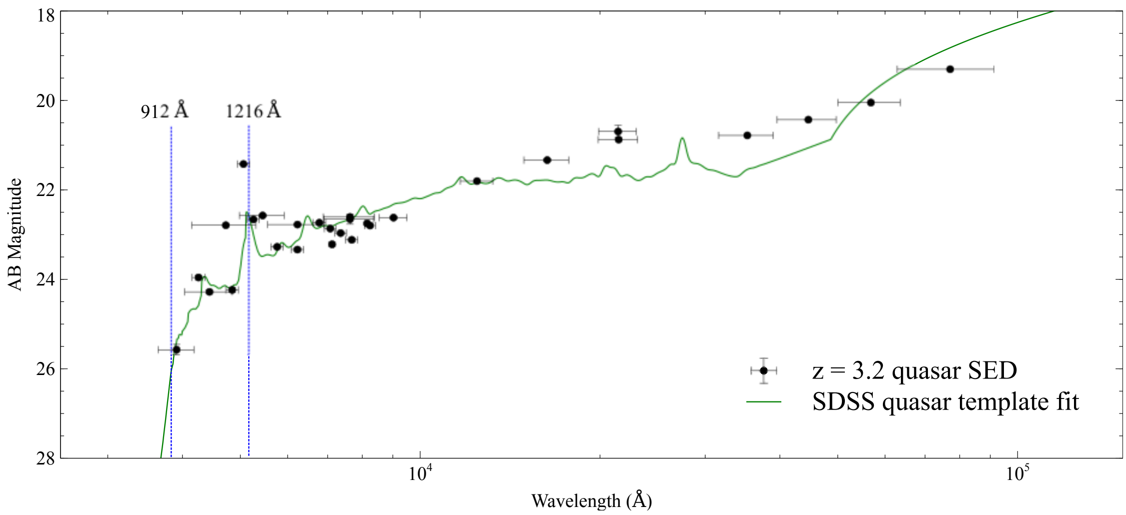

Figure 2.1 This confirmed quasar at redshift $z = 3.2$ illustrates the quality of the low-resolution spectrum afforded by the COSMOS photometric data. Filter bandwidth is indicated with horizontal bars. The observed-frame positions of the Lyman break and Lyman limit are indicated with vertical blue lines. Overlaid is a typical QSO spectral template (Vanden Berk et al. 2001). Features of a high-redshift quasar SED are clear in the photometry, including the Lyman break at rest-frame 1216Å, Lyα emission, broad quasar emission lines, and the rising SED into the observed-frame infrared.

Because neither the properties of the faint, high-redshift quasar population nor the properties of the contaminating stellar population are very well constrained, we individually inspect the spectral energy distributions and imaging data to identify quasars and reject contaminants, as described in § 2.3.4. To ensure that our classifications are unbiased, we also cross-check against automated χ^2 fitting of model SEDs to the low resolution spectro-photometry of COSMOS (§ 2.3.6). The two methods produce similar results, but we argue the visual classification is more accurate because it allows for a broader range of quasar properties as well as the identification of photometry errors that can influence the χ^2 result. The method we use can be summarized as follows:

1. Find a coarse selection (based on point-source morphology, the presence of a Lyman-break, and a power law infrared slope) that is highly complete for type-1 quasars at $z \sim 3-5$, sacrificing reliability to the extent necessary to achieve high completeness.

2. Assess the 29-band photometric and imaging data for each candidate to remove contaminants.

3. Cross-check the resulting quasar list with known high-redshift quasars in COSMOS to confirm our ability to recover quasars with high completeness.

4. Compute the luminosity function with the resulting sample.

Several factors specific to the COSMOS field make this approach reasonable. We list these below.

- Over 40 confirmed $z > 3$ quasars are known in COSMOS, which were selected in different ways (X-ray, infrared, optical). These quasars serve as a guide in developing our selection criteria, and provide an important check on our ability to distinguish quasars from contaminants using photometric and imaging data.

- A large spectroscopic sample of faint AGN and galaxy candidates obtained by the Keck, VLT, Subaru and Magellan telescopes can be used to test contamination.

- High-resolution imaging of the COSMOS field with the HST lets us restrict our sample to true point sources, limiting the contamination from high-redshift star-forming galaxies.

- Accurate photometric redshifts (Ilbert et al. 2009; Salvato et al. 2009) can be used for sources lacking spectroscopic confirmation.

- Deep Chandra X-ray imaging of the central 0.9 deg^2 of the COSMOS field allows another check on the completeness and reliability of our approach, and also permits a comparison of our estimated QLF with the X-ray luminosity function at similar redshifts. We present this analysis in § 2.7.

2.3.2 Selection procedure

Spectroscopic campaigns have confirmed over 40 quasars at $z > 3$ in the COSMOS field. These known quasars were originally selected in different ways (X-ray, infrared, optical) and therefore display a range of SEDs. The confirmed sources are used to guide the development of a coarse initial selection, which is then tested for completeness with simulated quasar photometry, as described in § 2.3.3.

It is worth emphasizing that the selection presented here is intended only to be a weak filter against contamination, in order to reduce the number of candidates to a reasonable number while maintaining high completeness. The careful rejection of contaminants occurs later through inspection of the photometric and imaging data, as described in § 2.3.4.

We begin by selecting point sources in the magnitude range $16 \leq I \leq 25$, restricting our study to the region of COSMOS covered by ACS imaging (1.64 deg^2). Spatially extended sources as defined in the Hubble Advanced Camera for Surveys (ACS) catalog of Leauthaud et al. (2007) are excluded. The test for point morphology is based on the ratio of the peak surface brightness (MU_MAX) to the magnitude (MAG_AUTO), and exploits the fact that the light distribution of a point source scales with its magnitude. The point source selection is shown to be robust to $I = 25$, which sets the magnitude limit for our search. 22383 candidates meet this selection criterion.

Next we use the χ^2 parameter, computed through template fitting in the COSMOS photometric redshift catalog, to separate stars from quasars. The *Le Phare* code (Arnouts & Ilbert 2011) was used to determine photometric redshifts (see Ilbert et al. 2009 for details). As a result of extensive fitting against templates, sources are assigned three χ^2 values: χ^2_{gal}, χ^2_{qso}, and χ^2_{star}, which are computed by fitting galaxy, AGN, and stellar templates, respectively, to the source photometry. Because we restrict our search to point sources, a comparison between χ^2_{qso} and χ^2_{star} can distinguish most stars from quasars. As seen in Figure 2.2, the relaxed cut $\chi^2_{qso}/\chi^2_{star} \leq 2.0$ selects all known $z > 3$ quasars, while rejecting the majority of stars. This leaves us with 8125 candidates.

The effectiveness of χ^2 fitting is due to two main factors. One is the COSMOS intermediate band data, which can differentiate sharp features such as the Lyman break and emission features in quasar photometry from the smooth photometry of stars. The other (more important) factor is Spitzer IRAC photometry. Stars display Rayleigh-Jeans black body curves that decline in the infrared, whereas high redshift quasars

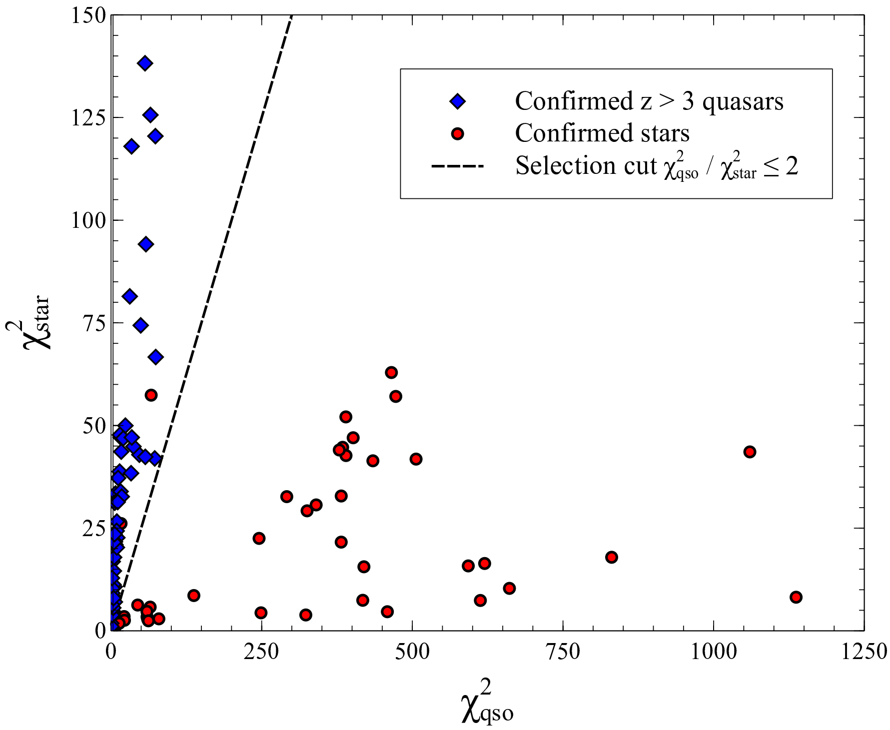

Figure 2.2 Comparison of the minimum χ^2 values for QSO and star template fitting to the COSMOS photometry of point sources with spectra. The cut shown selects objects with $\chi^2_{qso}/\chi^2_{star} \leq 2.0$, which retains all known $z > 3$ quasars while rejecting a significant fraction of stars. The spectroscopically confirmed stars shown here are primarily F, M, L, and T dwarfs, which are typical contaminants in high-redshift quasar searches (Caballero et al. 2008; Richards et al. 2009).

display power law SEDs that are flat or rising in the infrared.

Next we apply a cut designed to select high-redshift quasars. The Lyman break, caused by the scattering of radiation at wavelengths shorter than 1216 Å by neutral hydrogen in the IGM and quasar host galaxy, results in a reduction in U band flux for quasars at $z \gtrsim 3.1$. In the mid-infrared, however, high redshift quasars remain relatively bright due to their intrinsic power law spectral slopes. Therefore, we accept sources meeting either of the following cuts: $U - \text{ch1} \geq 1.5$ or $U - \text{ch2} \geq 1.5$. Here ch1 and ch2 refer to Spitzer IRAC channel 1 (3.6μm) and channel 2 (4.5μm). These cuts were motivated by the spectroscopically confirmed sample as well as simulated quasar spectra, and are significantly relaxed in order to achieve high completeness. While the cuts are not significantly different, we accept sources meeting either one in order to avoid losing quasars with bad IRAC photometry in one of the bands. This leaves 6667 candidates. To safeguard against losing unusual quasars, we also accept sources with photometric redshifts $z_{qso} \geq 3$. This adds 28 candidates, for a total of 6695 candidates after this step.

Finally, we require that the source is detected at a significant level ($m_{AB} \leq 24.0$) in either IRAC channel 1 or channel 2. Because quasar SEDs typically rise into the infrared, this condition will be met by the majority of quasars with $I < 25$, while it serves to eliminate faint stars or other unexpected contaminants. The final number of candidates after applying this selection is 4009.

This selection, by utilizing only the Lyman continuum break and power law infrared emission of high-redshift quasars, largely avoids the uncertainties associated with broad-band color selection. Color selections in the rest-frame optical must correctly account for intrinsic quasar SEDs that can vary substantially in spectral slope and broad line emission equivalent widths, the distributions of which are not well constrained at high redshift. In addition, the selection used here should be sensitive to broad absorption line (BAL) quasars, which show similar mid-infrared to optical luminosity ratios as non-BALs (Gallagher et al. 2007).

To summarize, the initial coarse selection we use is:

1. $16 < I(\text{mag\_auto}) < 25$

2. Point source based on ACS I-band imaging

3. $\chi^2_{qso}/\chi^2_{star} \leq 2.0$

4. $U - \mathrm{ch1} \geq 1.5$ OR $U - \mathrm{ch2} \geq 1.5$ OR $z_{qso} \geq 3.0$

5. $m_{AB}(3.6\mu\mathrm{m}) \leq 24.0$ OR $m_{AB}(4.5\mu\mathrm{m}) \leq 24.0$

The 4009 candidates selected include all 39 known $z \geq 3.1$ quasars in COSMOS.

A comparison of our selection with the high-redshift X-ray sources reported in Civano et al. (2011) confirms that we select all high redshift X-ray sources with $I \leq 25$ and point morphology (27 total). The other 74 sources in the X-ray $z > 3$ sample are primarily classified as extended (90%), or lie outside our I-band magnitude limit, or both. Keck DEIMOS spectra (Capak et al., in preparation) of 12 of the extended $z > 3$ X-ray sources confirms that these are obscured, type-2 AGN without broad emission lines, and therefore not appropriate to include in this work.

These pieces of evidence indicate that the selection outlined above is highly complete for unobscured quasars at $z > 3.1$. This is verified using simulated quasar photometry, as described in the next section.

2.3.3 Selection completeness

We follow the standard procedure of testing the selection by simulating a large number of quasars in redshift/magnitude space. We use the three composite spectral templates QSO1, TQSO1, and BQSO1 from the SWIRE template library (Polletta et al. 2007), each representing a different infrared/optical flux ratio, and extend them into the far-UV using the composite HST spectral template of Telfer et al. (2002). By letting the intrinsic spectral slopes for $\lambda > 1216$ Å and $\lambda < 1216$ Å vary randomly according to the distributions given in Vanden Berk et al. (2001) and Telfer et al. (2002), we generate 50 QSO1 templates and 25 each of the TQSO1 and BQSO1 templates. These 100 base templates are checked against the photometry of known quasars in SDSS, including IRAC photometry for quasars in the Spitzer Heritage Archive (Teplitz et al. 2012), to verify that they are representative of the underlying variation in the population of type-1 quasars.

We create a grid in redshift and I magnitude, with the redshift extending from $3 \leq z \leq 5$ in steps of $\Delta z = 0.1$ and the I band magnitude extending from $20 \leq I \leq 26$ in steps of $\Delta I = 0.1$. At each point in this grid we generate 20 realizations of each of the 100 model quasar templates, adding Poisson and background noise to the measured flux in each filter, and correcting for intergalactic extinction using the model of Madau (1995). The selection criteria (4) and (5) are then applied to each of the 2000 resulting SEDs to determine the completeness at that grid point.

The result is shown in Figure 2.3. For $I < 23.8$, the completeness is >90% over the redshift range $3.1 < z < 3.3$ and ∼100% at higher redshifts. The marginal incompleteness for $3.1 \lesssim z \lesssim 3.3$ will be improved by the additional inclusion of sources with $z_{qso} > 3$ in criterion (4). There is some incompleteness for $23.8 < I < 25$ due to criterion (5), which is accounted for when computing the luminosity function.

Figure 2.3 demonstrates that the photometric criteria (4) and (5) are highly complete, but it does not account for possible incompleteness introduced by criteria (2) and (3). We briefly discuss the effect these may have.

The third selection criterion ($\chi^2_{qso}/\chi^2_{star} \leq 2.0$) is based on the results of extensive fitting of the COSMOS sources against spectral templates. Checking this criterion with our modeled quasar templates would not be very revealing, as it would constitute checking simulated photometry against simulated photometry. However, the evidence in Figure 2.2 gives us confidence that this very relaxed criterion introduces negligible

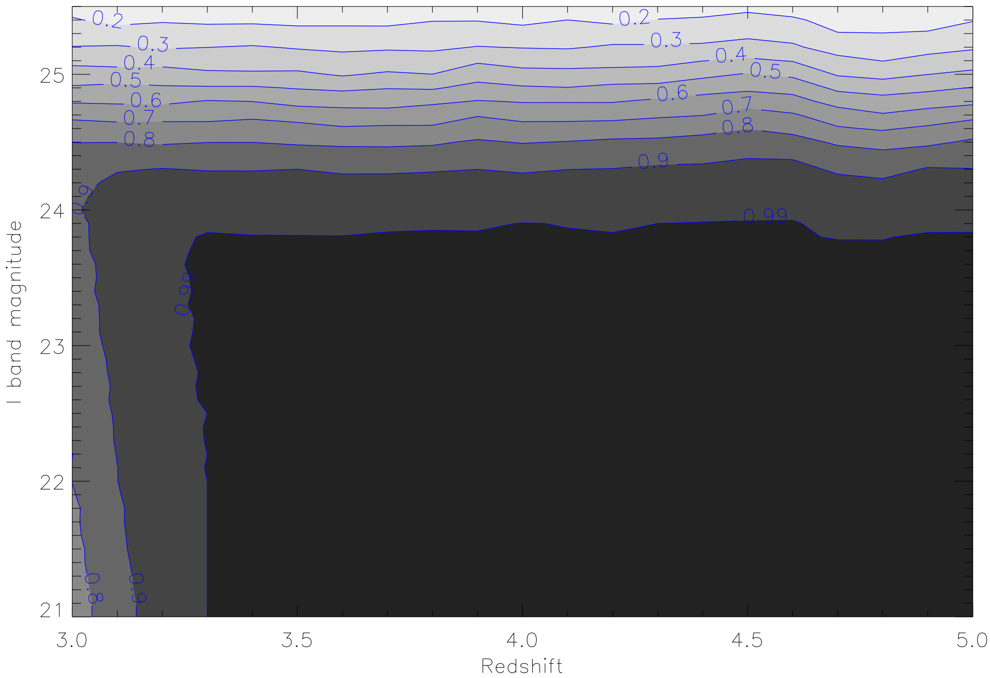

Figure 2.3 Completeness map for our photometric selection. For magnitudes brighter than $I \sim 24$, the selection is over 90% complete over the redshift range $3.1 \lesssim z \lesssim 3.3$ and ∼100% complete at higher redshifts. Because we also accept all sources with $z_{qso} \geq 3$, the completeness from $3.1 \lesssim z \lesssim 3.3$ will be enhanced over what is shown. At I-band magnitudes fainter than $I \sim 24$ there is some incompleteness due to criterion (5), which is accounted for in computing the luminosity function.

incompleteness.

The point source criterion can potentially induce incompleteness because ACS imaging, with a point-spread function (PSF) with FWHM of $0.12''$ at the detector, resolves all but the most compact of objects. While this is desirable in that it excludes galaxies from consideration, it may also reject intrinsically faint quasars with host galaxy light contributing to the overall flux. We discuss this issue in more detail in § 2.6.4.

2.3.4 Identification of quasars

The selection described above is highly complete but also unreliable, in the sense that a small fraction of the selected objects actually are quasars at the redshifts of interest. However, careful examination of the COSMOS photometric and imaging data for each of the 4009 candidates is relatively fast and allows us to reject typical contaminants such as dwarf stars and lower-redshift quasars.

Visual examination of the data allows more robust classification than a reliance on SED template fitting. The 29 bands of photometry and corresponding imaging data reveal stars with unusual colors that mimic quasar SEDs closely, often because of photometric contamination, as well as true quasars that automated tests fail to find because of contaminated or unusual photometry. In addition, coarse redshift estimates can be made based on the position of Lyα emission and/or the Lyman break, which can then be compared with the results from automated fitting.

The relevant high redshift quasar characteristics we look for in the COSMOS photometric and imaging data include: (1) a strong spectral break at rest-frame 1216 Å, (2) a power law SED that is flat or rising in the infrared IRAC bands, (3) Lyα emission evident in intermediate band filters, and (4) often other strong rest-frame UV emission lines (e.g., CIV λ1549, CIII] λ1909) evident in intermediate band filters as well.

Stars, in contrast, have SEDs with characteristic Rayleigh-Jeans shapes that decline in the IRAC bands. The decline in the blue side of a stellar SED is less abrupt than the Lyman break in the SED of a high redshift quasar, and there are no emission lines in the intermediate bands. Figure 2.4 illustrates, for some of the most difficult cases, the clear differences in the SEDs of high redshift quasars and stellar contaminants.

The candidates were examined using Specpro (Masters & Capak 2011), an

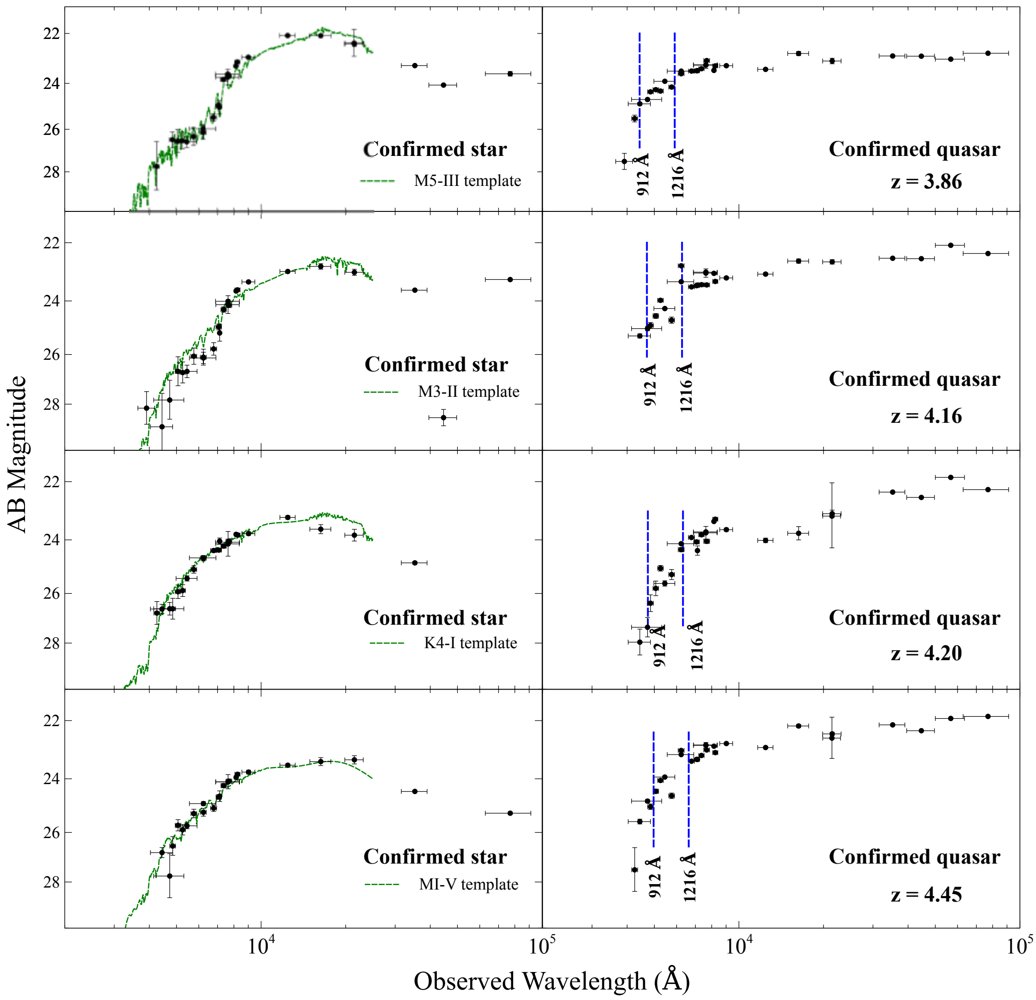

Figure 2.4 SEDs from the quasar candidates selected in I11. Stars are shown on the left and confirmed quasars on the right. The stars are dwarfs representative of those typically contaminating quasar searches, and the quasars are among the faintest known. Stellar templates (Pickles 1998) are overlaid in green. The obvious differences between the SEDs of the objects make it relatively simple to distinguish them, even without high-resolution spectroscopy. The observed-frame position of the the Lyman break and Lyman limit are indicated on the quasar SEDs with vertical blue lines. The distinct break, with a power law SED in the infrared bands, is characteristic of faint, high redshift quasars and distinguishes them from stars.

interactive IDL tool designed primarily for spectral analysis in the context of multi-wavelength surveys*. This program displays the imaging and photometric data for each candidate and allows us to perform rough SED fitting and redshift estimation. The first author went through all candidates after significant calibration against the SEDs of known stars and high-redshift quasars, and subsets of the data were examined by coauthors to establish the consistency and reproducibility of classification. It was found that classifications were highly consistent among different classifiers.

As expected, our sample includes a large fraction of stellar contaminants. Most of these are dwarf stars, while a fraction are stars whose optical fluxes are incorrectly matched to a nearby IR-bright source, which is apparent through examination of the stamp images. The mismatch artificially boosts the SED in the IRAC bands, such that the χ^2_{qso} vs. χ^2_{star} comparison does not favor a star assignment.

We also find a number of quasars or compact galaxies at $z < 3.1$ in our sample, which reflects the fact that our Lyman-break criterion (4) is very relaxed. This can also be seen in the slow decline in completeness toward $z = 3$ in Figure 2.3. Lower-redshift objects are identified by the position (or absence) of the Lyman break / Lyα emission in the SED. Of the contaminants, we estimate that 28% are $z < 3.1$ objects (quasars or compact low-z galaxies), and 64% are stars. The remaining 8% are unclear based on the photometry but likely fall in one of these categories as they do not show characteristics of $z > 3.1$ quasar SEDs.

For the sources identified as likely high redshift quasars, we assign a confidence flag ranging from 2 to 4, where 4 is highly confident and 2 is somewhat confident. We emphasize that sources even marginally consistent with being high-redshift quasars are retained (usually at confidence 2) in order to maintain high completeness. Candidates

*specpro.caltech.edu

assigned a confidence of 4 typically are X-ray detected and/or show strong emission lines in intermediate bands, as well as a clearly defined Lyman break and rising infrared SED. Candidates assigned a confidence 3 show a well-defined Lyman break and/or Lyα emission evident in an intermediate band filter as well as a rising infrared SED, but are not clearly detected in X-ray. We are confident that these are high redshift quasars based on their point-source morphology and SED. Candidates assigned a confidence 2 show a moderately convincing photometric break and are flat or rising in the infrared, but do not necessarily show emission features in intermediate bands, nor are they X-ray detected. Of our candidates these are the most likely to be either very compact galaxies or unusual stars rather than quasars. Follow-up spectroscopy on these sources may be required to refine the results presented here.

2.3.5 Identification reliability

The quasar candidates were examined without knowing which were the previously confirmed quasars, yet every one of the 39 known quasars at $z \geq 3.1$ in the COSMOS field was correctly classified based on the imaging and photometric data. The method employed thus independently recovered every previously known type-1 quasar in the field. Figure 2.5 shows that the confirmed sample includes a number of very faint sources, including those discovered by Ikeda et al. (2011). This is strong evidence that we do not miss actual high-redshift quasars in the initial sample. If anything, we may overcount by misidentifying either stars or high-redshift galaxies as quasars. Because stars display easily recognizable SEDs, we consider it unlikely that they constitute a significant contaminant.

While stars are relatively easy to reject, high redshift galaxies display a similar

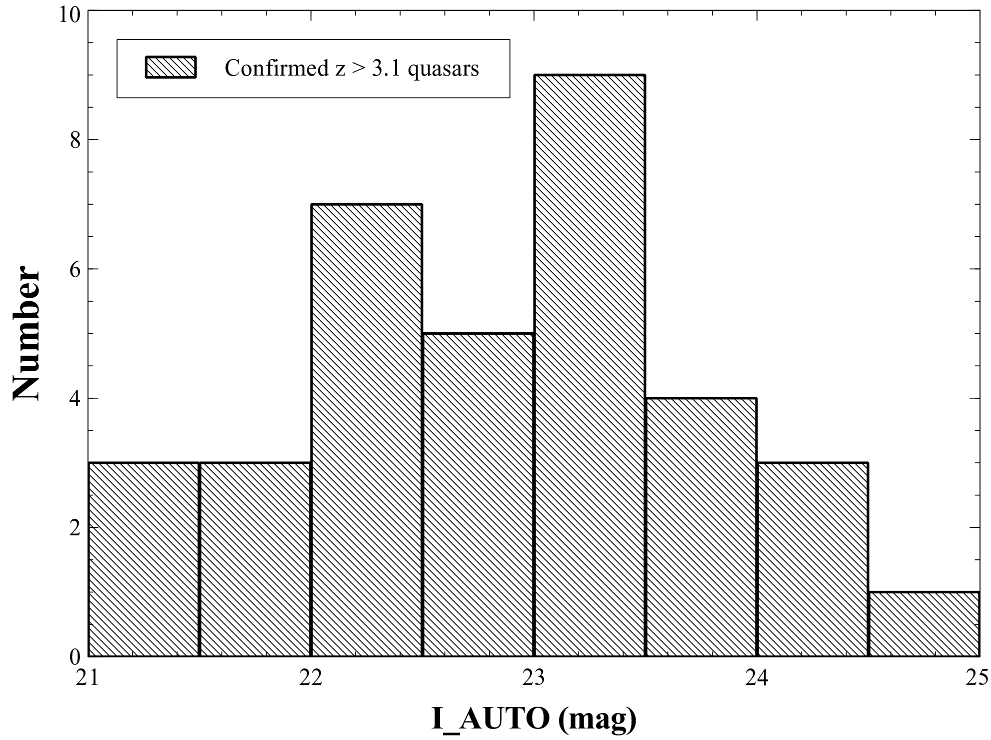

Figure 2.5 The distribution in I(mag_auto) for the spectroscopically confirmed subset of our final quasar candidates. We have recovered both relatively bright and very faint known quasars in the field, indicating that there is high overall completeness in our classification method regardless of quasar luminosity.

overall SED to a quasar and could contaminate the sample. We expect that few of the candidates identified as quasars are actually compact galaxies, because the strict point-source criterion will eliminate nearly all galaxies at these redshifts. We discuss this potential source of error in more detail in § 2.6.3.

Of 4009 candidates, we find 155 likely type-1 quasars at $z > 3.1$. Of these, 48 are considered confidence 2 sources, 54 are considered confidence 3, and 53 are considered confidence 4.

2.3.6 Comparison with traditional χ^2–based quasar selection

As another check on the reliability of our classifications, we compare our final sample with a purely automated selection using the results of the extensive χ^2 fitting against stellar and AGN templates described in Ilbert et al. (2009). Of the initial sample of 4009 candidates, 195 objects have photometric redshift estimates above $z = 3.1$. Limiting the sample to objects with $\chi^2_{qso}/\chi^2_{star} \leq 1.0$ (i.e., quasar is the favored solution from χ^2 fitting) the final automated sample is 143 objects, in very close agreement with our final sample of 155 from visual classification.

Figure 2.6 shows that, of the 195 objects with photometric redshifts above 3.1, our visual classification typically retains objects with $\chi^2_{qso}/\chi^2_{star} \lesssim 1$ and rejects objects with $\chi^2_{qso}/\chi^2_{star} \gtrsim 1$, as would be expected if the visual classification is in agreement with χ^2 fitting.

Of the 143 objects that would be selected automatically, 91 are in common with our final selection. The sources that we rejected but automated fitting would retain are, for the most part, stars mismatched to a nearby IR-bright source, artificially elevating their IRAC fluxes. This is reflected in the fact that these sources have higher average IRAC-to-optical match distances. On the other hand, we identify 64 likely quasars that are rejected by the automated selection. These primarily are rejected due to a low photometric redshift estimate. However, they are consistent with being high-z quasars based on a weak photometric break and power law infrared spectrum, so we retain them.

Despite the slightly different samples, it is clear that automated selection based on χ^2 fitting produces essentially the same answer as careful rejection of contaminants on an object-by-object basis.

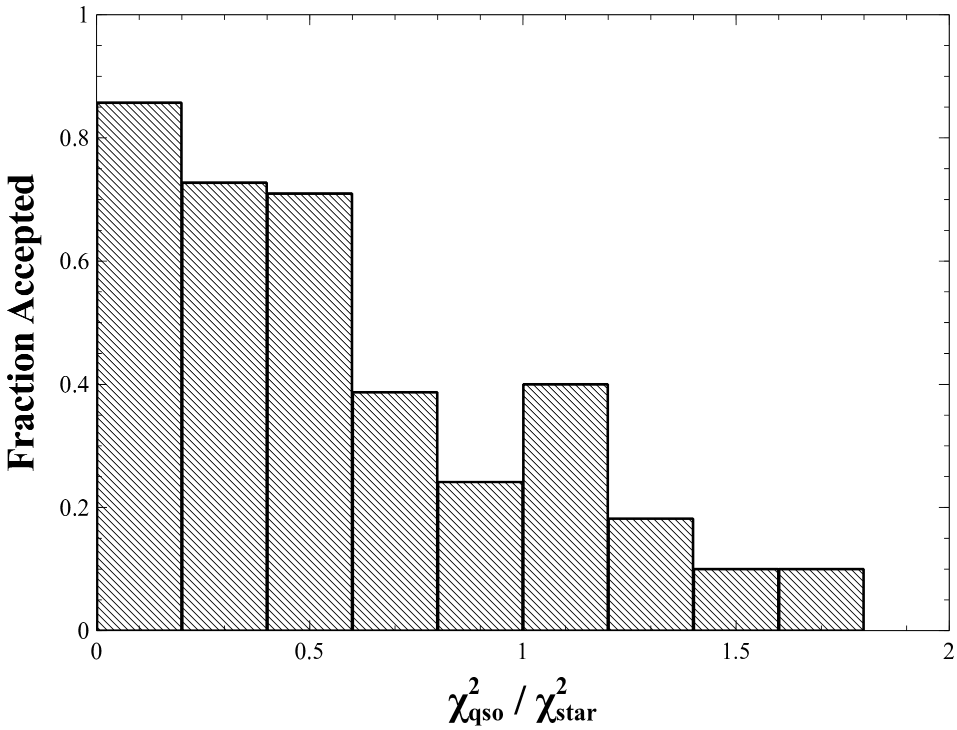

Figure 2.6 The fraction of the $z_{qso} > 3.1$ candidates we identify as high redshift quasars as a function of the ratio $\chi^2_{qso}/\chi^2_{star}$. As expected, the lower this ratio, the more likely that we identify a candidate as a quasar through inspection of the imaging and photometry, showing that our visual inspection is in accord with the results of χ^2 fitting against spectral templates.

2.4 X-ray properties of the sample

The Chandra COSMOS survey (C-COSMOS, Elvis et al. 2009) is a 1.8 Ms Chandra program covering the central 0.5 deg^2 of the COSMOS field with an effective exposure of ~160 ks, and an outer 0.4 deg^2 area with an effective exposure of ~80 ks. In addition, the entire COSMOS field has been observed in the X-ray with XMM-Newton (Hasinger et al. 2007) to a brighter X-ray flux limit.

Of the final sample of confirmed and likely quasars presented here, 27 are X-ray detected by Chandra (Civano et al. 2011, 2012) and 12 are detected by XMM (Brusa et al. 2010). The remainder of the objects are undetected and therefore have X-ray fluxes below the detection limits of either Chandra deep, Chandra shallow, or XMM, depending on their location in the COSMOS field. We perform a stacking analysis of 47 unconfirmed sources without X-ray detection in the Chandra region to investigate whether their X-ray fluxes are consistent with expected quasar emission.

We use CSTACK (Miyaji et al. 2008) to compute the number of X-ray counts at the optical position of the undetected sources. This program correctly accounts for the different exposure times depending on source position. We find a detection in the soft-band 0.5-2.0 keV (Figure 2.7), corresponding closely to rest-frame 2-10 keV for our sources, with a significance of ~5-6 sigma, as determined through random stacking in blank fields. We find no clear detection in the observed-frame 2-8 keV hard band. The stacked detection in the soft band provides evidence that these sources are quasars with individual X-ray fluxes below the Chandra detection limit, while the lack of a clear hard band detection suggests no significant X-ray obscuration.

As another check on whether the X-ray flux limits on the nondetected candidates are consistent with these objects being quasars, we compute the α_{ox} ratio for sources in the C-COSMOS region, making use of the SEDs to derive the rest-frame UV fluxes. The α_{ox} parameter represents the spectral slope between the UV and X-ray flux:

$$\alpha_{ox} \equiv \frac{\log(f_{\rm X}/f_{\rm uv})}{\log(\nu_{\rm X}/\nu_{\rm uv})} \tag{2.2}$$

where $f_{\rm uv}$ is the 2500 Å flux and $f_{\rm X}$ is the 2 keV X-ray flux. For X-ray detected sources we derived the 2keV X-ray flux from the 0.5-2 keV flux (Elvis et al. 2009). For sources without X-ray detection, we compute an upper limit on the X-ray flux, taking into account the X-ray flux limit at the optical position of each source. The result in

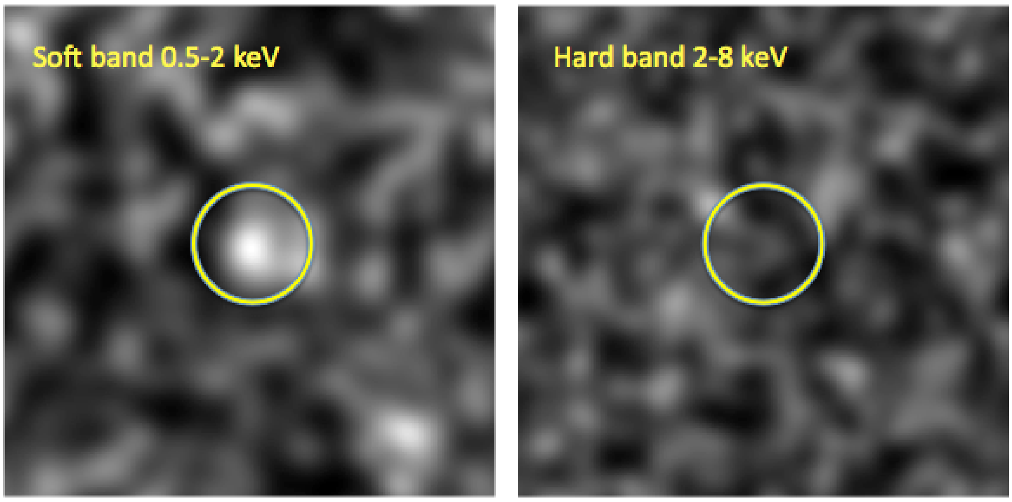

Figure 2.7 Stacking analysis of 47 likely quasars that fall in the Chandra region but are not individually detected in X-ray. The images are $30'' \times 30''$ and are smoothed with a Gaussian kernel with FWHM of $6''$. The ~5-6 sigma detection in the soft band (corresponding to the hard X-ray band in the rest frame at $z \sim 3-4$) is evidence that at least a fraction of the individually undetected sources are quasars. The lack of a clear detection in the observed-frame 2-8 keV stack indicates they are likely unobscured, intrinsically faint objects that fall below the detection limit in the hard band.

Figure 2.8 shows that the nondetected sources tend to have lower UV luminosity, with upper limits on the α_{ox} ratio that are generally consistent with previously measured correlations between α_{ox} and the 2500 Å luminosity (Steffen et al. 2006, Young et al. 2010). In conjunction with the stacking results, this gives additional evidence that the sources are faint, type-1 quasars with X-ray fluxes below the Chandra detection limit.

2.5 The luminosity function

We derive the luminosity function for the redshift bins $3.1 \leq z \leq 3.5$ and $3.5 < z \leq 5.0$, using the standard $1/V_{max}$ estimator (Schmidt 1968). We use the

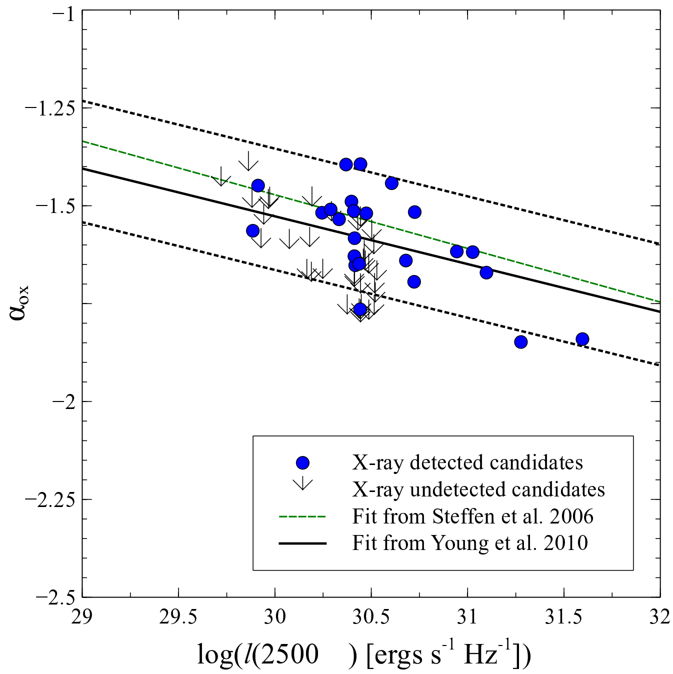

Figure 2.8 The X-ray / UV correlation for the sources in our sample in the Chandra region of COSMOS. The α_{ox} ratios (or upper limits on the ratio for sources without individual X-ray detection) are generally consistent with measured correlations at lower redshifts. The dotted lines indicate the 1-sigma dispersion in the α_{ox} relation of Young et al. 2010.

parameterization of the luminosity function given in Equation 2.1 to fit our results, in conjunction with bright-end results of Richards et al. (2006) derived in the SDSS. Before presenting the results we first outline the determination of redshift and absolute magnitude for the sample.

2.5.1 Redshift determination

Only 39 of the 155 sources in the final sample have spectroscopic redshifts. For those that do not, we use the photometric redshift z_{qso} determined by fitting AGN templates to the source SED (Ilbert et al. 2009). In the cases in which a candidate is

X-ray detected but not spectroscopically confirmed, we adopt the photometric redshifts of Salvato et al. (2009, 2011), which have been computed for X-ray sources in COSMOS and are optimized for AGN.

We check to verify that the photometric redshift is in rough agreement with the redshift estimated from visual examination of the source SED. If there is a very large disagreement between the photometric and visual redshift estimates, we adopt the visually estimated redshift. This accounts for occasional failures of the photometric redshift determination due to contaminated photometry in a small number of bands.

In Figure 2.9 we show both the photometric redshift and estimated redshift compared with the spectroscopic redshift for the subset of spectroscopically confirmed candidates. The photometric redshift is generally more accurate, but contains a small number of outliers. The visually estimated redshifts are low on average, but there are no outliers. These estimated redshifts were made by identifying the position of the Lyman-break/Lyman-limit in the source SED. The fact that they are systematically low by a small amount reflects a small bias in this visual estimate. We only adopt these values in cases in which the photometric redshift is likely incorrect, primarily as a result of contaminated photometry (29 of the 80 sources in the $3.1 < z < 3.5$ bin and 9 of the 48 sources in the $3.5 < z < 5$ bin). Because our redshift bins are relatively large, the errors introduced by doing so will not have a significant effect on the derived luminosity functions.

2.5.2 Absolute magnitude determination

We follow the convention of giving the quasar luminosity function in terms of the absolute magnitude at rest-frame 1450 Å. To estimate M_{1450}, we fit quasar templates

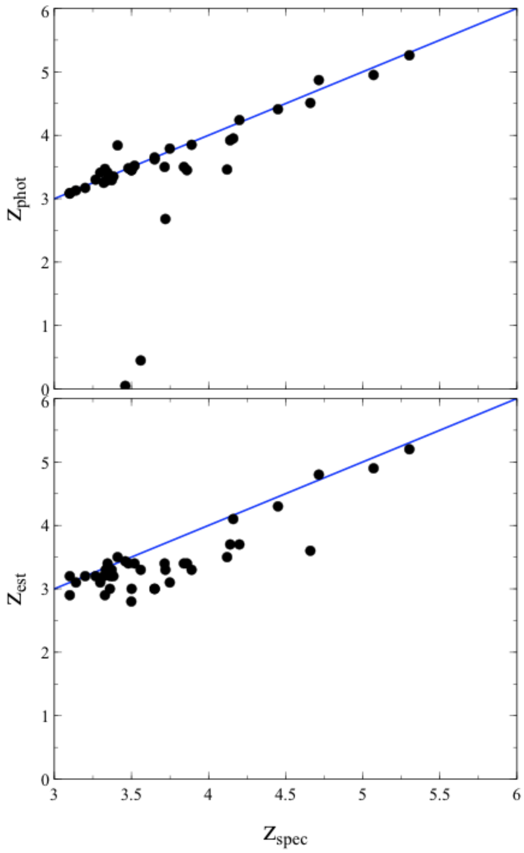

Figure 2.9 *Top:* the photometric versus spectroscopic redshift for the sources in our sample with spectroscopic confirmation. The scatter is ∼0.7, with a few outliers. *Bottom*: the estimated redshifts versus spectroscopic redshifts for the same sources. Our visual estimates are systematically low, but with no outliers. These values are only adopted when no spectroscopic redshift is available and the photometric redshift is clearly wrong. This amounts to 29 out of 80 sources in the $3.1 < z < 3.5$ bin and 9 out of 46 sources in the $3.5 < z < 5$ bin.

to the source SED, which accounts for elevated fluxes due to quasar emission lines. We found that fitting to the measured magnitudes in the three broad-band Subaru filters V, R, and I and interpolating to find the observed-frame 1450 Å magnitude often overestimates the luminosity due to the contribution of quasar emission lines to the measured broad-band magnitudes.

When performing the SED fits to find M_{1450}, only filters within ±2000 Å of the observed-frame wavelength corresponding to rest-frame 1450 Å are considered. The M_{1450} values we find through SED fitting are typically ∼0.2 magnitudes fainter than what we found by extrapolating the broad band magnitudes, but with significant scatter (Figure 2.10).

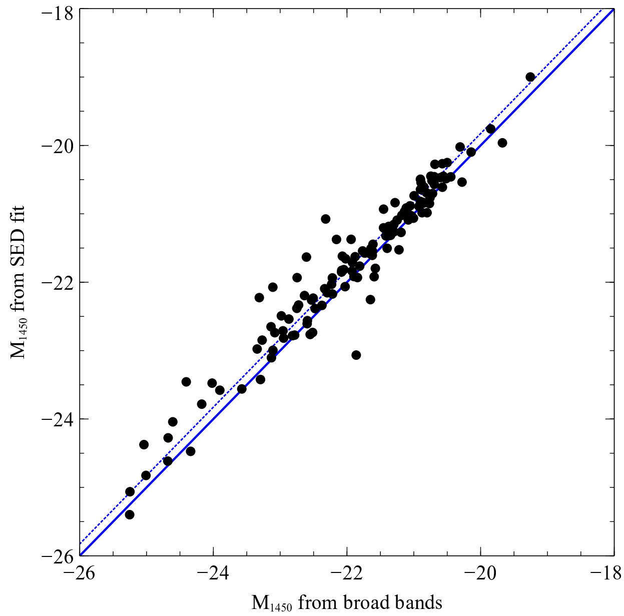

Figure 2.10 Comparison of the M_{1450} value derived from a linear fit to broad band filters vs. that derived from SED fitting. The absolute magnitude estimated using the SED fit is fainter by ∼0.2 magnitudes on average, as indicated with the dotted line. This reflects the fact that the broad band fluxes can be elevated relative to the underlying continuum by broad emission lines.

Given the observed magnitude m corresponding to rest-frame 1450 Å radiation, the absolute magnitude is found with

$$M_{1450} = m - 5\log(d_L/10) + 2.5\log(1+z) \tag{2.3}$$

The second term on the right-hand side is the distance modulus; the final term is a correction for the effective narrowing of the frequency interval sampled in the observed frame.

2.5.3 The luminosity function at $z \sim 3.2$ and $z \sim 4$

We compute the luminosity fuction using the derived redshifts and absolute magnitudes for the sample, correcting for the incompleteness at $I \gtrsim 24$ from the selection function in Figure 2.3. The luminosity function we derive for the redshift bin $3.1 < z < 3.5$ is shown in Figure 2.11. There is good continuity with the bright-end result derived in the SDSS, as well as close agreement with prior results that have probed the faint end at similar redshift (e.g., Siana et al. 2008, Bongiorno et al. 2007, Wolf et al. 2003).

We fit the $z \sim 3.2$ QLF to the double power law relationship (Equation 2.1) using our faint-end result in conjunction with the bright end from Richards et al. (2006). The best-fit parameters we derive are $\Phi^* = 2.65(\pm 2.22) \times 10^{-7}$, $M^*_{1450} = -25.54 \pm 0.68$, $\alpha = -2.98 \pm 0.21$, and $\beta = -1.73 \pm 0.11$.

In Figure 2.12 we show the result for the $z \sim 4$ luminosity function, together with the previous results from G11 and I11. The best-fit parameters to the double power law paramaterization are $\Phi^* = 7.5(\pm 23.5) \times 10^{-8}$, $M^*_{1450} = -25.64 \pm 2.99$, $\alpha = -2.60 \pm 0.63$, and $\beta = -1.72 \pm 0.28$. Our faint end result is in agreement with the result reported by I11, and the faint-end slopes we find at both $z \sim 3.2$ and $z \sim 4$ agree with the faint-end slope at $2 < z < 3.6$ ($\beta = -1.70$) derived in Jiang et al. (2006). However, the space density of faint quasars at $z \sim 4$ we find is lower than the result reported in G11 by a factor of ∼3-4. The source of this discrepancy is unclear, but may be due

Table 2.1. Binned luminosity function at $z \sim 3.2$ and $z \sim 4$.

ΔM_{1450}	N_{QSO}	Φ ($\times 10^{-7}$) (Mpc^{-3} mag^{-1})	$\Delta\Phi$ ($\times 10^{-7}$)
$z \sim 3.2$			
[-25.5,-23.5]	4	5.3	2.6
[-23.5,-22.5]	9	11.9	3.9
[-22.5,-21.5]	26	39.0	7.1
[-21.5,-20.5]	41	59.8	8.4
$z \sim 4$			
[-25.5,-23.5]	5	1.9	0.8
[-23.5,-22.5]	9	3.5	1.2
[-22.5,-21.5]	14	6.4	1.4
[-21.5,-20.5]	20	20.6	2.6

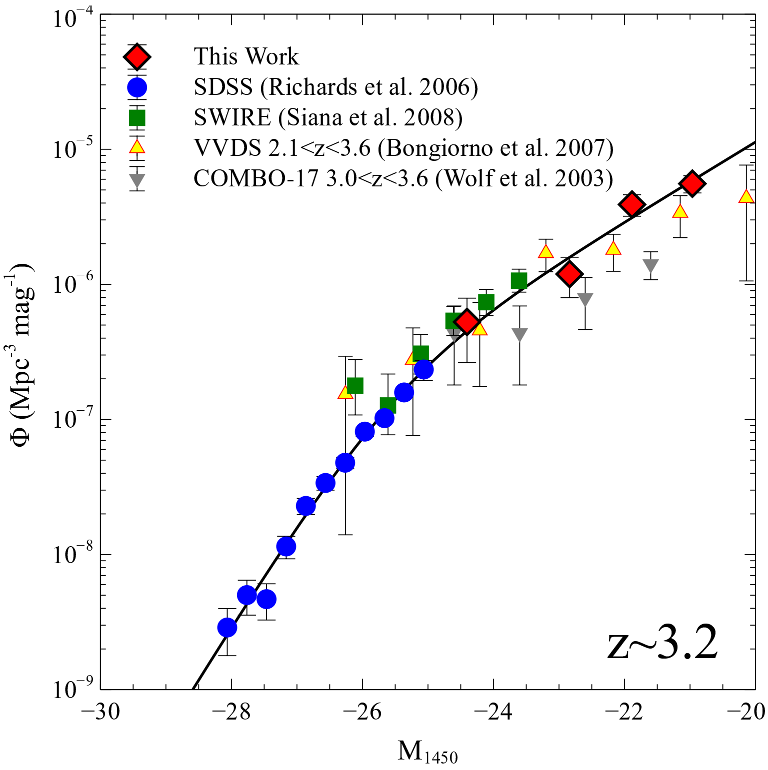

Figure 2.11 The $z \sim 3.2$ luminosity function derived here compared with previous results. The solid black line is our best fit to the double power law parameterization including the bright-end result from the SDSS. Our result is in close agreement with previous determinations of the QLF at similar redshift. The faint-end slope we derive is $\beta = -1.73 \pm 0.11$.

to contamination (dwarf stars and high-redshift galaxies) in the sample of G11 at the faintest magnitudes probed in that work. The point-source selection used in G11 is done with ground-based imaging, which is not as effective as HST imaging at resolving compact, high-z galaxies. Additionally, the number of stellar contaminants in broad band quasar searches grows rapidly at the faintest magnitudes, where spectroscopic follow-up is the most challenging and thus the contamination is not as well-constrained.

In Figure 2.13 we illustrate the strong evolution of the luminosity function from $z \sim 3.2$ to $z \sim 4$. We find that the space density of faint quasars decreases by a factor of

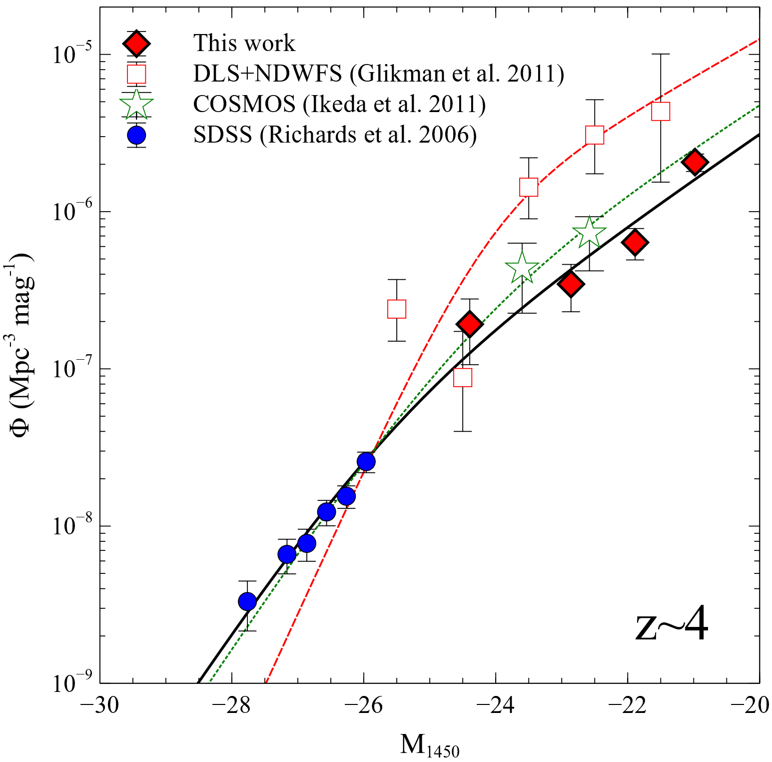

Figure 2.12 The $z \sim 4$ luminosity function derived here compared with previous results. The solid black line is our best fit to the double power law parameterization including the bright-end result from the SDSS. The dotted green line is the best fit from I11 and the dashed red line is the best fit from G11. The disagreement between the bright-end result of G11 and the SDSS data points arises because G11 recompute the SDSS results after finding the absolute magnitudes directly from the SDSS spectra. Our result is in close agreement with that of III. The disagreement in the faint-end space density between the result derived here and that derived in the DLS+NDWFS is significant, with that result higher by a factor of ∼4.

four between $z \sim 3.2$ and $z \sim 4$, in close analogy with the evolution of brighter optical and X-ray quasars at these redshifts. This trend is also verified by the results presented in Ikeda et al. (2012), where it is found that the space density of faint quasars at $z \sim 5$

Table 2.2. Double power law parameters, combining SDSS and this work.

$\Phi(M^*)$	M^*_{1450}	α	β
$\boldsymbol{z \sim 3.2}$**:**			
$2.65(\pm 2.22) \times 10^{-7}$	-25.54 ± 0.68	-2.98 ± 0.21	-1.73 ± 0.11
$\boldsymbol{z \sim 4}$**:**			
$7.5(\pm 23.5) \times 10^{-8}$	-25.64 ± 2.99	-2.60 ± 0.63	-1.72 ± 0.28

is significantly lower than at $z \sim 4$.

2.6 Potential sources of error affecting the QLF determination

2.6.1 Cosmic variance

The comoving volume probed here at $z \sim 4$ is sufficiently large (2.6×10^7 Mpc^3) that we expect cosmic variance to have little effect. However, it has been shown in the SDSS (Shen et al. 2007) that the bias of luminous, high redshift quasars relative to dark matter halos increases dramatically with redshift, so we attempt to estimate the likely error introduced by cosmic variance.

We make use of the cosmic variance cookbook of Moster et al. (2011), in which the bias of galaxies as a function of stellar mass and redshift is used to compute the counting error for galaxies due to cosmic variance. Quasars are expected to be significantly biased with respect to the matter distribution, existing preferentially in the

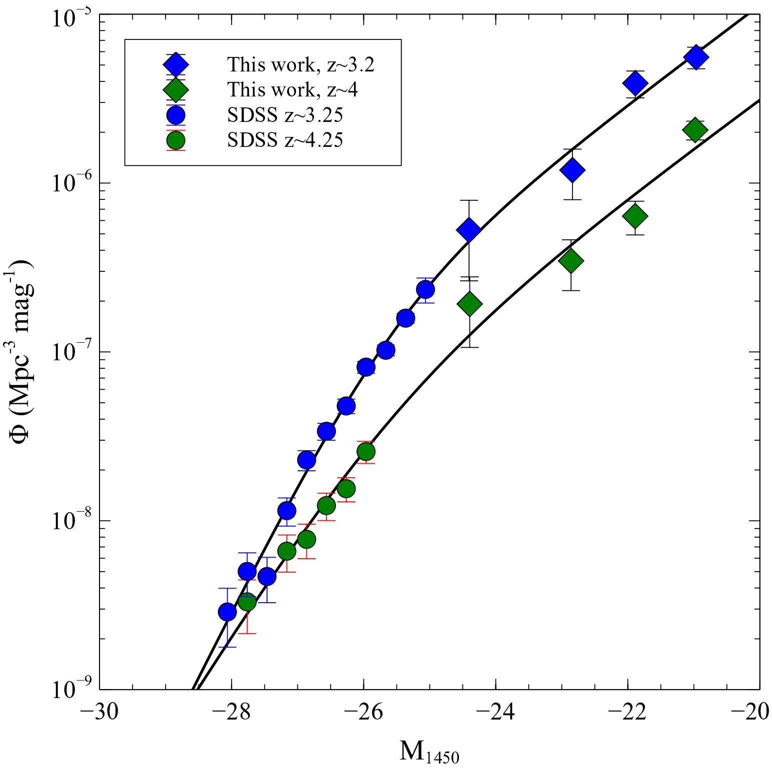

Figure 2.13 The evolution of the luminosity function from $z \sim 4$ to $z \sim 3.2$, combining the bright end derived from the SDSS (Richards et al. 2006) with the faint end derived here. The space density of faint quasars increases by a factor of ∼4 from $z \sim 4$ to $z \sim 3.2$. Overplotted are the best-fit lines for each luminosity function using the double power law parameterization. The faint-end slopes we derive for $z \sim 3.2$ and $z \sim 4$ are $\beta = -1.73 \pm 0.11$ and $\beta = -1.72 \pm 0.28$, respectively.

highest mass halos. This leads us to make the approximation that quasars are similarly biased to the most massive ($M \geq 10^{11} M_{\odot}$) galaxies. The bias factor estimated in this way is in relatively good agreement with the results presented in Shen et al. (2007) for quasar clustering in the SDSS (and may actually be slightly overestimated).

In the redshift window of $3.5 < z < 5$ in the COSMOS field, we compute an uncertainty of ∼19% in our quasar count, indicating that cosmic variance will contribute only modestly to the derived luminosity function.

2.6.2 Contamination by stars

The consistent, well-matched wavelength coverage of the COSMOS data, extending from the UV to the infrared, enables the identification and removal of stellar contaminants, the SEDs of which differ substantially from those of quasars. Figure 2.6 illustrates that our final selection preferentially retains objects for which χ^2 fitting disfavors stellar templates, and the close agreement with prior studies at $z \sim 3$ also indicates that contamination is low. If there were significant stellar contamination in the final sample, it would imply that the luminosity functions are upper bounds, making it more difficult to reconcile the result at $z \sim 4$ found here with that of G11.

2.6.3 Contamination by star-forming galaxies

Because we only have spectroscopic confirmation for a fraction of our sample, we may overestimate the faintest end of the luminosity function by inadvertantly counting compact, star-forming galaxies as quasars. To estimate the contamination from high-redshift galaxies, we analyze a sample of 386 confirmed star-forming galaxies at $z > 3$ in COSMOS. These sources were selected as part of a large spectroscopic campaign with Keck DEIMOS (Capak et al., in preparation) aimed at finding high-redshift galaxies down to $I = 25$ from $3 < z < 6$. A number of techniques (Lyman-break criteria, narrow-band selection, etc.) were employed to achieve high completeness, with no selection based on morphology. By applying our quasar selection to these objects, we can get a reasonable sense of the contamination due to compact galaxies.

Of the 386 confirmed high-redshift galaxies, only 2 (0.5%) pass our selection (and were removed from our final sample), with the rest rejected primarily on the basis of morphology. We can combine the fraction of high-redshift star forming galaxies likely to contaminate our sample with the UV luminosity function for galaxies at $z \sim 4$ (Bouwens et al. 2007) to estimate the level of contamination. Restricting our attention to the faintest absolute magnitude bin ($M_{1450} = -21$) examined at $z \sim 4$, we estimate a contamination level of roughly 10^{-6} (Mpc^{-3} mag^{-1}) by star-forming galaxies. This is approximately half the space density we derive in this magnitude bin. Therefore, this faintest data point on the luminosity function may be elevated somewhat significantly by star-forming galaxy contamination, leading to an overestimation of the faint-end slope. This issue may need to be settled by follow-up spectroscopy on the faintest sources in the sample.

2.6.4 Faint quasars in bright host galaxies

Conversely, we may underestimate the faintest bins of the luminosity functions by rejecting bright galaxies hosting faint quasars. This will be the case if a significant fraction of faint type-1 quasars ($M_{1450} \gtrsim -23$) exist in galaxies bright enough in the rest-frame UV to make the source appear extended in ACS I-band imaging. Two pieces of evidence lead us to believe that this is not the case.

First, we examine 12 Keck DEIMOS spectra of Chandra sources at high redshift that are classified as extended in the ACS catalog, and find that these sources do not show broad lines indicative of a type-1 quasar. Therefore there is no evidence from spectroscopy of high-redshift X-ray sources of a population of type-1 quasars that we miss by restricting our search to point sources. On the contrary, high-redshift X-ray sources that are morphologically extended seem to be exclusively type-2 AGN.

Second, we note that, in the sample of ∼1400 high-redshift candidate galaxies in COSMOS followed up on with Keck DEIMOS spectroscopy, we do not find cases of broad-line objects with extended morphology. If a significant number of faint type-1 quasars at $z \sim 4$ have host galaxies bright enough in the rest-frame UV to make the galaxy appear extended in ACS imaging, we should find serendipitous examples of these in a large sample of candidate high-redshift galaxies. In fact we do not; high-redshift, broad-line emitting objects seem invariably to be point sources in the rest-frame UV.

We conclude from these two tests that we do not miss a substantial fraction of type-1 quasars due to our morphological criterion, even at the faintest quasar magnitudes.

2.7 Comparison of the X-ray and UV quasar luminosity functions

The X-ray luminosity function at $z > 3$ in COSMOS was determined recently for the 0.9 deg^2 Chandra region in COSMOS (Civano et al. (2011), hereafter C11). In C11 it is shown that the population of X-ray luminous AGN decreases rapidly above $z = 3$, in agreement with previous results (e.g., Brusa et al. 2009; Silverman et al. 2008). In fact, Figure 4 of C11 shows a decline in space density of X-ray luminous ($L_{\rm x} \gtrsim 10^{44}$ ergs s^{-1}) AGN by a factor of ∼4 between $z \sim 3.2$ and $z \sim 4$, in agreement with the trend we have demonstrated here for the faint end of the UV QLF at the same redshifts.

A rough sense of the obscured fraction at these redshifts can be obtained simply by comparing the high-redshift X-ray sample with our list of type-1 quasars. Doing so, we find that our selection finds 27/101 sources in the high-redshift X-ray sample. The X-ray sources that we miss are primarily classified as extended in the ACS I-band imaging, or are fainter than $I = 25$, or both. As mentioned previously, an examination of 12 spectra of high-redshift X-ray sources that are classified as extended in ACS imaging shows that they are consistent with being type-2 AGN rather than unobscured quasars. Assuming that the X-ray sources our selection misses are in fact optically obscured, this leads to an estimated type-2 fraction of roughly 75%.

To more quantitatitvely compare our results with those found in C11, we convert our rest-frame UV luminosity functions to X-ray using the α_{ox} relationship presented in Steffen et al. (2006):

$$\log(l_{2\mathrm{keV}}) = (0.721 \pm 0.011)\log(l_{2500\mathrm{\AA}}) + (4.531 \pm 0.688) \quad (2.4)$$

We modify this relationship slightly to put it in terms of the luminosity at 1450 Å by assuming a typical quasar spectral slope. With this relationship, the space density of quasars with $L_{\mathrm{x}} > 10^{44.15}$ erg s^{-1} is found by integrating the UV luminosity functions over the absolute magnitude interval $M_{1450} = [-\infty, -23.45]$. The uncertainty in the conversion is based on the uncertainty in the parameters of the α_{ox} relation.

Our results are plotted as black diamonds in Figure 2.14, together with the X-ray results of C11. The same trend with redshift is observed, but the points derived from the UV QLF are lower by a factor of $\sim$4, in agreement with the ratio found by directly comparing the two samples. While the C11 space density is in agreement with the prediction for obscured and unobscured sources (solid line) derived from the Gilli et al. (2007) X-ray background synthesis model, the space density derived from the UV QLF is more consistent with the prediction for unobscured sources only (dashed line). Based on the offset, we again find that the fraction of obscured (but not Compton-thick) quasars is roughly 75% at $z \sim 3 - 5$.

It is interesting to compare this result with the redshift evolution of the type-2 fraction determined by Hasinger (2008) (hereafter H08). Figure 9 of that work clearly indicates an upward trend in obscured fraction with redshift, which seems to saturate

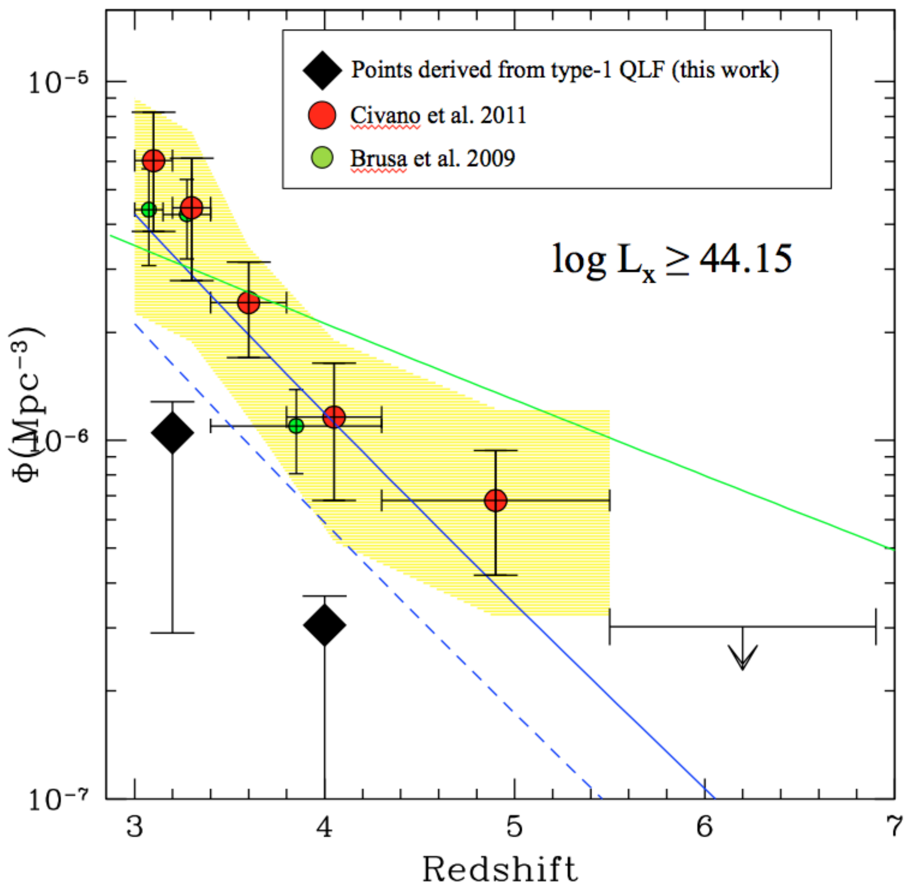

Figure 2.14 The UV luminosity function results, converted to X-ray (black diamonds), compared to the X-ray luminosity functions for X-ray bright Chandra sources derived in Civano et al. (2011) including uncertainties (red circles and yellow shaded area) and for XMM-COSMOS sources (green circles, Brusa et al. 2009). The space density is roughly a fourth of that found in X-ray, implying that ∼75% of bright quasars are optically obscured at these redshifts. The blue lines represent the prediction from the Gilli et al. (2007) model for obscured and unobscured sources (solid) and unobscured sources only (dashed).

around $z = 2$ at ∼60%. This result arises after a correction for the fact that observational bias makes it more difficult to identify obscured AGN at higher redshifts. The type-2 fraction we find at $z \sim 3-4$, ∼75%, is higher than the result in H08 and may indicate that the trend of increasing obscured fraction with redshift continues to higher redshifts.

In should also be noted that the result in Figure 9 of H08 is actually a normalization of a rather steep gradient of obscuration versus X-ray luminosity. The obscured fraction decreases with X-ray luminosity at a given redshift, such that for sources above $L_{\rm x} = 10^{44}$ at $z \sim 3 - 4$ the estimated obscured fraction is actually closer to 20-30%, significantly lower than what we find for comparably luminous sources at these redshifts. Follow-up spectroscopy on more of the $z > 3$ X-ray sources in COSMOS would allow a more firm determination of the type-2 fraction at these redshifts.

2.8 The ionizing background due to quasars

Given the luminosity function $\Phi(M_{1450}, z)$, we can estimate the rate of production of ionizing photons by quasars at redshift z. To do so, we use results from Vanden Berk et al. (2001) and Telfer et al. (2002) to approximate the spectral energy distribution of a typical quasar:

$$L(\nu) \propto \begin{cases} \nu^{-0.5} & (1216\ \text{Å} < \lambda < 2500\ \text{Å}) \\ \nu^{-1.76} & (\lambda < 1216\ \text{Å}) \end{cases} \tag{2.5}$$

The number of hydrogen-ionizing photons emitted per second by a quasar of absolute magnitude M_{1450} is given by

$$\dot{n}_{\rm HI}(M_{1450}) = \int_{1\rm ryd}^{4\rm ryd} \frac{L(M_{1450}, \nu)}{h\nu}\, d\nu \tag{2.6}$$

where the cutoff at 4 ryd is due to preferential HeII absorption of photons above this energy (Madau et al. 1999). Similarly, the rate of emission of HeII ionizing photons is given by

$$\dot{n}_{\rm HeII}(M_{1450}) = \int_{4\rm ryd}^{\infty} \frac{L(M_{1450}, \nu)}{h\nu}\, d\nu \tag{2.7}$$

Combining equations (5) and (6) with the QLF, one can compute the number of HI and HeII ionizing photons produced per second per unit comoving volume at a given redshift:

$$\dot{\mathcal{N}}_{\rm HI}(z) = \int \Phi(M,z)\dot{n}_{\rm HI}(M)\, dM \tag{2.8}$$

$$\dot{\mathcal{N}}_{\rm HeII}(z) = \int \Phi(M,z)\dot{n}_{\rm HeII}(M)\, dM \tag{2.9}$$

We use the results for the QLF at $z \sim 3.2$ and $z \sim 4$ presented in § 2.5 to estimate these ionizing backgrounds and their evolution with redshift.

2.8.1 HI ionizing background

With the QLFs derived in § 2.5, we find quasar emission rates of hydrogen-ionizing photons at $z \sim 3.2$ and $z \sim 4$ of $\dot{\mathcal{N}}_{\rm HI} = 3.3 \times 10^{50}$ s^{-1} Mpc^{-3} and 1.0×10^{50} s^{-1} Mpc^{-3}, respectively. These rates are lower than needed to reionize the IGM at either redshift. At z=4, for example, the estimated required rate for reionization is $\dot{\mathcal{N}}_{\rm HI} = 2.4 \times 10^{51}$ s^{-1} Mpc^{-3} (Madau et al. 1999), more than 20 times higher than what we find. In addition, the rates we compute ignore escape fraction and are therefore upper limits on the photons available to ionize the IGM.

The emissivity of UV radiation due to quasars can be found with our luminosity functions and compared with the result given in Haardt & Madau (2012). We integrate to find the emissivity at 1450 Å and use a conversion factor of $f_{912\text{Å}}$ / $f_{1450\text{Å}} = 0.58$ to convert to the corresponding emissivity at 912 Å. At $z \sim 3.2$ and $z \sim 4$ we find $\epsilon_{912\text{Å}} = 4.4 \times 10^{24}$ and 1.4×10^{24} ergs s^{-1} Mpc^{-3} Hz^{-1}, respectively. Haardt & Madau (2012) find $\epsilon_{912\text{Å}} = 4.3 \times 10^{24}$ and 2.0×10^{24} ergs s^{-1} Mpc^{-3} Hz^{-1} at the same redshifts. We are in relatively close agreement, although our value at $z \sim 4$ is somewhat lower, likely due to the rapid decline in the space density of faint quasars we find.

The emissivity we find at $z \sim 4$ is significantly lower than that required to maintain reionization at $z \sim 7$ (Robertson et al. 2010), even assuming a very high escape fraction for ionizing photons. Therefore, assuming that the faint-end of the QLF continues to decline at higher redshifts, type-1 quasars can not contribute significantly to cosmic reionization of hydrogen at $z \sim 6 - 10$.

2.8.2 HeII ionizing background

We find a QSO emission rate of HeII-ionizing photons at $z \sim 3.2$ of $\dot{\mathcal{N}}_{\rm HeII} = 3.1 \times 10^{49}$ s^{-1} Mpc^{-3}. At $z \sim 4$ we find $\dot{\mathcal{N}}_{\rm HeII} = 1.0 \times 10^{49}$ s^{-1} Mpc^{-3}. The significant increase in the production by quasars of HeII-ionizing (>54.4 eV) photons from $z \sim 4 \rightarrow 3$ is qualitatively consistent with the observed patchy reionization of HeII at $z \sim 3$ (Shull et al. 2010; Bolton et al. 2006). While AGN are considered the only sources capable of producing sufficient photons with energies above 54.4 eV to be responsible for the reionization of HeII, significant uncertainty exists with regard to the specifics of the HeII reionization process (Shull et al. 2010). This is mainly due to degeneracies between temperature, density, and ionization fraction in the IGM, as well as the dependence on the spatial distribution and spectral hardness of the ionizing sources. Therefore, we do not attempt to quantify the ionizing background needed to produce the observed HeII reionization at $z \sim 3$.

2.9 Conclusions

We searched the COSMOS field for type-1 quasars at $3.1 < z < 5$ and $I_{\rm AB} < 25$, with care taken to achieve high completeness. Our method applied a weak quasar selection that is nearly complete but unreliable, and then identify and remove contaminants through careful inspection and χ^2 analysis of the COSMOS photometric and imaging data. This method exploits the fact that stellar contaminants are readily identified with the 29 bands of deep photometry spanning the UV to the infrared. We recover all 39 previously known type-1 quasars at $z > 3.1$ in COSMOS as well as 116 additional likely quasars, and have presented evidence based on simulations and automated classifiers that this sample is highly complete for type-1 quasars above $z = 3.1$ in the HST-ACS region (1.64 $\rm deg^2$) of COSMOS.

A summary of the main conclusions follows.

1. We find 155 likely type-1 quasars at $z > 3.1$ in the COSMOS field, 39 of which have been previously confirmed, down to a limiting magnitude $I_{AB} = 25$. We present strong evidence that this quasar sample is nearly complete over the redshift range $3.1 < z < 5$.

2. We use the quasar sample to compute the QLF at $z \sim 3.2$ and $z \sim 4$. The faint-end results we obtain show continuity with the bright-end results reported by Richards et al. (2006) for the SDSS, and demonstrate a clear decrease in the space density of faint quasars, by roughly a factor of four, from $z \sim 3.2$ to $z \sim 4$. The faint-end we derive at $z \sim 4$ is in good agreement with the result reported for the COSMOS field in I11, but disagrees with the result reported in G11. While the source of this discrepancy is unclear, we suggest that it may be caused by contaminating stars/high-redshift galaxies at the faintest magnitudes in the sample of G11.

3. We find no evolution in the faint-end slope β over the redshift range investigated. The faint end slopes we find are $\beta = -1.73 \pm 0.11$ at $z \sim 3.2$ and $\beta = -1.72 \pm 0.28$ at $z \sim 4$, similar to those found at lower redshift.

4. We compare the luminosity functions derived here with the X-ray luminosity function at $z > 3$ in COSMOS. The optical QLF and the X-ray QLF evolve similarly between $z \sim 3.2$ and $z \sim 4$ in the sense that both show a rapid decline in space density. However, the different normalizations of the LFs imply that roughly 75% of AGN with $\log(L_x) \gtrsim 43.75$ are obscured, type-2 quasars at $z \sim 3 - 4$.

5. We compute the ionizing background due to quasars, both of HeII and HI. The rapid increase in production of HeII ionizing photons from $z \sim 4 \rightarrow 3$ that we find is qualitatively consistent with the observed onset of HeII reionization at $z \sim 3$. However, given the decline of the faint end of the QLF to higher redshift, we conclude that faint quasars are unlikely to contribute substantially to cosmic reionization of hydrogen.

Chapter 3

Physical Properties of Emission-Line Galaxies at $z \sim 2$

3.1 Introduction

The rest-frame optical spectra of star-forming galaxies at all redshifts exhibit emission lines from which detailed physical properties can be inferred. For galaxies at the peak of cosmic star formation at $z \sim 2$, these emission lines are shifted into the near-infrared, which, combined with the intrinsic faintness of the sources, makes them difficult to observe from the ground. For this reason, relatively few near-infrared spectra of galaxies at $z \sim 2$ that cover all of the important rest-frame optical emission lines have been published to date (e.g., Erb et al. 2006; Hainline et al. 2009; Erb et al. 2010; Rigby et al. 2011; Belli et al. 2013).

The available near-infrared spectra of star-forming galaxies at $z \sim 2$ have revealed differences in comparison with counterparts in the local universe (Liu et al. 2008; Newman et al. 2013). For example, in the conventional Baldwin, Phillips & Terlevich (BPT) diagram, star-forming galaxies at $z \sim 2$ tend to have higher [O III]/Hβ

ratios at a given [N II]/Hα ratio than local star-forming galaxies. This observation has been attributed to more extreme interstellar medium (ISM) conditions, on average, in galaxies at high redshift, possibly as a result of higher nebular electron densities, harder ionizing radiation fields, different gas volume filling factors, or some combination of these (Shapley et al. 2005; Brinchmann et al. 2008b; Shirazi et al. 2013; Kewley et al. 2013a,b). The clumpy morphology and relatively high velocity dispersions observed in many of these sources (Pettini et al. 2001; Förster Schreiber et al. 2006; Genzel et al. 2008; Law et al. 2009) may support the conjecture that star-formation in the early universe generally occurs in denser and higher pressure environments than those found in local star-forming galaxies. Significant contribution of active galactic nuclei (AGN) to emission line fluxes for $z \sim 2$ galaxies has also been suggested as a source of the elevated line ratios (Trump et al. 2011, 2013).

The slitless grism spectroscopy provided by the Wide Field Camera 3 (WFC3) on the Hubble Space Telescope (HST) has enabled the discovery of large numbers of star-forming galaxies near the peak of cosmic star formation (Atek et al. 2010, 2011; Straughn et al. 2011; van der Wel et al. 2011; Trump et al. 2011; Brammer et al. 2012). Grism surveys such as the WFC3 Infrared Spectroscopic Parallels (WISP) survey (Atek et al. 2010) are well-suited to finding low-mass star-forming galaxies at intermediate redshifts through their optical emission lines. While WFC3 grism spectroscopy detects large numbers of emission-line galaxies, it is not ideal for extracting the physical information encoded in their optical spectra. The spectral resolution ($R \sim 130$ in G141 and $R \sim 210$ in G102) is insufficient to resolve Hα from [N II]λ6548, 6583, or detect line broadening due to AGN activity. Moreover, despite the broad wavelength coverage (~0.8–1.7 μm) of the grism, Hα is not detected for galaxies at $z \gtrsim 1.6$ and important metallicity diagnostics such as $R_{23} \equiv$ ([O III]$\lambda 4959, 5007$+[O II]λ3727)/Hβ are often inaccessible.

For these reasons, ground-based spectroscopy with the new generation of near-infrared spectrometers is required to constrain the physical properties of these galaxies.

Here we present rest-frame optical spectroscopy of 26 emission-line galaxies from WISP obtained with the Folded-port Infrared Echellette (FIRE, Simcoe et al. 2008, 2010) on the Magellan Baade 6.5 meter telescope. The sample consists of 13 sources at $z \sim 2.2$ and 13 at $z \sim 1.5$. Galaxies in the sample were selected from the WISP survey based on the detection of strong [O III]λ5007 emission (at $z \sim 2.2$) or Hα (at $z \sim 1.5$) in the G141 grism data. Follow-up near-IR spectroscopy with FIRE enables us to: (1) detect Hα for sources at $z > 1.6$ and split Hα and [N II] in order to determine star formation rates (SFRs), (2) get accurate dust reddening estimates using the Balmer decrement, (3) infer metallicities and ionization parameters from strong lines, (4) measure diagnostic line ratios to test for nuclear activity, and (5) resolve emission line velocity dispersions. We also construct composite spectra from our sample, which allow us to investigate the statistical physical properties of strongly star-forming galaxies at $z \sim 2.2$ and $z \sim 1.5$ in greater detail.

This chapter is based on Masters et al. 2014 (ApJ in press) and is structured as follows. In §3.2 we provide an overview of the WISP survey and the emission-line galaxies selected for follow-up spectroscopy. In §3.3 we discuss the Magellan FIRE spectroscopy and data reduction. In §3.4 we present the physical properties measured from the FIRE spectra, including dust obscuration, metallicity, ionization parameter, star formation rate and kinematics. In §3.5 we discuss the composite spectrum derived from the sample. In §3.6 we analyze the results, exploring the implications of our findings for the nature of starbursting galaxies at $z \sim 2$. In §3.7 we conclude with a discussion. We adopt a cosmology with $\Omega_M = 0.3$, $\Omega_\Lambda = 0.7$ and $H_0 = 70$ km s^{-1} Mpc^{-1}.

3.2 WFC3 data & sample selection

3.2.1 The WISP survey

The WISP team (PI Malkan, Atek et al. 2010) is obtaining slitless, near-infrared grism spectroscopy over 0.8–1.7 μm using the two infrared grisms installed on the IR channel of Wide Field Camera 3 (WFC3; Kimble et al. 2008), with more than 800 arcmin^2 of sky covered at present. WFC3 grism observations are highly sensitive to emission-line galaxies over $0.3 \lesssim z \lesssim 2.3$, without suffering from the observational biases affecting ground-based surveys at these redshifts.

WISP is a "pure parallel" program, which means that the WFC3 pointings are determined by primary observing programs using other HST instruments. The WFC3 observations are taken in a parallel field determined by the offset of the instruments on the focal plane and the roll angle of the telescope. WISP consists of two types of observations: a deep survey for parallel targets with more than four orbits of visibility, covering a relatively small number of fields, and a shallower survey for parallel targets with one to three orbits of visibility, covering a much larger number of fields. Parallel observing targets are selected at galactic latitudes $|b| > 20°$ with a preference for longer visibility times. Typical integration times for a 4–5 orbit target are ∼5000 sec in G102 and ∼2000 sec in G141. Longer parallel opportunities are also imaged in F110W and UVIS (the F475X and/or F600LP filters). The shallower WISP fields are restricted to the G141 grism and H-band imaging, with a typical G141 integration time for a 2-orbit target of ∼4000 sec. Because the 2–3 orbit pointings typically achieve deeper G141 integrations and cover a larger area than the deep survey, a substantial fraction of the emission-line galaxies studied here were selected in these fields.

Table 3.1. Overview of the emission-line galaxies from the WISP survey selected for follow-up near-IR spectroscopy with FIRE.

Obj ID	R.A. (J2000)	Decl. (J2000)	z	EW([O III])[a] (Rest Å)	EW(Hα)[a] (Rest Å)	F110W (AB mag)	F140W/F160W (AB mag)
WISP159_134	20:56:30.91	–04:47:56.3	1.300	···	314 (36)	···	22.82 (0.03)
WISP134_171	18:42:33.21	–68:58:37.4	1.354	124 (6)	266 (11)	···	22.55 (0.02)
WISP50_65	22:22:15.86	+09:36:47.1	1.437	···	202 (15)	···	22.35 (22.06)
WISP173_205	01:55:23.64	–09:03:10.2	1.444	982 (146)	603 (42)	···	23.71 (0.03)
WISP9_73	12:29:43.35	+07:48:35.9	1.454	233 (9)	221 (12)	22.80 (0.02)	22.79 (0.02)
WISP43_75	21:04:06.18	–07:22:28.6	1.482	···	137 (14)	22.62 (0.16)	22.37 (0.02)
WISP25_53	10:08:44.82	+07:10:20.4	1.486	···	130 (7)	···	22.20 (0.01)
WISP46_75	22:37:56.48	–18:42:46.1	1.504	···	245 (28)	···	22.77 (0.20)
WISP126_90	13:41:49.16	+05:03:06.2	1.536	···	···	···	22.26 (0.02)
WISP22_111	08:52:46.09	+03:09:19.4	1.541	87 (15)	···	···	22.60 (0.03)
WISP22_216	08:52:46.29	+03:08:45.9	1.543	99 (8)	···	···	23.93 (0.06)
WISP64_2056	14:37:30.20	–01:50:51.4	1.610	···	···	27.45 (0.20)	25.12 (0.20)
WISP81_83	01:10:06.69	–02:23:06.5	1.677	122 (11)	···	23.11 (0.20)	23.30 (0.06)
WISP138_173	15:45:31.03	+09:33:30.0	2.158	286 (22)	···	···	23.48 (0.05)
WISP170_106	00:12:28.18	–10:28:33.6	2.165	154 (7)	···	···	23.31 (0.03)
WISP64_210	14:37:28.34	–01:49:54.4	2.177	143 (14)	···	24.55 (0.05)	23.66 (0.06)
WISP204_133	11:19:46.37	+04:10:30.8	2.191	226 (44)	···	···	23.93 (0.05)
WISP27_95	11:33:08.67	+03:28:27.0	2.192	150 (14)	···	23.66 (0.25)	23.03 (0.05)
WISP147_72	23:58:22.06	–10:14:48.7	2.196	131 (16)	···	22.99 (0.01)	22.03 (0.02)
WISP90_58	01:00:56.20	+02:25:54.0	2.212	71 (4)	···	···	22.53 (0.02)
WISP70_253	04:02:02.50	–05:37:19.5	2.215	257 (23)	···	···	24.67 (0.48)
WISP175_124	03:42:19.72	–20:33:17.1	2.216	271 (18)	···	···	23.74 (0.05)
WISP96_158	02:09:26.37	–04:43:29.0	2.234	238 (10)	···	24.08 (0.31)	23.61 (0.04)
WISP138_160	15:45:36.29	+09:34:26.7	2.264	116 (4)	···	···	23.30 (0.03)
WISP56_210	16:16:50.44	+06:36:38.0	2.304	372 (13)	···	···	23.84 (0.03)
WISP206_261	10:34:17.56	–28:30:49.8	2.315	210 (28)	···	···	24.26 (0.08)

[a]Rest-frame equivalent widths derived from the WFC3 G141 grism data.

3.2.2 Source selection

We select galaxies in WISP fields at $z \sim 2.2$ and $z \sim 1.5$ with clearly detected emission lines. These redshifts were chosen because Hα and other important rest-frame optical emission lines are redshifted into relatively clear atmospheric windows for ground-based near-IR spectroscopy. To find the candidates, the WFC3 2D G141 grism frames were examined carefully to identify sources with the prominent [O III]λ4959, 5007 emission line complex and/or Hα for sources at $z \sim 1.5$. Line fluxes were measured to ensure that FIRE spectroscopic follow-up would be feasible; all sources were required to have [O III]λ5007 or Hα fluxes greater than 5×10^{-17} erg cm^{-2} s^{-1}. The WFC3 data for the emission-line galaxy sample are summarized in Table 3.1, and examples of the WFC3 H-band direct imaging and G141 2D spectra are shown in Figure 3.1.

The grism selection used here is particularly sensitive to star-forming galaxies with high equivalent width (EW) emission lines, which tends to favor lower mass, younger systems, with high specific star formation rates (sSFRs). The relation of our emission-line galaxy selection to galaxies selected using photometric techniques at similar redshifts, for example the "BX/BM" (Steidel et al. 2004), "BzK" (Daddi et al. 2004) and UV-dropout (Hathi et al. 2010) samples, is uncertain. It has been shown previously that the different color cut prescriptions non-uniformly sample the true population of galaxies (Reddy et al. 2005; Quadri et al. 2007; Grazian et al. 2007; Ly et al. 2011), although there is large overlap between the galaxies selected with each method. The overlap of our sample with the UV color-selected galaxies at similar redshift is likely high, although the grism-selected emission-line sample can probe lower mass galaxies due to its relative insensitivity to the galaxy continuum.

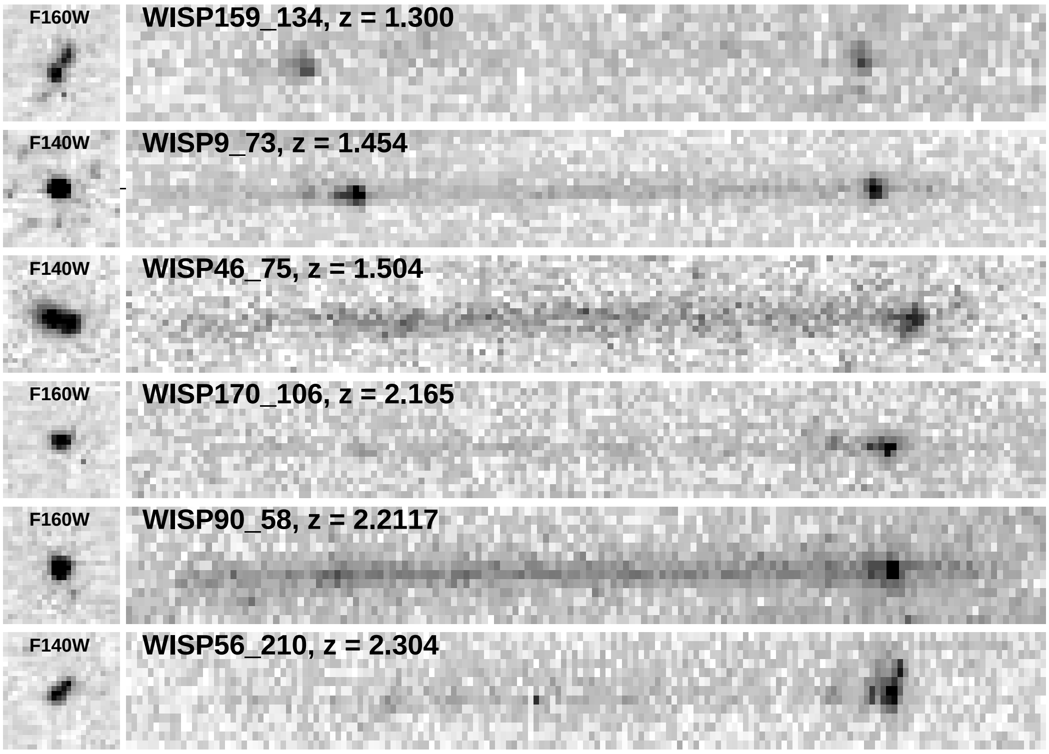

Figure 3.1 Examples of the WISP sources selected for follow-up Magellan FIRE spectroscopy. The direct WFC3 H-band images on the left are $3''$ on a side. Prominent rest-frame optical emission lines are visible in the G141 grism exposures, which span 1.1-1.7 μm.

3.3 Magellan FIRE near-IR spectroscopy

3.3.1 Observations & data reduction

Observations with Magellan FIRE were conducted over six observing runs from April 2011 to March 2013. FIRE was used in high-resolution echelle mode to give near-infrared spectra spanning $\sim 1.0 - 2.5$ μm. The success rate was nearly 100% for the candidates, with the only non-detections occurring in poor observing conditions. Observations were conducted as follows. The J-band acquisition camera was used to locate a nearby star from which a blind offset was applied to position the science target in the slit. The slits used were either 0.6″, 0.75″ or 1.0″ in width, depending on the seeing, and were oriented at the parallactic angle in most cases to minimize differential atmospheric refraction. Exposure times of 900 seconds were used for sequences of ABBA dither sequences with total integrations ranging from 1 to 3.5 hours. Readouts were performed with the Sample Up The Ramp (SUTR) mode in order to minimize overheads. For each science target, at least one A0V star was observed at similar airmass for telluric correction.

Data were reduced using the publicly available pipeline[†] developed by the instrument team. A brief summary of the reduction process follows. First, the edges of the 2D echelle orders were traced and the flat field was derived using a combination of internal quartz lamp exposures and sky flat exposures. ThAr arc lamp exposures were used to derive the wavelength solution, which was then refined using the OH sky lines from the science frames. Sky subtraction was performed using the method described in Kelson (2003). In most cases optimal extraction was used to derive the 1D spectrum from the 2D frames, after fitting a spatial profile to a prominent emission line in a 2D frame. The 1D spectra were flux calibrated using observations of an A0V telluric standard star, and then combined to obtain the final, flux calibrated 1D spectrum.

3.3.1.1 Improvements to reduction pipeline

The publicly available pipeline for FIRE reduction uses an assortment of existing IDL code for reducing spectra, modified to work with the echelle data. In the process of using the code, we discovered a number of issues, and made improvements when necessary. As an example, one relatively major improvement involved the sky subtraction,

[†] http://web.mit.edu/~rsimcoe/www/FIRE/ob_data.htm

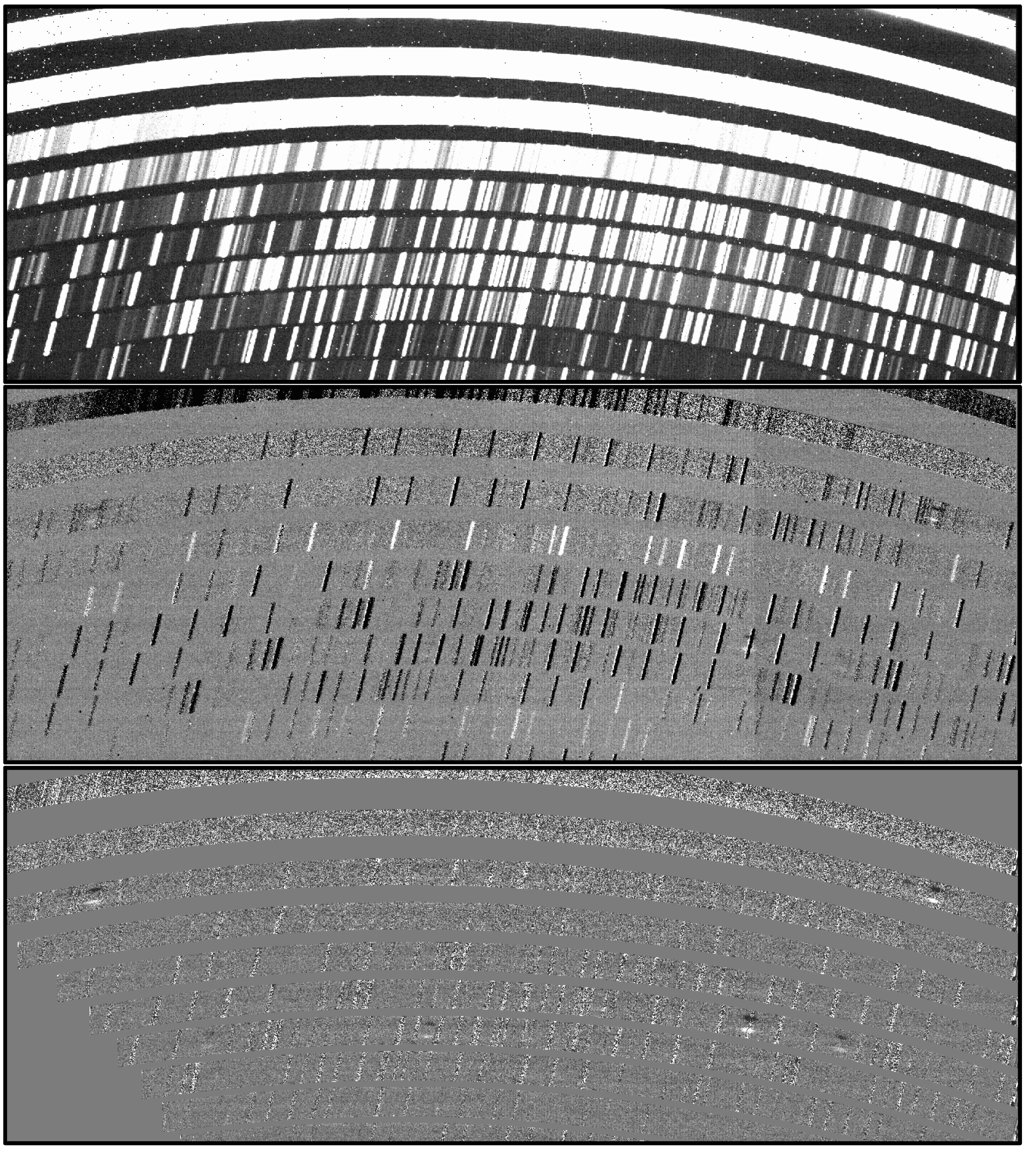

Figure 3.2 Example FIRE 2D data for WISP90_58. *Top:* Raw FIRE 2D exposure showing wavelengths corresponding to H and K band. *Middle:* The same frame after subtracting a dithered exposure. The sky OH line and thermal background is greatly reduced through this crude subtraction, revealing clear emission features including [O III] and Hα. *Bottom:* Coadd of five sky-subtracted A position frames, after subtracting off five coadded, sky-subtracted B position frames. The emission lines are obvious and the sky background is greatly reduced.

when using the optimal extraction method. We discovered that the object was not being masked properly when estimating the sky level, leading to significant over-subtraction of the sky in these regions. Figure 3.3 illustrates the improvement in sky subtraction in the region of an emission line we were able to achieve by implementing a fix to correctly mask the emission line while estimating the sky level.

Examples of reduced FIRE 1D spectra are shown in Figures 3.4 and 3.5, and the entire sample is shown in Appendix B.

3.3.1.2 Absolute flux calibration

The emission line fluxes measured from the FIRE 1D spectra frequently were lower by a factor of 2-4 compared to the same lines measured from the G141 grism spectra. When multiple lines were measured with both instruments, for example [O III]λ5007 and Hα for galaxies at $z \sim 1.5$, the ratio of the FIRE and WFC3 line fluxes was found to be consistent for the two lines to within 20%, indicating that the relative calibration of FIRE is reliable. The exact reason for the absolute offset is unclear, but is probably a combination of slit losses in FIRE and difficulty in deriving the absolute correction for sources with essentially no detected continuum.

For the majority of the analysis presented here we do not require absolute line flux values, but to infer SFRs for the sample we do need to know the absolute flux of Hα. We use the WFC3 measurements to derive the absolute Hα flux. For galaxies at $z \sim 1.5$ we take the WFC3-measured $F(\mathrm{H}\alpha)$ as the reference value, after correcting for blended $F([\mathrm{N\ II}])$ as measured from the FIRE spectrum. For galaxies at $z \sim 2.2$, Hα was not measured with WFC3, so we scale the measured FIRE $F(\mathrm{H}\alpha)$ by the ratio of the WFC3-measured $F([\mathrm{O\ III}])$ to the FIRE-measured $F([\mathrm{O\ III}])$, which is justified given

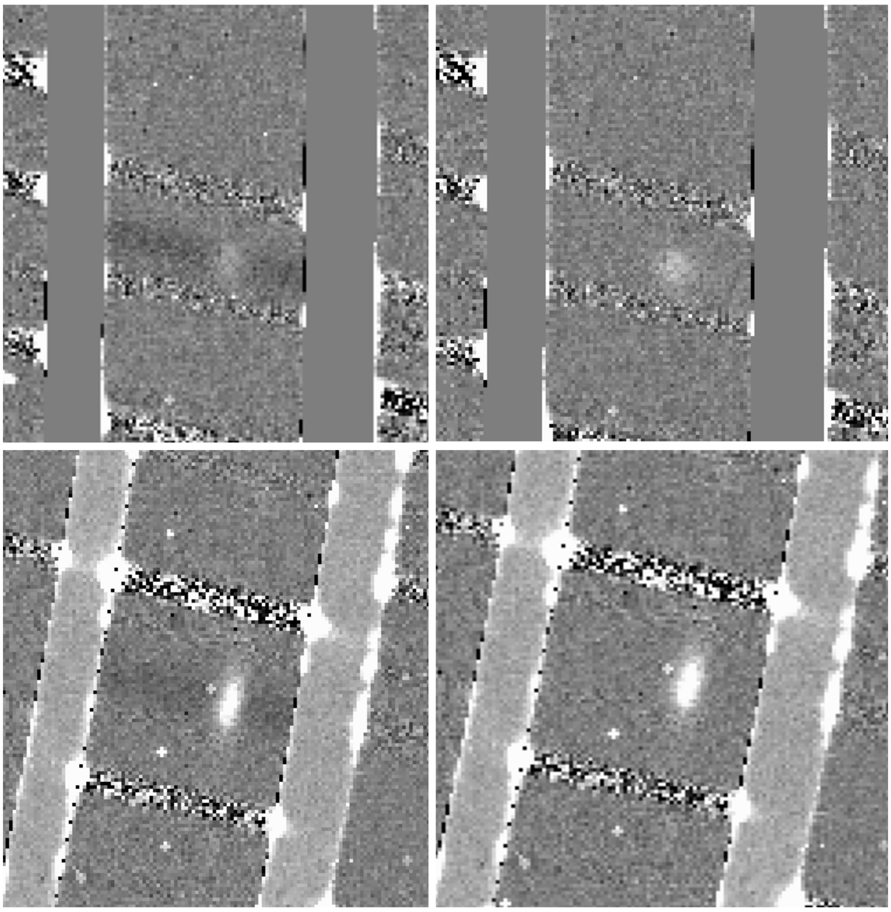

Figure 3.3 On the left are emission lines with sky subtraction performed using the unmodified pipeline. A clear over-subtraction in the region of the line is evident, indicating that the flux of the line itself is being included in the sky estimate. We investigated this issue and found a fix. The improved sky subtraction is shown on the right for the same lines.

the consistent relative calibrations of the two instruments.

3.3.2 Line measurement

We fit the emission lines with Gaussian profiles using the IDL MPFIT routines (Markwardt 2009). Errors in the derived line fluxes and velocity dispersions were determined using Monte Carlo simulations in which the lines were fit repeatedly after

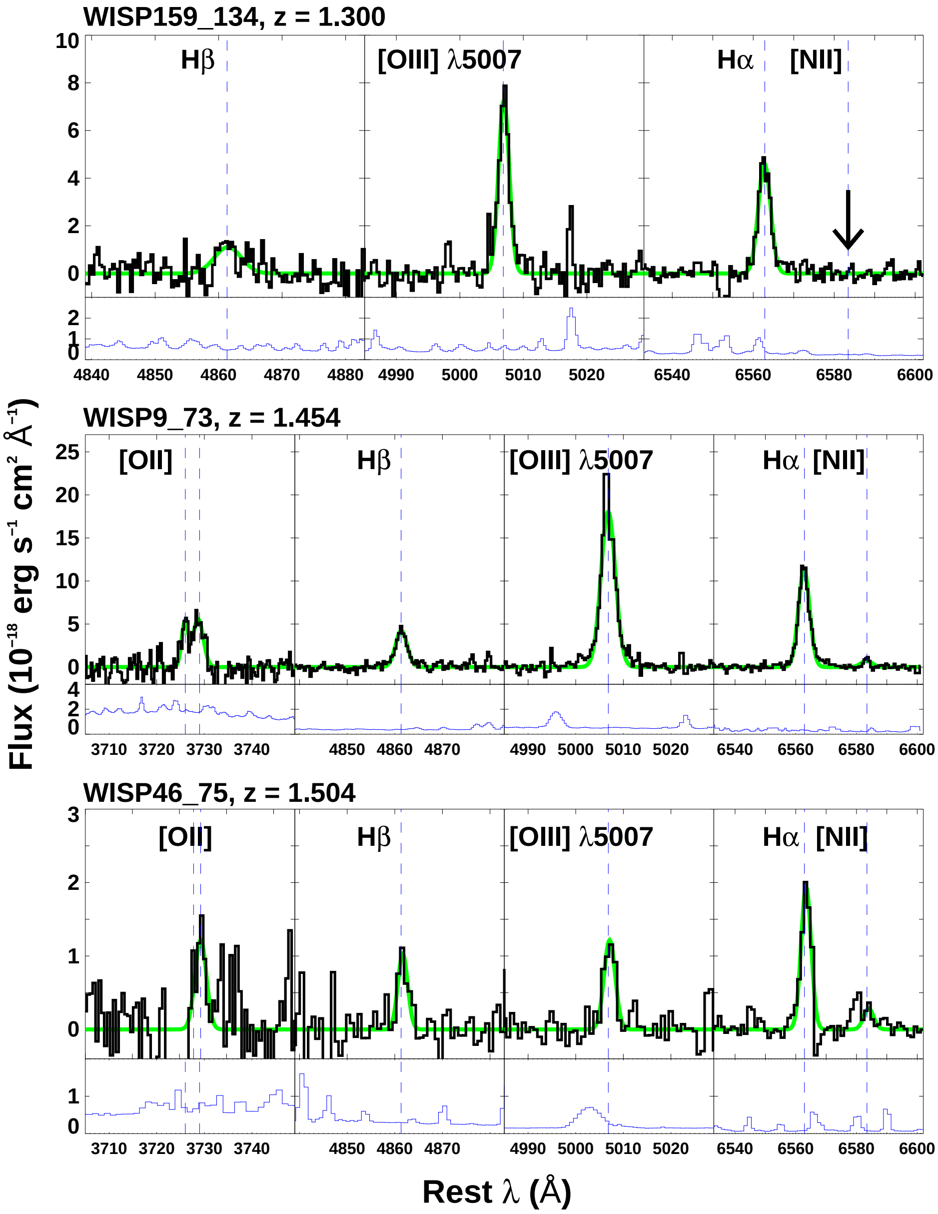

Figure 3.4 Example 1D spectra from Magellan FIRE, for the $z \sim 1.5$ sources shown in Figure 3.1. Fits are overlaid in green and the emission lines are labeled. Downward arrows indicate non-detections. The lower panels show the error spectra. The appendix contains WFC3 and FIRE data for all objects in the sample.

applying gaussian noise consistent with the error spectrum. The [N II]λ6583 flux was fit simultaneously with Hα while fixing the width and separation of the two lines. For non-

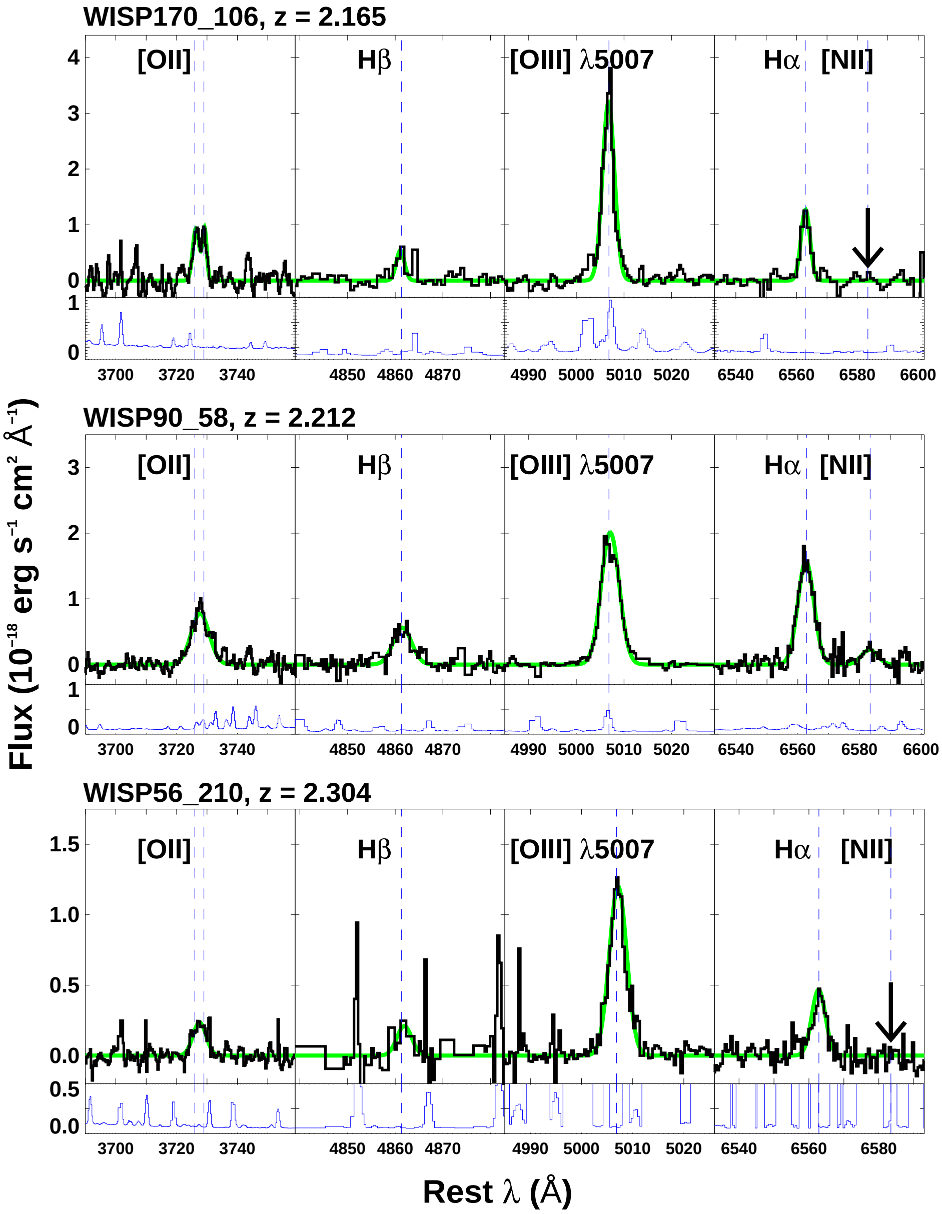

Figure 3.5 Example 1D spectra from Magellan FIRE, for the $z \sim 2.2$ sources shown in Figure 3.1.

detected [N II]λ6583, the 95% confidence upper limit on the flux was determined with a Monte Carlo simulation in which noise was added to the spectrum and the [N II] flux was fit repeatedly as described. The resulting distribution of [N II] fluxes determined the 2σ upper limit. This limit was verified by adding in and attempting to recover known fluxes in empty regions of the spectrum near [N II]λ6583.

The instrumental resolution of FIRE was determined by measuring the FWHM values of multiple ThAr lines. This was done for slit widths of 0.6$''$, 0.75$''$, and 1.0$''$, giving FWHM resolutions of 59, 65.5, and 72 km s^{-1}, respectively. These values would be appropriate for galaxies that fill the slit uniformly; in reality the FWHM resolution may be lower depending on the light profile of the target. Galaxy line widths are considered to be resolved when the measured FWHM of the line was at least twice the instrumental resolution. We find that all of the emission lines are resolved. Measured line fluxes are presented in Table 3.2 and the velocity dispersions for [O III]λ5007 and Hα are presented in Table 3.5.

3.4 Physical properties

3.4.1 Dust extinction

Dust preferentially attenuates shorter-wavelength light and must be taken into account when deriving physical properties from emission lines. We use the ratio Hα/Hβ (the Balmer decrement) to estimate the nebular dust extinction of galaxies in the sample. The Balmer decrement is relatively insensitive to temperature and should equal 2.86 in the absence of dust, given reasonable assumptions for the physical conditions of the H II regions producing the line emission (Osterbrock & Ferland 2006).

In computing the nebular extinction from the Balmer decrement we follow the method outlined in Momcheva et al. (2013) and Domínguez et al. (2013), which uses the extinction curve of Calzetti et al. (2000) to convert the observed Balmer decrement into $E(B-V)$ and total extinction values. The Balmer decrements we measure for the

Table 3.2. Line fluxes derived from the FIRE near-IR spectroscopy.

Object ID	$F([\text{O II}]\lambda3727)^{a}$	$F(\text{H}\beta)$	$F([\text{O III}]\lambda5007)$	$F(\text{H}\alpha)$	$F([\text{N II}]\lambda6583)$
WISP159_134	···	13.5 (3.4)	35.6 (1.3)	40.3 (2.3)	<1.3
WISP134_171	···	···	106 (3.6)	68.3 (1.5)	7.4 (1.1)
WISP50_65	11.7 (2.1)	2.8 (1.1)	10.7 (1.1)	19.3 (0.5)	6.6 (0.3)
WISP173_205	8.9 (2.2)	7.5 (0.4)	47.0 (0.7)	22.3 (0.4)	···
WISP9_73	59.4 (7.5)	31.6 (1.3)	168 (3.0)	128 (1.0)	8.2 (0.8)
WISP43_75	···	88.8 (4.8)	···	296 (37)	76.8 (20)
WISP25_53	65.9 (3.0)	31.0 (0.9)	78.9 (0.8)	86.9 (0.9)	15.8 (0.9)
WISP46_75	18.5 (3.7)	6.6 (1.1)	9.0 (0.5)	20.1 (0.7)	3.0 (0.3)
WISP126_90	···	3.8 (0.7)	···	21.9 (0.4)	8.7 (1.1)
WISP22_111	···	7.5 (1.4)	26.8 (3.3)	21.0 (0.5)	5.3 (1.0)
WISP22_216	···	11.7 (0.7)	53.6 (1.5)	32.7 (1.6)	< 0.5
WISP64_2056	14.3 (8.0)	···	30.6 (0.4)	16.9 (0.4)	< 0.6
WISP81_83	···	···	220 (4.1)	136 (1.6)	···
WISP138_173	9.2 (0.5)	2.7 (0.3)	14.5 (0.6)	16.0 (1.3)	<1.0
WISP170_106	13.2 (1.6)	3.7 (0.4)	32.0 (1.4)	15.0 (0.5)	< 1.3
WISP64_210	29.9 (1.9)	20.1 (1.4)	136 (2.3)	84.5 (3.5)	15.1 (3.7)
WISP204_133	4.3 (0.8)	2.6 (0.3)	5.7 (0.7)	3.9 (0.4)	< 0.9
WISP27_95	50.0 (1.4)	18.6 (0.7)	91.0 (0.7)	77.5 (1.2)	9.6 (1.2)
WISP147_72	14.4 (7.8)	···	86.5 (0.5)	20.2 (0.7)	1.3 (0.6)
WISP90_58	18.7 (0.8)	8.7 (0.3)	30.7 (0.5)	33.0 (0.8)	4.7 (0.4)
WISP70_253	4.1 (0.6)	7.3 (0.3)	30.1 (0.2)	14.0 (0.6)	< 0.6
WISP175_124	13.1 (0.7)	···	38.1 (0.3)	25.4 (0.9)	2.5 (0.4)
WISP96_158	19.7 (2.5)	9.0 (1.6)	94.4 (2.3)	44.9 (1.8)	< 2.9
WISP138_160	···	49.8 (5.7)	256 (1.6)	170 (1.5)	14.6 (1.2)
WISP56_210	4.2 (0.3)	2.7 (0.4)	16.9 (0.7)	7.5 (1.2)	···
WISP206_261	6.9 (1.5)	7.4 (0.5)	49.1 (0.4)	30.3 (0.9)	< 1.1

[a]All fluxes are in units of 10^{-18} erg cm^{-2} s^{-1}. Fluxes presented here have not been scaled to match WFC3 fluxes, as described in §3.1.

Table 3.3. Balmer decrements, extinctions, and SFRs for the sample.

Object ID	Hα/Hβ	E(B-V) (mag)	F(Hα) scaled[a]	F(Hα) ext. corr.[b]	SFR (uncorr.) $M_{\odot}$ yr^{-1}	SFR (corr.) $M_{\odot}$ yr^{-1}
WISP159_134	2.99 (0.76)	$0.04^{+0.24}_{-0.00}$	14.2 (0.95)	$16.1^{+29.7}_{-14.0}$	6.6 (0.5)	$7.5^{+13.8}_{-6.5}$
WISP134_171	···	···	22.6 (0.78)	···	11.6 (0.4)	···
WISP50_65	6.97 (2.70)	$0.76^{+1.09}_{-0.46}$	10.0 (0.9)	103^{+283}_{-41}	6.0 (0.5)	62^{+169}_{-25}
WISP173_205	2.96 (0.16)	$0.03^{+0.08}_{-0.00}$	11.2 (0.6)	$12.3^{+14.4}_{-11.1}$	6.8 (0.4)	$7.4^{+8.7}_{-6.7}$
WISP9_73	4.05 (0.17)	$0.30^{+0.34}_{-0.26}$	18.7 (0.8)	$46.9^{+53.1}_{-41.5}$	11.5 (0.5)	29^{+33}_{-25}
WISP43_75	3.36 (0.45)	$0.14^{+0.25}_{-0.03}$	29.6 (3.7)	$45.5^{+64.1}_{-31.9}$	19.1 (2.4)	29^{+41}_{-21}
WISP25_53	2.80 (0.09)	$0.00^{+0.03}_{-0.00}$	15.0 (0.7)	$15.0^{+16.6s}_{-14.3}$	9.8 (0.5)	$9.8^{+10.8}_{-9.3}$
WISP46_75	3.03 (0.50)	$0.05^{+0.19}_{-0.00}$	13.6 (1.3)	$15.9^{+24.5}_{-13.3}$	9.1 (0.9)	$10.6^{+16.4}_{-8.9}$
WISP126_90	5.81 (1.01)	$0.61^{+0.76}_{-0.46}$	···	···	···	···
WISP22_111	2.80 (0.54)	$0.00^{+0.16}_{-0.00}$	7.58 (0.16)	$7.58^{+12.4}_{-7.42}$	5.4 (0.1)	$5.4^{+8.8}_{-5.3}$
WISP22_216	2.79 (0.22)	$0.00^{+0.04}_{-0.00}$	9.58 (0.46)	$9.58^{+10.9}_{-9.12}$	6.8 (0.4)	$6.8^{+7.8}_{-6.5}$
WISP64_2056	···	···	7.68 (0.17)	···	6.1 (0.1)	···
WISP81_83	···	···	1.14 (0.01)	···	1.0 (0.01)	···
WISP138_173	5.86 (0.85)	$0.61^{+0.73}_{-0.49}$	9.43 (0.78)	$61.2^{+88.5}_{-42.4}$	15.3 (1.2)	99^{+144}_{-69}
WISP170_106	4.05 (0.44)	$0.30^{+0.39}_{-0.21}$	6.89 (0.24)	$17.3^{+22.8}_{-13.1}$	11.3 (0.4)	28^{+37}_{-21}
WISP64_210	4.20 (0.34)	$0.33^{+0.40}_{-0.26}$	7.77 (0.32)	$21.4^{+26.5}_{-17.2}$	12.9 (0.5)	35^{+44}_{-28}
WISP204_133	1.52 (0.25)	$0.00^{+0.00}_{-0.00}$	3.61 (0.36)	$3.61^{+3.97}_{-3.25}$	6.1 (0.6)	$6.1^{+6.7}_{-5.5}$
WISP27_95	4.17 (0.18)	$0.32^{+0.36}_{-0.28}$	12.0 (0.2)	$32.0^{+36.2}_{-28.3}$	20.2 (0.4)	54^{+61}_{-48}
WISP147_72	···	···	8.27 (0.29)	···	14.0 (0.5)	···
WISP90_58	3.79 (0.16)	$0.24^{+0.28}_{-0.20}$	15.4 (0.4)	$32.2^{+36.3}_{-28.4}$	26.5 (0.6)	56^{+63}_{-49}
WISP70_253	1.92 (0.11)	$0.00^{+0.00}_{-0.00}$	3.38 (0.13)	$3.38^{+3.52}_{-3.25}$	5.8 (0.2)	$5.8^{+6.2}_{-5.6}$
WISP175_124	···	···	9.53 (0.33)	···	16.5 (0.6)	···
WISP96_158	5.01 (0.93)	$0.48^{+0.64}_{-0.32}$	6.09 (0.25)	$26.5^{+43.4}_{-16.2}$	10.8 (0.5)	47^{+77}_{-28}
WISP138_160	3.41 (0.39)	$0.15^{+0.25}_{-0.05}$	13.3 (0.1)	$21.1^{+28.6}_{-15.5}$	24.2 (0.3)	38^{+52}_{-29}
WISP56_210	2.80 (0.64)	$0.00^{+0.16}_{-0.00}$	10.3 (1.6)	$10.3^{+17.0}_{-8.66}$	19.6 (3.1)	20^{+32}_{-16}
WISP206_261	4.08 (0.31)	$0.30^{+0.36}_{-0.24}$	5.57 (0.17)	$14.0^{+16.8}_{-11.6}$	10.7 (0.4)	27^{+32}_{-22}

[a]This is the FIRE flux scaled to WFC3 as described in §3.1, accounting for the uncertain absolute calibration of the FIRE data. The units are 10^{-17} erg cm^{-2} s^{-1}.

[b]Scaled F(Hα) extinction corrected using the $E(B\text{-}V)_{gas}$ derived from the Balmer decrement.

sample and the derived $E(B-V)$ and $A_{H\alpha}$ values are given in Table 3.3. The nebular extinctions for the sample are generally low, ranging from no evidence for extinction up to $A_{H\alpha} = 2.53$ mags, with an average extinction of $A_{H\alpha} = 0.7$ mags. In this analysis we do not correct for the possible effect of stellar absorption lines on the measured line fluxes due to the lack of reliable continuum measurements for most objects. This may affect the measured Balmer decrements and lead to slightly overestimated dust extinctions, but the effect will be small for high-EW galaxies. For example, the typical equivalent width of the stellar absorption in Hβ is 3-4 Å (see, e.g., Domínguez et al. 2013), whereas the equivalent widths of the Hβ lines in this sample are likely to be $\gtrsim 30$ Å judging from the measured EW([O III]) values and [O III]/Hβ ratios. We conclude that the effect will not have a substantial impact on the results.

On the left panel of Figure 3.6 we show the Balmer decrement as a function of the observed Hα luminosity (which was scaled to account for the uncertain absolute FIRE calibration, as described in §3.1.1). There is no obvious trend between the Balmer decrement and the observed $L_{H\alpha}$, which is unsurprising given the relatively narrow range of observed Hα luminosities in our sample. Nevertheless, the Balmer decrements we find for $\log_{10}(L_{H\alpha}) \sim 42-42.5$ erg s^{-1} are in good agreement with those found by Domínguez et al. (2013) using stacked WFC3 spectra from WISP.

On the right panel of Figure 3.6 we show the inferred $E(B-V)$ values plotted against the extinction-corrected Hα luminosities. There is circularity in this plot, in that the reddening on the y-axis was used to estimate the correction for the Hα luminosity on the x-axis. If taken at face value, a clear trend is evident, with the galaxies that are more luminous in Hα having more dust extinction. This result is consistent with the trend seen at both low and high redshift that more luminous galaxies tend to have more

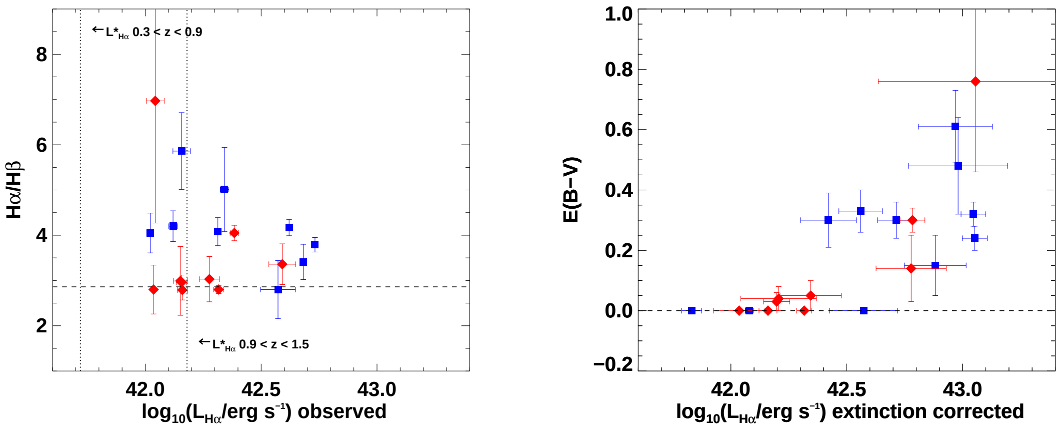

Figure 3.6 Balmer decrement as function of Hα luminosity, observed (left) and corrected for extinction (right). The blue squares are from the $z \sim 2.2$ sample and the red diamonds are from the $z \sim 1.5$ sample. There is no trend evident on the left, but the values measured are consistent with the results from Domínguez et al. (2013) for this somewhat narrow range of observed $L_{\mathrm{H}\alpha}$. We indicate with dotted lines the values of $L^*_{\mathrm{H}\alpha}$ for two lower redshift intervals recently determined by Colbert et al. (2013). On the right we see a clear trend, with more luminous Hα sources showing elevated dust extinctions. It should be noted that this plot is somewhat circular, in that the Balmer decrement is used to obtain the extinction corrected $L_{\mathrm{H}\alpha}$ values.

dust obscuration (Domínguez et al. 2013), as well as with previous studies (e.g., Ly et al. 2011) that have found that the star formation rate density at $z \sim 2$ is dominated by a less numerous population of highly dust-extinguished galaxies. A word of caution is in order, however, as this might be a selection effect due to the grism selection missing obscured sources with lower intrinsic Hα luminosities.

3.4.2 Metallicity

A number of different metallicity calibrations based on emission line strengths have been proposed in the literature (see Kewley & Ellison 2008 for an overview). One of the most commonly used indicators is $R_{23} \equiv$ ([O III]λ4959,5007+[O II]λ3727)/Hβ (Pagel et al. 1979; McGaugh 1991; Kewley & Dopita 2002; Kobulnicky & Kewley 2004). A well-known difficulty with R_{23} is that it is double-valued with 12+log(O/H), making it necessary to determine which "branch" of the R_{23} curve a galaxy is on (Dopita et al. 2013 and references therein). The R_{23} calibration also has a strong dependence on ionization parameter, although this quantity can be measured from the ratio [O III]/[O II] when R23 is observed. Another well-known metallicity indicator is $N2 \equiv \log$([N II]λ6583/Hα) (Pettini & Pagel 2004). This estimator has the advantage of increasing monotonically with metallicity below $12 + \log(\mathrm{O/H}) \sim 9.2$, but is also sensitive to ionization parameter (Kewley & Dopita 2002).

We find unusually large R_{23} values compared with local samples for about half of the sources for which we were able to measure R_{23}. We illustrate this in Figure 3.7, in which the dust-corrected R_{23} values from the FIRE sample are plotted against the ratio log([N II]/Hα). This plot is similar to the BPT diagram, but in this case both axes are commonly-used metallicity indicators. Noteworthy is the offset of many of the FIRE-observed points to higher R_{23} values at a given [N II]/Hα ratio compared with the Sloan Digital Sky Survey (SDSS; Abazajian et al. 2009) data points shown for comparision. Calibrations in the literature generally do not account for such high values. We are relatively confident that the majority of the high R_{23} values are not due to AGN activity, a point that is discussed further in §6.1.

We used the code Inferring Metallicities (Z) and Ionization parameters (IZI, Blanc et al. in prep) to further analyze the sample. This software uses Bayesian inference to compute the joint and marginalized posterior probability distribution functions (PDF) for the metallicity and ionization parameter by comparing the dust-corrected line fluxes

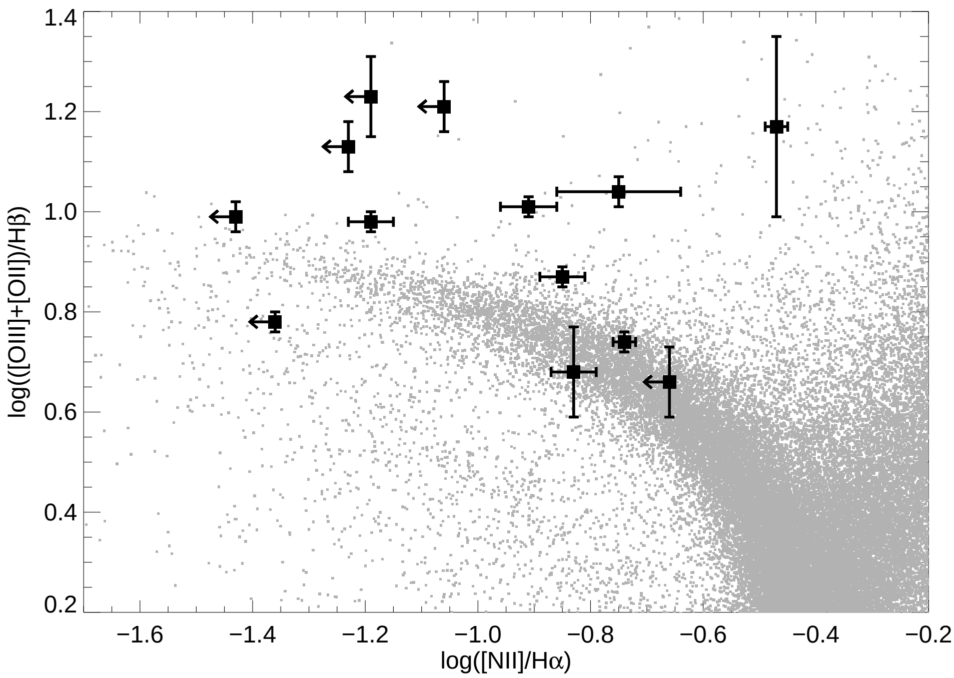

Figure 3.7 $R23$ plotted against $N2$. Both of these quantities are metallicity indicators, and in the FIRE data a hint of a turnover in R23 at low metallicities (low N2 values) is apparent in the two leftmost FIRE points. 60,000 data points from SDSS galaxies are shown for comparison; no turnover in R23 is apparent in this data, but this is because of the combination of the rarity of lower branch galaxies in the local universe and the lack of sensitivity of SDSS to such low-mass sources. Close to half of the galaxies in our sample show higher R_{23} values than found in local star-forming galaxies.

to the predictions of a photoionization model grid. We used the grids of Levesque et al. (2010), which have been recently extended to higher ionization parameter values by Richardson et al. (2013). Again, we find that the model grids are often unable to reproduce the observed lines for those sources with high [O III]/Hα and [O III]/Hβ line ratios.

To estimate metallicities, we use the $N2$ calibration of Pettini & Pagel (2004).

We then use these estimates to determine which branch of the R_{23} curve to adopt when computing the R_{23} metallicity, with the lower branch being used for $N2$ metallicities less than 8.4. The metallicity estimates from R_{23} and $N2$ are given in Table 3.4. In cases for which R_{23} was higher than normal, we approximate the R_{23} metallicity as $12 + \log(\mathrm{O/H}) \sim 8.4$, the value at the nominal turnover of the R_{23} curve.

We find a median ratio [N II]/Hα of ∼10%, in close agreement with the value of ∼12% derived from the overall composite spectrum presented in §5. The $N2$ metallicities of the sample range from <13% solar to roughly solar, with a median of 0.45 $Z_\odot$ ($Z_\odot$=8.69 in units of 12+log(O/H), Asplund et al. 2009). The R_{23} metallicities are similar, with a median metallicity of 0.50 $Z_\odot$. As pointed out by Dopita et al. (2013), R_{23}-based metallicities should be treated with caution, particularly as the ratio is only weakly sensitive to abundance for $8.3 \lesssim 12 + \log(\mathrm{O/H}) \lesssim 9.0$. Therefore, we use the $N2$ metallicities in the analysis that follows, although these can also be problematic.

Both Villar et al. (2008) and Cowie et al. (2011) have shown a strong relationship between the [N II]/Hα ratio and EW(Hα) for star-forming galaxies at lower redshifts. For most of our sample we are unable to determine EW(Hα), but the [N II]/Hα ratios we find are consistent with EW(Hα) values of ∼100–300 as determined by those authors. Based on the few sources for which we do have EW(Hα), this is very reasonable. In Figure 3.8 we plot the [N II]/Hα ratio against EW([O III]λ5007) as a proxy for EW(Hα). A negative correlation of EW([O III]) and log([N II]/Hα) is evident. Assuming EW([O III]) is a rough tracer of age, as is the case for EW(Hα), the increasing [N II]/Hα ratio with decreasing EW([O III]) may reflect a smooth metal buildup with age.

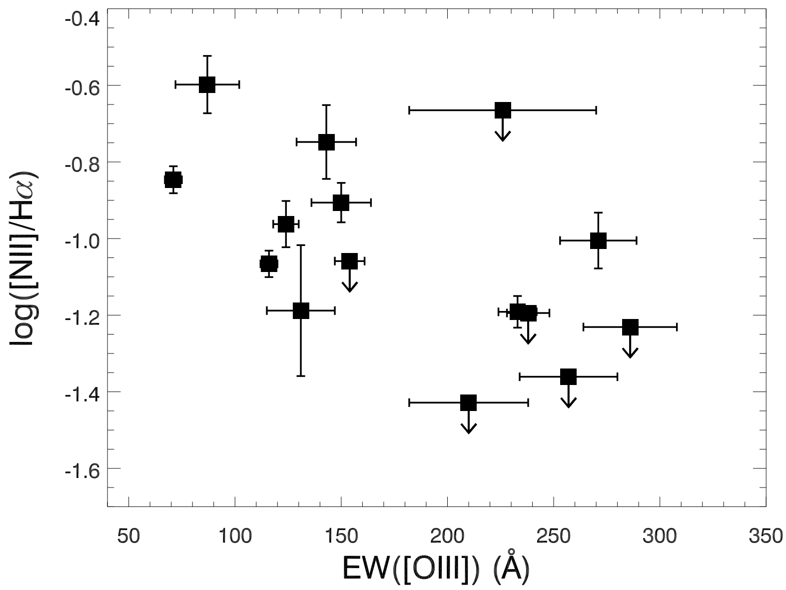

Figure 3.8 The ratio [N ii]/Hα vs. EW([O iii]). A fairly tight negative correlation between [N ii]/Hα and EW(Hα) was shown by Cowie et al. 2011 (Figure 9f). A similar trend is apparent here, with EW([O iii]) as a proxy for EW(Hα).

3.4.2.1 Mass-metallicity relation

The relationship between the gas-phase metallicity and the stellar mass of galaxies has been explored extensively in the literature because it directly constrains models of the interplay between star formation, pristine gas inflows, chemical enrichment of the ISM, and feedback in the form of supernova-driven galactic-scale winds (e.g., Lequeux et al. 1979; Skillman 1989; Zaritsky et al. 1994; Tremonti et al. 2004; Erb et al. 2006; Henry et al. 2013). It is now well-established that a strong positive correlation exists between metallicity and stellar mass in both the local (Tremonti et al. 2004) and high redshift (Erb et al. 2006) universe. This relationship probably reflects the higher gas fractions found in lower mass systems and/or the relative inability of low-mass galaxies to retain metals accelerated by supernova-driven winds. The mass-metallicity relation at $z \sim 2$ was recently explored at lower masses than previously possible using stacked data from the WISP survey (Henry et al. 2013). We explore this regime further using our FIRE data.

On the left panel of Figure 3.9 we show the $N2$ metallicities plotted against the rest-frame V band absolute magnitudes derived from WFC3 H band photometry (either the F140W or F160W filter), corrected for emission line contamination. There is a clear positive correlation between metallicity and luminosity. On the right panel of Figure 3.9 we show the $N2$-based metallicity estimates against rough stellar mass estimates from the WFC3 photometry. The masses were estimated by using a M/L ratio in V band from the Bruzual & Charlot 2003 (BC03) models assuming constant star-formation and an age of 100 Myr. The age was chosen to roughly match the values of EW(Hα) for the sample (the relation between age and EW(Hα) is well-known; see, e.g., Shim et al. 2011). The large error bars primarily reflect the uncertainty in the M/L ratio, which depends on the uncertainty in the age estimates. This was in turn estimated from the likely spread in EW(Hα) values for the sample, as only a handful are directly measured from the WFC3 grism data.

The strong mass-metallicity relation we find is in relatively good agreement with the recent determination by Henry et al. (2013) using stacked WISP data at similar redshift, although that result shows a somewhat higher normalization. We also compare to the determination of the mass-metallicity relation at $z \sim 2$ from Erb et al. (2006) and find that our points show a similar trend but tend to be offset upwards from this relation. This offset may be due to a combination of the somewhat lower average redshift of points in our sample and/or a nitrogen enhancement in the emission-line sample, discussed further in §6.3. Such an enhancement, if real, could bias our $N2$ metallicity

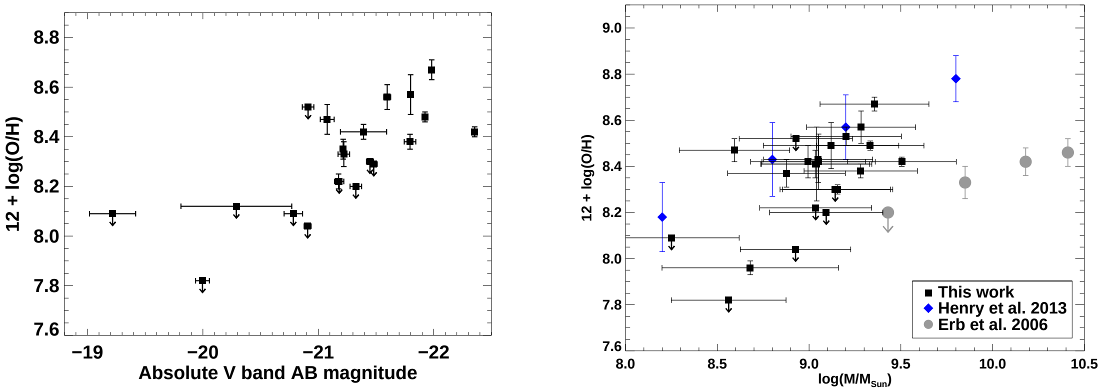

Figure 3.9 *Left:* The $N2$ metallicity vs. absolute magnitude from WFC3 H-band photometry, corresponding to rest-frame optical. The photometry has been corrected for emission line contamination. *Right:* Rough mass estimates from rest-frame optical photometry corrected for emission line flux against the best metallicity estimates. The blue diamonds are from the recent determination of the MZ relation by Henry et al. (2013) using stacked data from WISP.

estimates toward higher values.

3.4.3 Ionization parameter

The ionization parameter q, defined as the ratio of the flux of ionizing photons through a unit area to the local number density of hydrogen nuclei, is frequently used to characterize the radiation field in H II regions. The effective ionization parameter is defined in terms of the Strömgrem radius R_S:

$$q = \frac{Q_{H^0}}{4\pi R_S^2 n} \tag{3.1}$$

where Q_{H^0} is the ionizing photon flux produced by the radiation source(s) and n is the local number density of hydrogen atoms. It is often expressed in terms of the logarithm

Table 3.4. $N2$ and R_{23} metallicity estimates and ionization parameters for the sample.

Object ID	Z^{a} ($N2$)	Z^{a} (R_{23})	$O32$	log U
WISP159_134	< 8.04	···	···	···
WISP134_171	8.35 (0.04)	···	···	···
WISP50_65	···	~ 8.4	-0.46 (0.19)	$-2.98^{+0.07}_{-0.2}$
WISP173_205	···	···	0.71 (0.15)	$-2.20^{+0.63}_{-0.35}$
WISP9_73	8.22 (0.03)	8.44 (0.04)	0.28 (0.19)	$-2.77^{+0.28}_{-0.07}$
WISP43_75	8.57 (0.08)	···	···	···
WISP25_53	8.48 (0.02)	8.81 (0.02)	0.08 (0.25)	$-2.91^{+0.21}_{-0.07}$
WISP46_75	8.42 (0.03)	8.87 (0.09)	-0.34 (0.26)	$-3.26^{+0.21}_{-0.07}$
WISP126_90	8.67 (0.04)	···	···	···
WISP22_111	8.56 (0.05)	···	···	···
WISP22_216	< 7.82	···	···	···
WISP64_2056	< 8.09	···	···	···
WISP81_83	···	···	···	···
WISP138_173	< 8.20	~ 8.4	-0.14 (0.21)	$-2.76^{+0.14}_{-0.14}$
WISP170_106	< 8.30	~ 8.4	0.22 (0.25)	$-2.76^{+0.21}_{-0.14}$
WISP64_210	8.47 (0.06)	~ 8.4	0.47 (0.06)	$-2.41^{+0.14}_{-0.28}$
WISP204_133	< 8.52	8.00 (0.11)	0.12 (0.15)	$-2.91^{+0.28}_{-0.07}$
WISP27_95	8.38 (0.03)	~ 8.4	0.08 (0.15)	$-2.93^{+0.21}_{-0.07}$
WISP147_72	···	···	0.78 (0.30)	$-2.06^{+0.80}_{-0.49}$
WISP90_58	8.42 (0.02)	8.62 (0.03)	0.08 (0.25)	$-2.93^{+0.28}_{-0.09}$
WISP70_253	< 8.12	7.96 (0.03)	0.86 (0.07)	$-1.88^{+0.40}_{-0.53}$
WISP175_124	8.33 (0.05)	···	0.46 (0.05)	$-2.62^{+0.35}_{-0.07}$
WISP96_158	< 8.22	~ 8.4	0.41 (0.13)	$-2.55^{+0.28}_{-0.21}$
WISP138_160	8.29 (0.02)	···	···	···
WISP56_210	···	~ 8.4	0.61 (0.06)	$-1.78^{+0.73}_{-0.60}$
WISP206_261	< 8.09	8.37 (0.06)	0.69 (0.13)	$-2.34^{+0.56}_{-0.21}$

[a]In units of 12+log(O/H).

of the dimensionless ionization parameter U where

$$U \equiv \frac{q}{c} \tag{3.2}$$

The ionization parameter depends on the nature of the ionizing radiation source(s) as well as the density and geometric distribution of the gas in H II regions. It is useful because it can be measured easily using the ratio of fluxes from different ionization stages of the same element, for example the ratio $O32 \equiv$[O III]λ5007/[O II]λ3727.

We used the $O32$ values from the sample together with the IZI code and priors on the metallicity to derive ionization parameter estimates. The extinction-corrected values of $O32$ and inferred log U values are given in Table 3.4. The ionization parameters for our sample range from $-3.26 < \log U < -1.78$, with an average log U of -2.59. These values are signficantly elevated with respect to local samples, for which ionization parameters in the range $-4 < \log U < -3$ are typical. The ionization parameters we measure are, however, in close agreement with those measured in other high redshift samples (e.g., Hainline et al. (2009), Richard et al. (2011), Wuyts et al. (2012), Nakajima et al. (2013)).

Erb et al. (2010) found a very high ionization parameter of log $U \sim -1$ for the low mass, low metallicity, star-forming galaxy Q2343-BX418 at z=2.3. This galaxy was selected for detailed study based on its low mass and blue UV-continuum slope. While our sample includes galaxies analogous to BX418 in many respects, including stellar mass, metallicity, SFR, half-light radius, and reddening, we do not find any sources with a comparably high ionization parameter. BX418 may be somewhat exceptional in this regard.

3.4.4 Star formation rates

The star formation rates for the sample were determined using the extinction-corrected values of $F(\text{H}\alpha)$ together with the calibration of Kennicutt (1998) converted to a Chabrier IMF. In this analysis we have assumed that AGN contribution is negligible (this issue is discussed further in §6.1). The results are summarized in Table 3.3. The estimated star formation rates range from $\sim 5 - 100$ $M_\odot$ yr^{-1} with an average of 29 $M_\odot$ yr^{-1} and a median of 27 $M_\odot$ yr^{-1}. As noted previously, the sources with the highest extinction-corrected SFRs tend to be those sources with more dust extinction overall, but this could be a selection effect.

3.4.5 Line widths & dynamical mass estimates

The emission line velocity dispersions are resolved in the FIRE spectra and are summarized in Table 3.5. Figure 3.10 shows a histogram of the measured dispersions (deconvolved with the instrumental resolution), which range from 50 to 200 km s^{-1}, but show a peak around $\sim$70 km s^{-1}.

Comparable (though generally more massive) star-forming galaxies at $z \sim 2$ have been shown through integral field studies (e.g., Law et al. 2009) to have kinematics that are often dominated by random motions. For any particular galaxy it is difficult to know if the line width results from rotation-dominated galaxy dynamics, turbulent motions of the ISM, thermal motion of gas in H II regions, or some combination of these. At least two galaxies in our sample (WISP43_75 and WISP25_53) show evidence for rotational motion in the FIRE 2D spectra, but the majority show no clear spatial gradient in the 2D emission lines. One source, WISP81_83, shows double-peaked emission lines separated by 290 km s^{-1}, likely due to either a small merger in progress or an

Table 3.5. Velocity dispersions and half-light radii for the sample.

Object ID	σ([O III]) (km s^{-1})	σ(Hα) (km s^{-1})	R_e (kpc)
WISP159_134	45.7 (3.0)	64.9 (4.3)	···
WISP134_171	111.8 (5.2)	71.5 (2.1)	2.4
WISP50_65	152.4 (20.0)	145.5 (3.8)	2.7
WISP173_205	65.4 (1.3)	61.3 (1.4)	1.5
WISP9_73	85.9 (2.6)	79.0 (1.0)	1.5
WISP43_75	···	···	3.2
WISP25_53	74.5 (0.8)	75.9 (1.2)	2.2
WISP46_75	66.1 (10.4)	69.4 (3.9)	···
WISP126_90	···	78.1 (1.5)	2.4
WISP22_111	80.2 (12.5)	68.3 (1.9)	2.6
WISP22_216	40.9 (1.7)	48.2 (1.7)	2.2
WISP64_2056	52.8 (1.0)	58.5 (1.9)	···
WISP81_83	···	···	2.8
WISP138_173	62.3 (2.7)	60.5 (6.4)	2.2
WISP170_106	71.4 (4.0)	55.2 (3.2)	1.6
WISP64_210	64.8 (1.5)	74.5 (4.7)	1.6
WISP204_133	55.3 (8.4)	54.9 (11.2)	1.7
WISP27_95	128.4 (1.3)	109.6 (3.0)	2.0
WISP147_72	202.4 (1.3)	186.7 (7.2)	1.6
WISP90_58	110.4 (1.9)	111.9 (2.9)	1.6
WISP70_253	39.6 (0.7)	51.2 (3.2)	1.6
WISP175_124	71.1 (1.0)	85.1 (4.5)	2.0
WISP96_158	47.5 (1.5)	50.7 (3.2)	2.4
WISP138_160	66.0 (0.4)	56.5 (0.8)	1.6
WISP56_210	97.7 (5.7)	84.0 (23.3)	2.1
WISP206_261	46.5 (0.8)	39.4 (1.7)	1.9

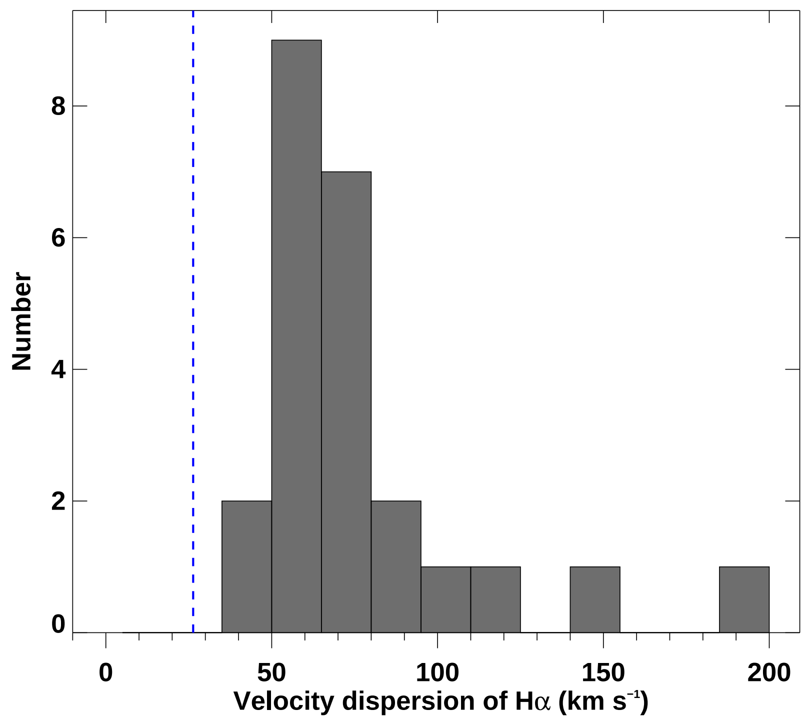

Figure 3.10 The velocity dispersions of the Hα lines. The blue dashed line shows the average resolution of FIRE (62 km s^{-1} FWHM = 26.4 km s^{-1} in sigma). The line velocity dispersions have been deconvolved with the instrumental resolution.

unresolved disk. WISP43_75 also shows what appears to be two-component emission in Hα, though less pronounced than WISP81_83.

Following the analysis of Maseda et al. (2013) and references therein, we can estimate the dynamical mass of galaxies in the sample using the emission line velocity dispersions and half-light radii from the relation

$$M_{dyn} = C\frac{r_{\rm eff}\sigma^2}{G} \tag{3.3}$$

The constant C is a geometric correction factor that can vary depending on the assumed shape and orientation of the galaxies. We adopt $C = 3$ as in Maseda et al., with a quoted uncertainty of 33%. The half-light radii are measured from the direct H-band images from WFC3, and are summarized in Table 3.5. In Figure 3.11 we plot the dynamical masses obtained in this way against the rough stellar mass estimates obtained as described in §4.2.

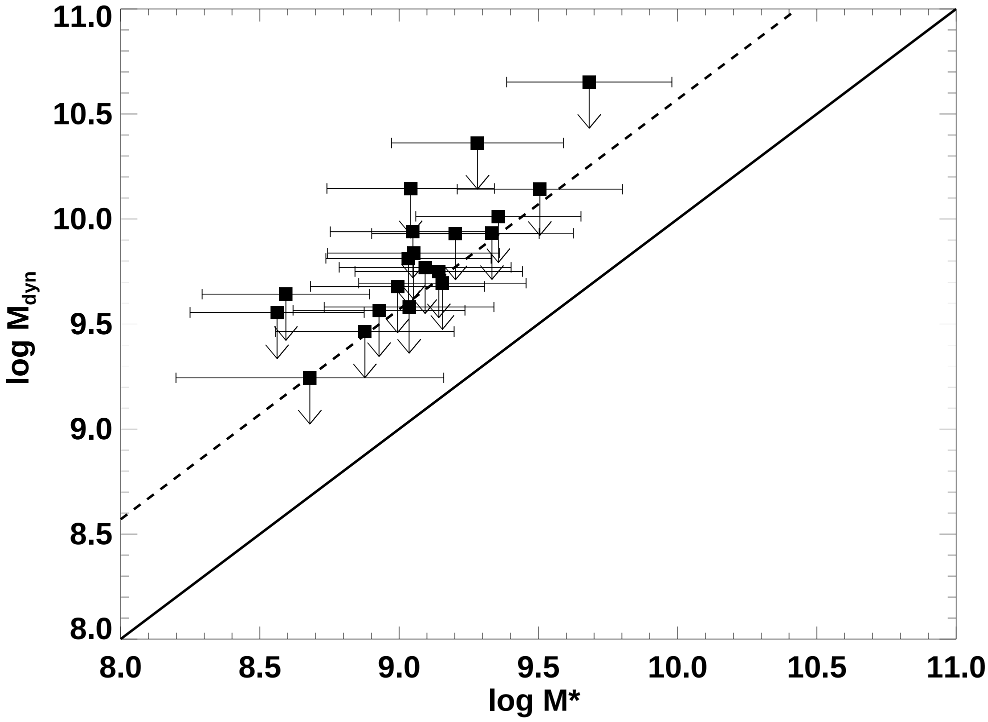

Figure 3.11 Here we show the dynamical mass estimated from Equation 3 (in units of $M_{\odot}$) against the stellar mass estimates from the WFC3 photometry. The dynamical mass estimates (plotted as upper limits) are systematically higher by ∼0.6 dex, which may reflect a low (∼ 30%) contribution of stars to the dynamical masses of the systems. However, the dynamical mass estimates are also likely to be elevated by random/turbulent motions of the gas affecting the measured line dispersions.

The dynamical mass estimates from Equation 3 are plotted as upper limits, because the line dispersions are a result of both rotational and turbulent/thermal motions of the gas and the relative contribution of these is uncertain. Our dynamical and stellar mass estimates show a strong correlation and are in relatively good agreement with the 0.57 dex offset found by Maseda et al. between the two estimates. This offset indicates that stars contribute ∼27% to the mass, assuming all of the dispersion is dynamical in origin. However, random motions of the gas may contribute substantially to the line dispersions, which would in part explain the offset between the dynamical and stellar mass estimates.

3.4.6 Morphologies

While detailed morphological modeling of the galaxies is beyond the scope of this paper, we may make some observations based on visual observation of the WFC3 imaging data. The H-band imaging (corresponding to rest-frame optical) for the galaxies in the sample reveals that a large fraction ($\gtrsim$40%) show evidence for disruption or asymmetry, probably indicative of merging or the existence of multiple star-forming clumps. Additionally, most sources are quite compact, with measured half-light radii typically $\lesssim$ 2.5 kpc.

An interesting example of a probable merger-driven starbursting galaxy is WISP96_158, which lies in one of the deepest WISP pointings. A serendipitous detection of [O III] emission in the FIRE 2D spectrum from a neighboring galaxy led to the identification of a small group of objects at the same redshift as the main emission-line galaxy. In Figure 3.12 we show the unusually deep WISP F110W exposure, in which we can clearly see the system of small galaxies surrounding WISP96_158, which itself appears clumpy and disturbed. It therefore seems likely that this starburst is triggered by the interaction/merger of small systems.

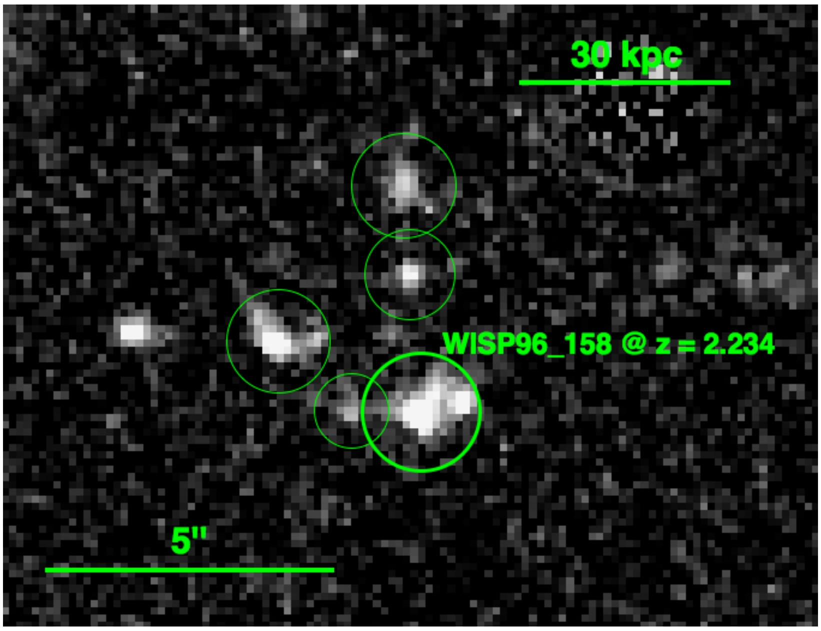

Figure 3.12 The emission-line galaxy WISP96_158 lies in one of the deepest WISP fields (28081 sec and 11430 sec exposures in the G102 and G141 grisms, respectively, and a 4295 sec direct image in the F110W filter, shown). A serendipitous detection of [O III]λ5007 in the FIRE 2D spectrum from a neighboring galaxy led to the identification of the small group of galaxies (circled) at the same redshift as WISP96_158. A significant fraction of strong emission-line galaxies at $z \sim 2$ are plausibly triggered by small gas-rich mergers in systems such as this one.

3.5 Composite optical spectrum

We constructed a composite 1D spectrum using the FIRE spectra, in order to probe the average properties of emission-line galaxies at $z \sim 2$ in greater detail. The composite contains 24 sources from FIRE, with two sources, WISP81_83 and WISP43_75, excluded due to the presence of multiple velocity components in their emission lines. To create the composite we shifted the individual 1D spectra to rest frame, interpolated to a common dispersion of 0.2 Å, and performed an inverse-variance weighted average of the flux at each wavelength after scaling the spectra to a common $F(\mathrm{H}\alpha)$. The weighting was done to minimize the contribution of OH line residuals from individual spectra. To verify that the result is not driven by a handful of individual spectra, we also performed a median combine and an unweighted average, both of which gave nearly identical results.

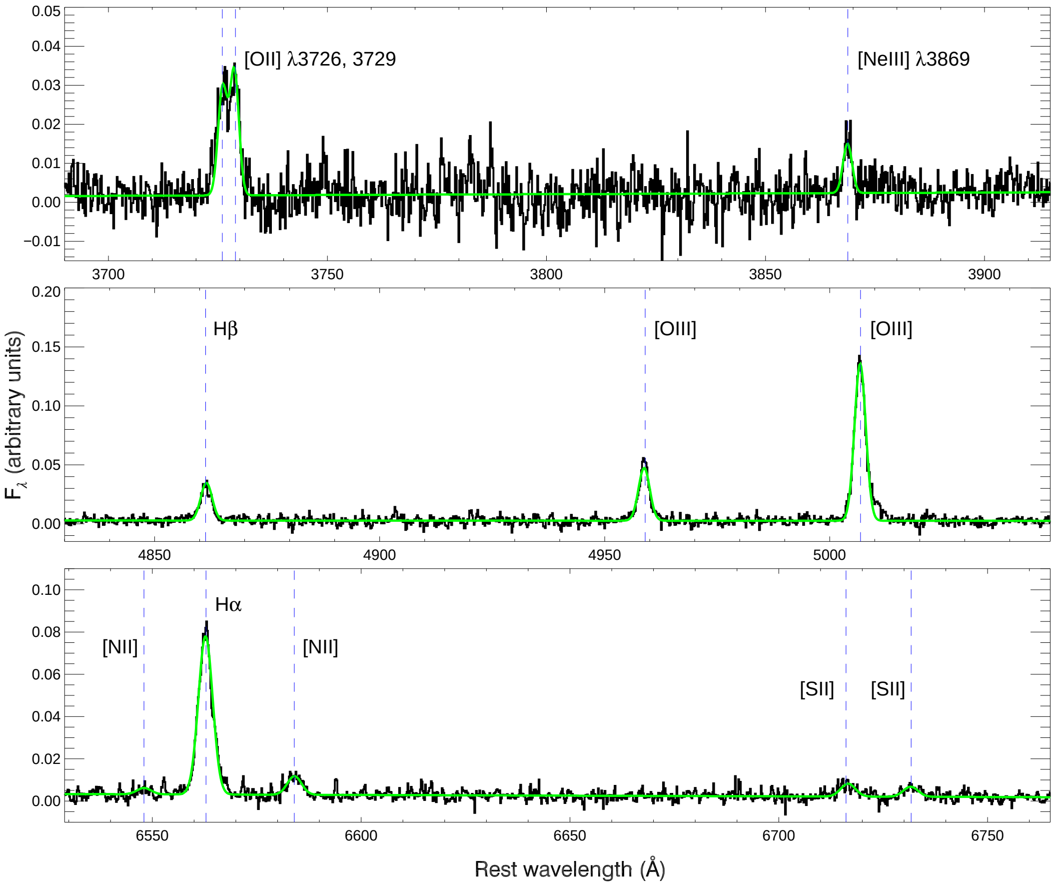

Figure 3.13 The composite FIRE spectrum of 24 emission-line galaxies from the WISP survey, with an average redshift of $\langle z \rangle = 1.85 \pm 0.39$. The fit is overlaid in green.

The composite 1D spectrum is shown in Figure 3.13. In Table 3.6 we give the emission line fluxes for the composite, normalized to $F(\mathrm{H}\beta)$=1.

Table 3.6. Line flux measurements from composite spectrum, normalized such that $F(\mathrm{H}\beta)=1$.

Line	Value
$F([\mathrm{OII}]\lambda 3726)$	0.702 (0.064)
$F([\mathrm{OII}]\lambda 3729)$	0.815 (0.057)
$F([\mathrm{NeIII}]\lambda 3869)$	0.324 (0.017)
$F([\mathrm{H}\beta])$	1.000 (0.008)
$F([\mathrm{OIII}]\lambda 5007)$	4.116 (0.007)
$F([\mathrm{H}\alpha])$	3.170 (0.013)
$F([\mathrm{NII}]\lambda 6583)$	0.372 (0.010)
$F([\mathrm{SII}]\lambda 6716)$	0.264 (0.010)
$F([\mathrm{SII}]\lambda 6731)$	0.205 (0.009)

3.5.1 Average physical properties from the composite spectrum

The physical properties of the composite are summarized in Table 3.7. The composite spectrum has a low extinction of $E(B-V) = 0.08 \pm 0.01$ as derived from its Balmer decrement of Hα/Hβ = 3.17. We computed the metallicity of the composite using the $N2$ and R_{23} (upper and lower branch) calibrations, as well as with the interpolation code IZI. The metallicity estimates are in relatively good agreement and yield a similar metallicity (∼0.50 $Z_{\odot}$) as found on average from the individual spectra. The ionization parameter for the composite is log $U \sim -2.49$, which is also consistent with the estimates from the individual FIRE spectra.

The velocity dispersion in Hα for the composite spectrum is 78 km s^{-1}. This value is in agreement with the $\langle\sigma_{mean}\rangle = 78 \pm 17$ km s^{-1} found for the similar sample analyzed by Law et al. (2009) at $z \sim 2$, which comprised 12 star-forming galaxies selected to have well-detected Hα or [O III] emission.

3.5.1.1 Limit on T_e from the composite

The ratio of [O III]λ4959, 5007 to [O III]λ4363 is a direct temperature indicator as it probes the relative abundance of electrons with the different excitation energies needed to produce these lines. [O III]λ4363 is not detected in the composite, but we are able to put a limit on its value: F([O III]λ4363) < 0.11 (2σ) on a scale in which F(Hβ)=1. This gives an upper limit of $T_e < 16,800$ K on the average gas temperature (Osterbrock & Ferland 2006).

Table 3.7. Physical parameters derived from the composite spectrum.

Parameter	Value
$\sigma_{(\mathrm{H}\alpha)}$	78 km s^{-1}
$\sigma_{([\mathrm{OIII}])}$	75 km s^{-1}
$\mathrm{H}\alpha/\mathrm{H}\beta$	3.17 (0.03)
$E(B-V)_{\mathrm{nebular}}$	0.08 (0.01)
12+log(O/H) ($N2$)	8.37 (0.01)
12+log(O/H) ($R23$, lower)	8.20 (0.01)
12+log(O/H) ($R23$, upper)	8.68 (0.01)
12+log(O/H) (IZI)	8.46 (0.08)
$O32$[a]	0.39 (0.05)
log U	$-2.49^{+0.07}_{-0.14}$

[a]Corrected for dust extinction using Balmer decrement.

3.5.1.2 Electron density from [SII] and [OII]

Electron densities can be estimated from the collisionally excited forbidden lines [S II]$\lambda6716, 6731$ and [O II]$\lambda3726, 3729$, both of which are cleanly detected in the FIRE composite spectrum. We measure [S II]$\lambda6716/\lambda6731 = 1.29 \pm 0.07$ and [O II]$\lambda3729/\lambda3726 = 1.16 \pm 0.13$. These values are both consistent with $n_{\rm e} \simeq 100 - 400$ cm^{-3}. This density range is elevated in comparison with typical H II regions in the local universe, which generally have $n_{\rm e}$ ∼50–100 cm^{-3} (e.g. Brinchmann et al. 2008b; Shirazi et al. 2013).

Shirazi et al. (2013) argued that the elevated ionization parameters observed in high redshift star-forming galaxies are a result of higher electron densities, on the order of ∼10^3 cm^{-3}. The higher average densities we find are consistent with this being a factor driving the higher ionization parameters at high redshift. However, ionization parameter scales weakly with electron density: $U \propto n_{\rm e}^{1/3}$ (Charlot & Longhetti 2001), and the ∼4× higher electron density we find with respect to local samples is, therefore, probably not the only cause of the ∼0.5-1.0 dex higher ionization parameters in the high redshift emission-line galaxies. The volume-averaged rate of production of ionizing photons in these galaxies, which have concentrated, low metallicity star formation, may be another major factor producing the high ionization parameters.

3.6 Analysis

3.6.1 BPT diagram and AGN contribution

The Baldwin, Phillips & Terlevich (BPT) diagram (Baldwin et al. 1981) uses the emission line ratios [N II]/Hα and [O III]$\lambda5007$/Hβ to separate star-forming galaxies

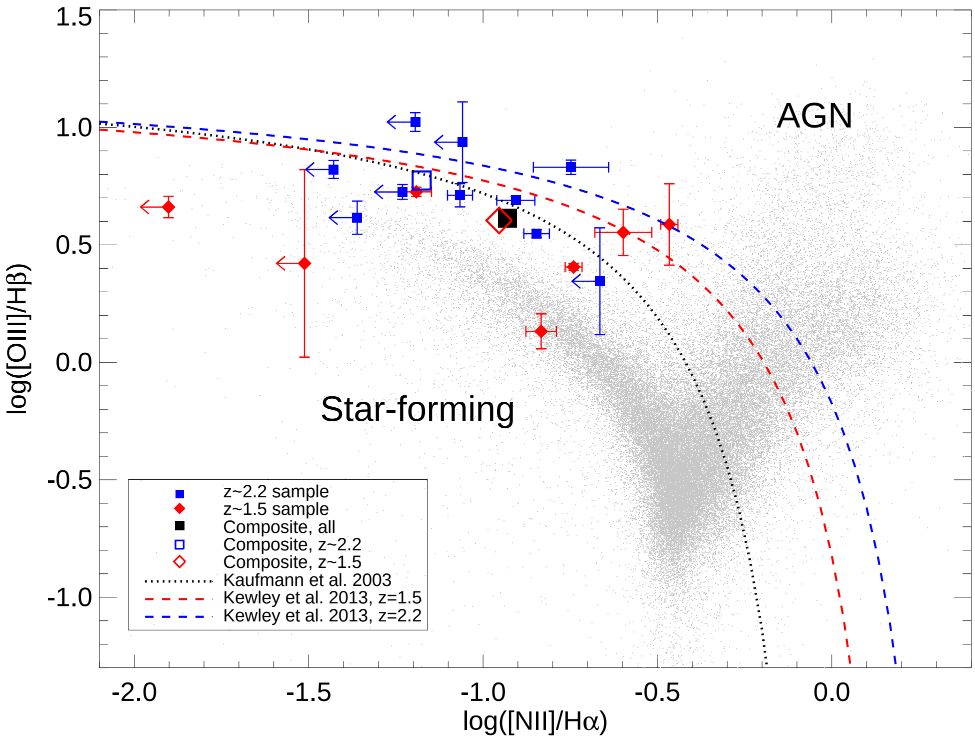

Figure 3.14 The BPT diagram for the galaxies in the sample for which we could measure the required lines. The small gray points are 60,000 sources from SDSS for comparison. Upper limits on log([N II]/Hα) at the 95% confidence level are given for those sources for which [N II]λ6583 was not detected. The black square and open symbols are the result for the composite FIRE 1D spectra (note that the error bars for these are smaller than the symbols). The [O III]/Hβ ratio for our sources is systematically higher than for star-forming galaxies in the local universe, a trend that has been noted previously. We show the empirical maximum starburst line from Kauffmann et al. (2003). Recently, Kewley et al. (2013b) proposed a redshift-dependent formulation of the maximum theoretical starburst line, shown here for $z = 1.5$ and $z = 2.2$. The majority of our points are consistent with being highly star-forming galaxies according to these demarcations.

from AGN. We were able to measure the four lines required for the BPT diagnostic for nine galaxies in our sample, and eight more for which a meaningful limit on F([N II])

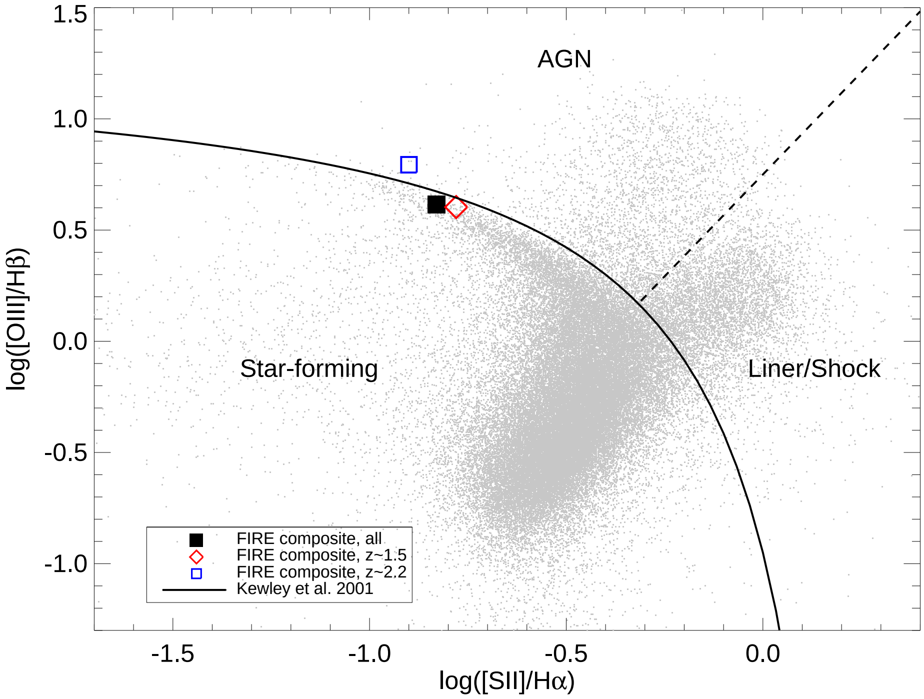

Figure 3.15 The BPT diagnostic diagram using the ratio [SII]/Hα in place of [NII]/Hα (Veilleux & Osterbrock 1987). Our composite spectrum from FIRE falls along the metal-poor tail of the local star-forming sequence from SDSS. No evidence for significant AGN or LINER/shock contribution to the emission lines is evident from this diagnostic.

could be placed. The resulting BPT plot is shown in Figure 3.14. Galaxies that are not shown had one or more of the relevant emission lines contaminated by an OH sky line.

The position occupied by the overall composite spectrum is shown as a black filled square. Additionally, we generated composite spectra at $z \sim 1.5$ and $z \sim 2.2$ using the procedure described in the previous section and measured the diagnostic ratios from them in order to search for possible evolution over this redshift interval. It should be noted that all of these composites contain additional objects that we were not able to include individually in the plot.

A clear feature of this plot is the average upward offset of the ratio [O III]/Hβ for a given [N II]/Hα of the $z \sim 2$ sample relative to local star-forming galaxies. This trend has been noted in previous studies (Shapley et al. 2005; Erb et al. 2006; Liu et al. 2008; Hainline et al. 2009; Newman et al. 2013), and has been linked to higher ionization parameters, on average, in star-forming galaxies at high redshift (e.g., Brinchmann et al. 2008b; Kewley et al. 2013b). The one galaxy in the sample that does fall on the local star-forming sequence in this diagram, WISP46_75, also has the lowest measured ionization parameter.

Recently Kewley et al. (2013b) presented a redshift-dependent parameterization of the AGN/starburst boundary line, motivated by the observational evidence for systematic offsets in the diagram for galaxies at high redshift. These lines are plotted on the left panel of Figure 3.14 for $z = 2.2$ and $z = 1.5$. It can be seen both from the individual galaxies and the composites that the sources at $z \sim 2.2$ tend to have higher [O III]/Hβ ratios in comparison with those at $z \sim 1.5$. The composite spectra are in fact consistent with being "maximal starbursts" according to the empirical demarcation Kauffmann et al. (2003), while falling well above the locus of star-forming galaxies in the local universe. The $z \sim 2.2$ composite is offset to the upper left of the $z \sim 1.5$ composite, hinting at an evolutionary trend over this redshift interval. However, this is probably (at least in part) due to a selection effect resulting from the fact that the $z \sim 2.2$ sample was selected on the basis of [O III] emission, while the $z \sim 1.5$ sample was often selected on the basis of Hα emission without regard to the strength of [O III].

We plot the position of the FIRE composite spectra on the log([O III]/Hβ) versus log([S II]/Hα) diagnostic (Veilleux & Osterbrock 1987) in Figure 3.15. The $z \sim 2.2$ composite is again offset to the upper left from the $z \sim 1.5$ composite. Notably, there is no obvious offset of the overall composite spectrum in this diagram with respect to the local star-forming sequence from SDSS.

The elevated [O III]/Hβ ratios in the traditional BPT diagram could be at least partially due to AGN activity in such galaxies (Trump et al. 2011, 2013; Kewley et al. 2013a). While a few objects in our sample fall close to the composite region of the BPT diagram, most are consistent with a purely star-forming classification. The positions of the composite spectra in the BPT diagrams, in particular, argue against signficant AGN contribution. Nevertheless, caution is required in interpreting these diagrams at high redshift. For example, Kewley et al. (2013a) showed that the effect of a low-metallicity AGN on the BPT diagram can be indistinguishable from the offset caused by more extreme star-forming conditions. However, the relatively low (~75 km s^{-1}) average velocity dispersion of the emission lines also disfavors significant AGN contribution, and we conclude that AGN activity in high-EW emission-line galaxies at $z \sim 2$ is likely to be minimal.

3.6.2 High [OIII]/Hα and [OIII]/Hβ ratios

A significant fraction of galaxies in the our sample show quite high [O III]λ5007 emission relative to the recombination lines Hα and Hβ. Both Domínguez et al. (2013) and Colbert et al. (2013) also noted the relatively large number of sources in the WISP survey with high [O III]/Hα ratios and found a negative correlation between the ratio [O III]/Hα and Hα luminosity. High [O III]/Hβ ratios were also found to be characteristic of Lyman-break selected galaxies at $z \sim 3.5$ by Holden et al. (2014).

The [O III]/(Hα,Hβ) line ratios we find for a number of galaxies in our sample are higher than the maximum values predicted by photoionization model grids for low-metallicity galaxies (e.g. Levesque et al. 2010). The $O32$ ratios for these sources indicate high ionization parameters, but not high enough to account for the [O III]/(Hα,Hβ) ratios. To investigate this further we made composite FIRE spectra of subsamples with high and low [O III]/Hα ratios, with the dividing ratio being [O III]/Hα=1.55 to give a roughly equal number of galaxies in each composite. The physical parameters derived from these composite spectra are summarized in Table 3.8. A few things emerge from these composites:

1. The cut on the ratio [O III]/Hα largely splits in a similar way as the cut on redshift, with high [O III]/Hα ratios more common among the $z \sim 2.2$ sample. As mentioned previously, this could be a selection effect given that the $z \sim 2.2$ sample was selected based on [O III] emission.

2. The [N II]/Hα ratio is lower for the composite of galaxies with high [O III]/Hα, most likely indicative of lower metallicity for those sources, although a higher ionization parameter can also lower this ratio. The correlation of [O III]/Hα and metallicity has been noted previously (Liang et al. 2006; Colbert et al. 2013), and is related to the shape of the star-forming sequence in the BPT diagram.

3. The sources with higher [O III]/Hα have significantly stronger [Ne III]/[O II] and [O III]/[O II] ratios than those with lower [O III]/Hα. Both of these ratios are sensitive to ionization parameter (Levesque & Richardson 2013), suggesting (as expected) that the higher ionization parameter is a key factor in elevating the [O III]/Hα ratio.

4. Roughly the same electron density is inferred for both composites from the density-sensitive doublets [O II]λ3726,3729 and [S II]λ6716,6731, although there is considerable uncertainty in the measurements.

Overall, what we infer from this comparison is that the sources with elevated [O III]/Hα and [O III]/Hβ ratios have higher ionization parameters, as expected, but that the difference seems more linked to their lower metallicity than a difference in

Table 3.8. Comparison of the properties of composite spectra binned by the ratio [O III]/Hα.

Parameter	[O III]/Hα > 1.55	[O III]/Hα < 1.55
12+log(O/H) ($N2$)	8.22 (0.04)	8.34 (0.03)
12+log(O/H) (Model grid)	8.30 (0.03)	8.46 (0.10)
O3O2	0.59 (0.05)	0.26 (0.09)
Ne3O2	-0.52 (0.09)	-0.74 (0.08)
log U	-2.1 (0.2)	-2.6 (0.2)
[S II]λ6716/[S II]λ6731	1.28 (0.32)	1.34 (0.18)
[O II]λ3729/[O II]λ3726	1.09 (0.33)	0.95 (0.35)

electron density. The relationship between ionization parameter and metallicity is also known to exist for local star-forming galaxies (Dopita et al. 2000; Kewley & Dopita 2002). Metallicity influences ionization parameter through its effect on stellar radiation: at low metallicity the UV flux from metal-poor stars is more intense due to decreased metal-line blanketing in stellar atmospheres. Moreover, rotational mixing in massive, rotating stars can lead to more efficient mass loss and facilitate the onset of the Wolf-Rayet phase and a corresponding hardening of the spectrum; this effect is predicted be more pronounced in low-metallicity environments (Leitherer 2008; Levesque et al. 2012; Kewley et al. 2013a). While electron density does not differentiate the two composites, both have higher electron densities than local samples.

3.6.3 What drives the BPT diagram offset?

The upward offset of many high redshift star-forming galaxies in the [O III]/Hβ versus [N II]/Hα diagram relative to the local star-forming sequence has been interpreted as resulting from more extreme star forming conditions in the early universe. Brinchmann et al. (2008b) showed that the offset from the ridgeline in the BPT diagram correlates closely with EW(Hα) in SDSS, and from this inferred that higher ionization parameter (which likely is related to EW(Hα)) is behind the effect.

The galaxies in our sample do have elevated ionization parameters relative to local samples, and show the offset in the [O III]/Hβ versus [N II]/Hα diagram seen in other high redshift star-forming galaxies. However, the composite spectrum from the FIRE sample does not show an analogous offset from the local metal-poor star-forming sequence in the [O III]/Hβ versus [S II]/Hα diagram, which is somewhat puzzling if more extreme star-forming conditions are the root of the offset in the [O III]/Hβ versus [N II]/Hα diagram. Moreover, the ionization parameters we measure for the sample, corresonding to log q values of ∼7.5-8.5, are simulated in up-to-date photoionization models (e.g., Dopita et al. 2013), and generally do not produce as large of an offset in the [O III]/Hβ versus [N II]/Hα diagram as what is observed.

Thus it is worth considering alternative explanations for the offset of high redshift star-forming galaxies from the local star-forming sequence in the [O III]/Hβ versus [N II]/Hα diagram. One possible cause of such an offset is a higher average nitrogen-to-oxygen abundance ratio (Pérez-Montero & Contini 2009). The N/O ratio for galaxies is roughly flat (though with significant scatter) at low metallicities, with a plateau value of log(N/O) ~ -1.5, and increases at higher metallicities due to the secondary production of nitrogen through the CNO cycle (Henry et al. 2000). Cases of enhanced nitrogen abundance have been found in starburst galaxies in the local universe. For example, the blue compact starburst galaxy NGC 5253 is known to have regions of 3× higher nitrogen abundance than normally found in metal-poor galaxies (Welch 1970; Walsh & Roy 1987; Kobulnicky et al. 1997), which seem to be associated with super star clusters (Westmoquette et al. 2013). Andrews & Martini (2013), using stacked spectra from SDSS, found that the log(N/O) ratio tends to be higher at a given metallicity for galaxies with higher SFRs. Additionally, Amorín et al. (2010) presented evidence that the so-called "green pea" galaxies found in SDSS (which, with strong [O III] emission lines and compact sizes, may be low-redshift analogues of the galaxies in our $z \sim 2$ sample) show systematically high log(N/O) values for their metallicities.

To investigate this possibility, we used the calibration of Thurston et al. (1996), based on the dust-corrected ratio log(N^+/O^+), to compute the value of log(N/O) for the composite FIRE spectrum. We adopted a nebular temperature of 10,000 K, yielding a value of log(N/O) $= -0.99 \pm 0.03$. For higher nebular temperatures log(N/O) increases,

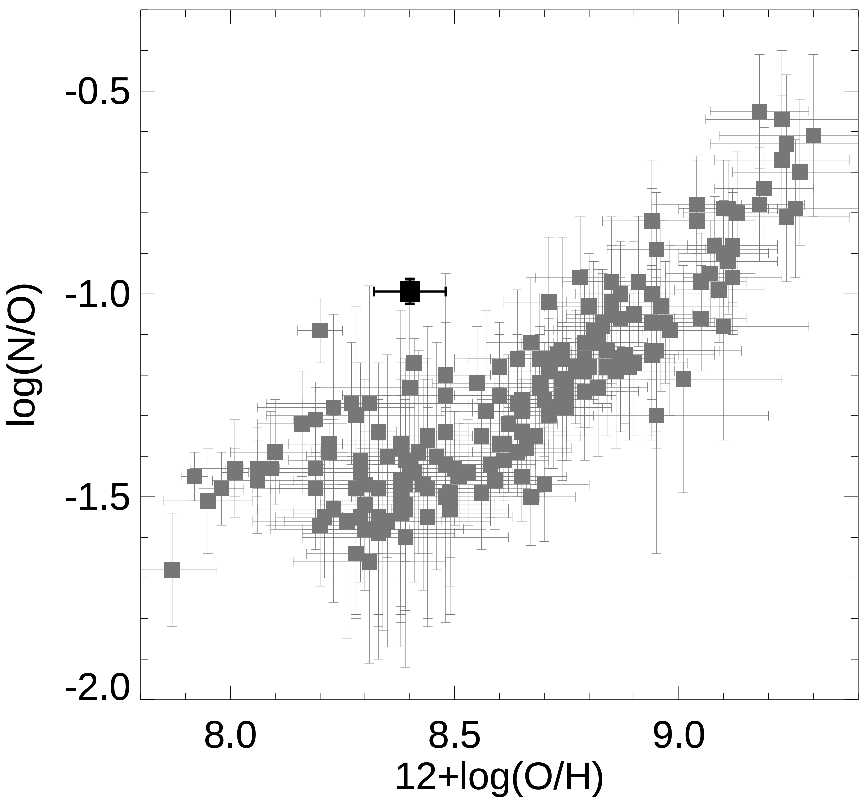

Figure 3.16 The nitrogen-to-oxygen abundance ratio vs. metallicity computed from the FIRE composite spectrum (black square) compared with values from local H II regions (van Zee et al. 1998).

so we consider this to be a relatively conservative lower limit[††]. We also computed log(N/O) using the ratio N2S2 = log([N II]/[S II]) as in Amorín et al. (2010), yielding log(N/O) $= -0.94 \pm 0.05$. Comparing these results to the measured log(N/O) values as a function of 12+log(O/H) in the literature (van Zee et al. 1998; Liang et al. 2006; van Zee & Haynes 2006; Berg et al. 2012; Andrews & Martini 2013), we find that the log(N/O) of the FIRE composite is higher by approximately 0.4 dex than the average value for galaxies at similar metallicity locally. The offset is illustrated in Figure 3.16,

[††]If, rather than use the calibration of Thurston et al. (1996), we assume that log(N/O)$\simeq$log(N^+/O^+) (as is often done in the literature), we obtain a higher value: log(N/O)$=-0.60 \pm 0.06$.

in which we show the FIRE composite spectrum in comparison with the data from local H II regions from van Zee et al. (1998).

From this analysis, it seems plausible that the offset of star-forming galaxies at high redshift in the [O III]/Hβ versus [N II]/Hα diagram is, to some extent, an offset in [N II]/Hα caused by systematically high N/O ratios. We now consider why this might be the case.

One mechanism for producing a nitrogen enhancement is through the inflow of metal-poor gas. Inflows can lower the metallicity (O/H) of a galaxy with a high N/O abundance ratio (from secondary nitrogen production) while preserving the high N/O ratio (van Zee et al. 1998; Köppen & Hensler 2005). We consider this unlikely to be the explanation of enhanced N/O in emission-line galaxies at $z \sim 2$, which are relatively young and metal-poor, and thus would not have had time to enter the secondary nitrogen production regime.

A more likely cause of the nitrogen enhancement, in our view, is a significant population of Wolf-Rayet (W-R) stars in the $z \sim 2$ emission-line galaxies. The connection between nitrogen-enriched galaxies and the influence of W-R stars has been known for some time (Pagel et al. 1986; Henry et al. 2000), and recent evidence has been found that low-redshift galaxies with W-R features in their optical spectra often display enhanced nitrogen abundances (Brinchmann et al. 2008a; López-Sánchez & Esteban 2010; Berg et al. 2011). However, the effect is generally smaller than the enhancement we find in the $z \sim 2$ sample.

Both Kobulnicky et al. (1997) and Westmoquette et al. (2013) suggested that the significantly nitrogen-enhanced regions of NGC 5253 (comparable to the enhancement we see in the $z \sim 2$ sample) result from the winds of W-R and/or related luminous blue variable (LBV) stars. Westmoquette et al. (2013) argued that the hot winds of these stars are able to mix with the cooler surrounding ISM because of the unusually high pressure environment the stars inhabit. This explanation may hold for the high redshift emission-line galaxies as well, which have higher nebular gas densities than local galaxies and probably harbor very dense star clusters to produce the observed emission lines.

A potential problem with this explanation is that the fraction of massive stars entering the W-R phase should decline with metallicity, so one would expect that the ratio of W-R to O stars would be lower in galaxies at high redshift. However, the metallicity of NGC 5253, $12 + \log(O/H) \sim 8.3$, is comparable to that of the galaxies in our emission-line sample at $z \sim 2$, and Brinchmann et al. (2008a) also find a large number of low-metallicity galaxies with W-R features. Moreover, the ratio of nitrogen- (WN) to carbon (WC)-sequence W-R stars increases strongly at lower metallicities (Crowther 2007), and WN-sequence stars would be most responsible for ejecting nitrogen into the ISM, leading to the observed enhancement.

It should be noted that evidence already exists for significant numbers of W-R stars in star-forming galaxies at high redshift. The composite rest-frame UV spectrum of $z \sim 3$ Lyman-break galaxies presented in Shapley et al. (2003) shows relatively strong and broad He II $\lambda1640$ emission, as does the rest-frame UV spectrum obtained by Erb et al. (2010) for the low-metallicity galaxy BX418 at $z = 2.3$. This feature is attributed to the fast, dense winds of W-R stars. As discussed by those authors, reproducing the He II $\lambda1640$ emission is difficult with existing stellar population synthesis models. In order to do so, very young starburst ages, a top-heavy initial mass function (IMF), or physical effects due to binary stellar evolution must be invoked. Clearly, there is still much that is not fully understood about the star formation in these environments.

3.6.4 NGC 5253 as local analogue of the high-z sample

We have assumed in the previous analysis that the local blue compact dwarf galaxy NGC 5253 is a potential analogue for the high redshift emission-line galaxies. In order to test this idea further, we used the line flux measurements from Kobulnicky et al. (1997) to see where NGC 5253 lies on the BPT diagrams with respect to our sample. The left side of Figure 3.17 illustrates that NGC 5253 (green square) falls almost directly on top of the composite spectrum from the FIRE sample, above and to the right of the locus of star-forming galaxies from SDSS. Moreover, when we place it on the [O III]/Hβ versus [S II]/Hα diagram, we find that it lies directly on the metal-poor tail from SDSS (i.e., no offset with respect to other star-forming metal poor galaxies is observed). This is also in agreement with what we find for the FIRE composite spectrum.

Given its known N/O enhancement, which has been firmly linked to the presence of W-R and/or LBV stars, the location of NGC 5253 on both BPT diagrams supports our conjecture that many high-redshift galaxies have similarly enhanced nitrogen abundances, and that W-R stars could be behind the effect. It is worth noting that NGC 5253 closely resembles the average galaxy in our sample in other respects, including its low mass, half-light radius, metallicity, and high [O III]/(Hα,Hβ) ratios. Therefore, NGC 5253 may be a good laboratory for understanding the physics driving the intense star-formation at $z \sim 2$.

3.7 Summary & discussion

We have presented rest-frame optical spectra taken with Magellan FIRE of a sample of 26 emission-line galaxies at $z \sim 1.5$ and $z \sim 2.2$ selected from the HST-WFC3 grism spectroscopy of the WISP survey. The FIRE spectra provide significant addi-

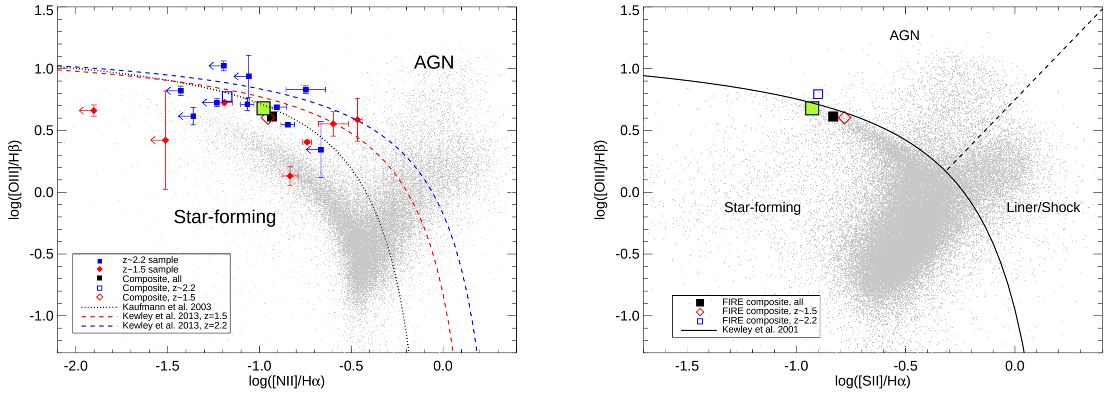

Figure 3.17 *Left:* Same as Figure 3.14, but this time with location of NGC 5253 shown (green square). The de-reddened line flux values for NGC 5253 are from Kobulnicky et al. (1997). *Right:* Same as Figure 3.15, with the position of NGC 5253 indicated. Both plots show excellent agreement between NGC 5253 and the high redshift sample, indicating that NGC 5253 may be a close analogue of high redshift galaxies in the local universe. It also supports our conjecture that the BPT offset may be due in part to elevated nitrogen abundance in star-forming galaxies at high redshift.

tional information about these galaxies, allowing us to measure metal abundances, dust reddening, kinematics, star formation rates and important diagnostic line ratios. We also created composite spectra that reveal further details about the average properties of the sample.

Direct WFC3 imaging shows the sources to be compact, with many ($\gtrsim$40%) exhibiting clumpiness or asymmetry. The galaxies are low mass ($\sim 10^{8.5}$–$10^{9.5}$ $M_{\odot}$), with a median metallicity of 0.45 $Z_{\odot}$. A clear mass-metallicity relation is found for the sample. As seen in other high-redshift samples, the ionization parameters of the galaxies in our sample are significantly higher, on average, than those found for typical star-forming galaxies in the local universe. The velocity dispersions of the emission lines for the sample range from ~50–200 km s^{-1} but usually are around 75 km s^{-1}. Assuming that the dispersions are almost entirely due to gravitational motions (which is probably not the case), this implies that stars make up roughly 30% of the dynamical mass of the galaxies.

The composite spectra we generated from the FIRE sample reveal more detail about the average properties of emission-line galaxies at $z \sim 2.2$ and $z \sim 1.5$. From the overall composite we infer an average electron density for the star-forming regions of 100-400 cm^{-3} and put a limit on the average temperature in these regions of $T_e < 16,800$ K from the non-detection of [O III]λ4363. The locations of galaxies and composites on the BPT diagnostic diagrams favor a starburst classification, and we find little evidence for substantial AGN contribution.

Our sample includes galaxies with unusually high [O III]/Hα and [O III]/Hβ line ratios that are not reproduced with existing photoionization models. Composite spectra sorted on the ratio [O III]/Hα indicate that those sources with high [O III]/Hα ratios show stronger [O III]λ5007 and [Ne III]λ3869 emission relative [O II]λ3727, indicating higher ionization parameters. The high [O III]/(Hα,Hβ) sources tend to be lower metallicity, which seems to be the main factor driving their higher ionization parameters. Reproducing the line ratios observed in such objects may require modifications to photoionization models to better account for the star-forming conditions in high redshift galaxies.

The well-known offset of high redshift star-forming galaxies from the local star-forming sequence in the [O III]/Hβ versus [N II]/Hα diagnostic diagram is observed in our sample, but we do not find a similar offset in the [O III]/Hβ versus [S II]/Hα diagram. We therefore investigated the possibility that the offset of high-redshift galaxies in the [O III]/Hβ versus [N II]/Hα diagram may result, at least in part, from elevated nitrogen abundances. The composite FIRE spectrum was used to infer the N/O abundance ratio, which we find to be ∼0.4 dex higher in comparison with local galaxies of similar metallicity. We speculate that an elevated nitrogen abundance in high redshift star-forming galaxies may be common, and could be explained by the presence of a substantial population of Wolf-Rayet stars embedded in super star clusters in such galaxies. We suggest that NGC 5253 may be a close analogue of many of the $z \sim 2$ emission-line galaxies.

Chapter 4

Distant Browns Dwarfs Discovered in the WISP Survey

4.1 Introduction

Understanding the nature and demographics of low-temperature brown dwarfs, which bridge the gap between dwarf stars and massive planets, is an important goal of modern astrophysics. Since the discovery of the first methane dwarf G1229B in 1995 (Nakajima et al. 1995; Oppenheimer et al. 1995), the number of known ultracool dwarfs of type T and now Y (Cushing et al. 2011) has continued to grow, primarily due to deep near-infrared surveys such as 2MASS (Kirkpatrick et al. 1999; Burgasser et al. 2002), SDSS (Strauss et al. 1999; Chiu et al. 2006), UKIDSS (Lodieu et al. 2007; Chiu et al. 2008; Burningham et al. 2010), CFBDS (Delorme et al. 2008) and WISE (Wright et al. 2010; Kirkpatrick et al. 2011). Additional dwarfs have been identified in proper motion surveys (e.g. Kirkpatrick et al. 2010; Scholz et al. 2011 and references therein). These surveys have been effective at finding brown dwarfs in the solar neighborhood; however, due to their faintness (a T8 dwarf has $M_{AB} \sim 17$ in H band), probing the larger-scale galactic distribution of ultracool dwarfs has not been possible.

Deep surveys in the near-infrared using the Wide Field Camera 3 (WFC3) on the HST enable the discovery of cold dwarfs at much larger distances. WFC3 parallel imaging surveys have identified cold dwarfs based on broad-band colors (e.g. Ryan et al. 2011), but the lack of spectroscopy means that the spectral types are uncertain. WFC3 near-infrared slitless grism spectroscopy, in contrast, permits unambiguous identification and classification of T dwarfs, whose spectra show pronounced atmospheric CH_4 and H_2O absorption bands in the near-infrared (Geballe et al. 2002; Burgasser et al. 2002). Moreover, the WFC3 spectra reach depths that are unachievable with ground-based surveys.

Here we present three of the most distant cold brown dwarfs known, discovered in the WFC3 Infrared Spectroscopic Parallels (WISP) Survey. These discoveries illustrate that, by enabling spectroscopic identification of ultracool dwarfs at large distances, HST-WFC3 grism spectroscopy can begin to probe the galactic spatial distribution of the ultracool dwarf population and search for substellar members of the halo population (Burgasser et al. 2003).

4.2 WFC3 Data

The brown dwarf discoveries presented here were found using the WFC3 grism spectroscopy of the WISP survey, which was described in some depth in the previous chapter. Please refer to the description in 3.2.1 for further details.

4.3 Brown Dwarfs in WISP

4.3.1 Identification of Ultracool Dwarfs

Brown dwarfs of type $\gtrsim$T2 are easily recognizable in H-band spectroscopy due to the presence of two prominent, broad pseudo-emission features at roughly 1.26 and 1.58 μm interspersed with deep absorption bands of water and methane in their atmospheres. The 155 G141 grism exposures (each $123'' \times 136''$) currently obtained by the ongoing WISP survey were systematically scanned by at least two observers to search for these objects, resulting in the identification of the three sources shown in Figure 4.1. Their properties are summarized in Table 1.

4.3.2 Spectral Classification

We determined the spectral types of the objects by comparing the WFC3 spectra to 69 T dwarf spectra from the SpeX Prism Spectral Libraries (Burgasser et al. 2006) and two additional Y dwarf spectra from Cushing et al. (2011). The WISP spectra and brown dwarf template spectra were compared using a χ^2 statistic. The classifications and associated uncertainties were then found by computing the weighted mean and deviation from the mean with a weighting factor of $e^{(\min(\chi^2)-\chi^2)^2}$. A cutoff weight of >0.1 was used so that the results are not skewed by a large number of poor fits to early-type T dwarfs (a sampling problem that arises because the template sample contains disproportionately more early-type T dwarfs).

WISP 1232-0033 and WISP 0307-7243 are found to be type T7±0.6 and T4.5±0.4, respectively. WISP 1305-2538 is found to be of type T9.5+, and is probably a Y dwarf. The spectrum of the Y0 dwarf WISE 1405+5534 is shown overlaid in Figure 4.1, in addition to the T9 dwarf UGPS 0722-0540. While neither template is perfect, the Y0 spectrum is a better fit.

4.3.3 Distance Determination

With accurate spectral types derived from the WFC3 spectra, the distances to the dwarfs can be found by comparing their measured broad-band magnitudes with those of nearby T dwarfs with known parallaxes. For this comparison, we converted the WFC3 F140W/F160W photometry for the WISP dwarfs into MKO J or H band with color corrections computed using the best-fitting T dwarf template spectra, applying the same weightings as for the spectral type determination. Given the inferred MKO J/H magnitudes, the distances were found using the absolute magnitude/spectral type relations of Dupuy & Liu (2012).

WISP 1232-0033 (T7) is found to be at 270±60 pc and WISP 0307-7243 (T4.5) at 400±60 pc. These are the most distant T dwarfs currently known, and have vertical scale heights of approximately 240 and 260 pc, respectively. WISP 1305-2538 is more difficult, as only one Y dwarf has reported a preliminary (and highly uncertain) parallax (WISE J154151.66−225025.2, $\pi = 0\farcs35 \pm 0\farcs11$; Kirkpatrick et al. 2011) and the classification scheme for these objects remains in progress (Cushing et al. 2011). We used the known parallaxes of the T9 UGPS 0722-0540 ($0\farcs246 \pm 0\farcs0033$; Lucas et al. 2010) and the T9.5 CFBDSIR J145829+101343B ($0\farcs340 \pm 0\farcs0026$; Liu et al. 2011) to infer a distance of 40–60 pc for this source, albeit with considerable uncertainty because of the classification.

Table 4.1. Cold Brown Dwarfs Discovered in the WISP Survey

Name	RA (J2000) (h m s)	DEC (J2000) (° ′ ″)	WFC3 magnitude (AB)	Spectral Type	Distance (pc)	Galactic Latitude (deg)
WISP 1305-2538	13 05 25.51	-25 38 28.8	23.01±0.04[b]	T9.5+	∼40-60[a]	+37.1
WISP 1232-0033	12 32 42.42	-00 33 06.7	23.34±0.05[b]	T7±0.6	270±60	+63.1
WISP 0307-7243	03 07 41.12	-72 43 57.5	22.67±0.02[c]	T4.5±0.4	400 ± 60	-40.9

[a]The interval arises from classification uncertainty and the current lack of quality parallaxes for Y dwarfs.

[b]F140W

[c]F160W

4.3.4 Space Density

The dwarfs discovered in the WISP survey provide the first opportunity to examine the mass function and spatial distribution of these late-type dwarfs in a deep field (see Pirzkal et al. 2009 for an equivalent study of late M and L dwarfs). To assess what constraints our small sample makes on these statistics, we computed the expected suface densities of T dwarfs as a function of spectral type in the WISP survey fields as follows.

1. Volume densities for the cold dwarf subtypes are computed using the methods outlined in Burgasser (2004, 2007). We assume a power-law stellar mass function $dN/dM \sim M^{-\alpha}$ with α varying from -1 to 1, normalized to agree with measured field values in the 0.09-0.10 $M_{\odot}$ range (0.0055 pc^{-3}; Reid et al. 1999; Chabrier 2001). We then assumed an age distribution consistent with a constant star formation rate over 10 Gyr, and computed the luminosity distribution for the dwarfs using the evolutionary models of Burrows et al. (1997). Finally, we use empirical bolometric correction/spectral type (Liu et al. 2010) and absolute

magnitude/spectral type (Dupuy & Liu 2012) relations to convert the luminosity function to a spectral type surface density distribution.

2. The expected surface density of dwarfs per WISP $123'' \times 136''$ pointing is then found by computing the limiting magnitude, and thus the maximum distance, for which each subtype would be spectroscopically detected* in a given field. The online WFC3 exposure time calculator is used for this analysis. Corrections to the derived limiting magnitudes are applied to account for Malmquist bias. We assumed as a first order approximation that 10% of each pointing is lost due to overlap, edge effects, etc. as estimated from the galaxy extractions.

3. The effective volumes for each field/subtype are found and multiplied by the space densities per subtype. The results for all the WISP fields are added, yielding a surface density for each subtype for the entire survey (Figure 2).

The expected surface density of each spectral type across the entire WISP survey is summarized in Figure 2 for different assumed power-law slopes in the low-mass stellar mass function. The number of dwarfs found is roughly consistent with expectations; in particular, the fact that we find no early type (<T4) dwarfs, despite their higher intrinsic luminosities, is consistent with their rarity (Burgasser 2007). The fact that we identified three T dwarfs is consistent with other field mass function estimates based on wide, shallow surveys of T dwarfs (e.g. Metchev et al. 2008; Burningham et al. 2010). However, finding a T9.5/Y0 dwarf is somewhat surprising due to their faintness. Possible explanations for this include (1) a flatter absolute magnitude/spectral type relation

*We require S/N=10 in this analysis, an approximation based on simple tests with the WFC3 spectra. However, changing the S/N requirement can significantly influence the expected surface density of dwarfs.

than preliminary estimates indicate (Cushing et al. 2011; Kirkpatrick et al. 2011), (2) a sudden upturn in the space density of very late-type dwarfs, possibly associated with a nearby free-floating planetary population (Sumi et al. 2011) or a larger proportion of old halo brown dwarfs at higher scale heights (for this simulation, a 1:400 halo fraction was assumed based on Digby et al. 2003), (3) a fortuitous discovery, or (4) some combination of the above. We note that WISP 1305-2538 is $4'.2$ from the very low-mass triple Kelu 1ABC at 20.1±1.0 pc (Liu & Leggett 2005). With a 5000 AU projected separation, this matching is unlikely, but second-epoch imaging would allow us to affirm or refute the existence of a widely-separated, very low-mass quadruple. Additionally, follow-up proper motion measurements of all three new dwarfs would help establish whether they are galactic halo members.

4.3.5 Summary

We have presented three distant T/Y dwarfs spectroscopically confirmed by the WISP Survey. These discoveries show the power of HST-WFC3 slitless grism spectroscopy to simultaneously find these objects at much larger distances than has been possible with ground-based surveys and yield accurate spectral types, making surveys such as WISP powerful new probes of the population of cold brown dwarfs in the galaxy.

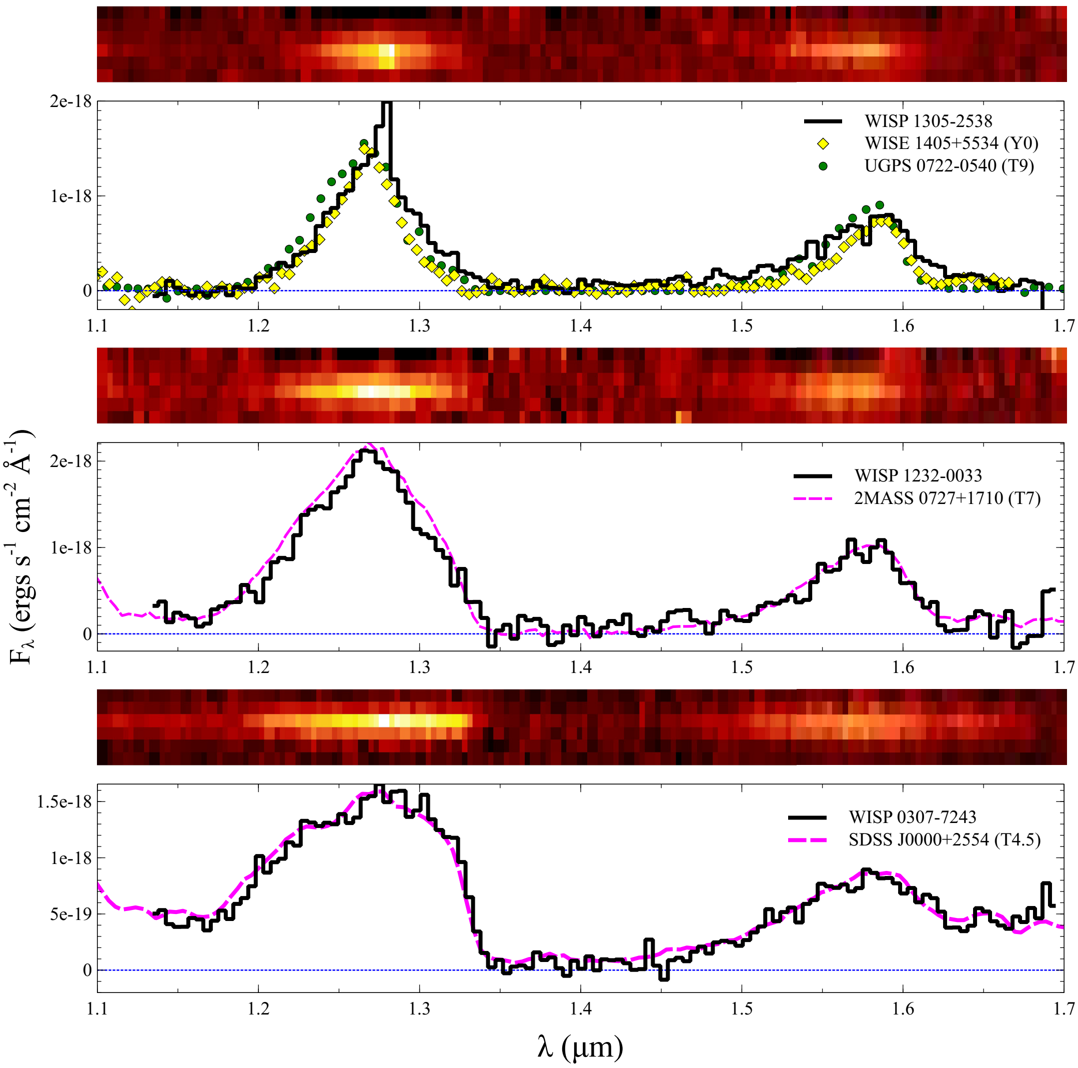

Figure 4.1 HST-WFC3 G141 1D/2D spectra of the three cold brown dwarfs found in the WISP survey, with best-fit template spectra overlaid. Prominent pseudo-emission features at roughly 1.26 and 1.58 μm are characteristic of T dwarfs and make them relatively easy to identify in the 2D grism images. While WISP 1232-0033 and WISP 0307-7243 (middle, bottom) are in nearly perfect agreement with the best-fit templates, WISP 1305-2538 (top) is not perfectly fit by either a T9 or Y0 template, although Y0 fits better. The template spectra are from the SpeX prism library (Burgasser et al. (2010) and references therein).

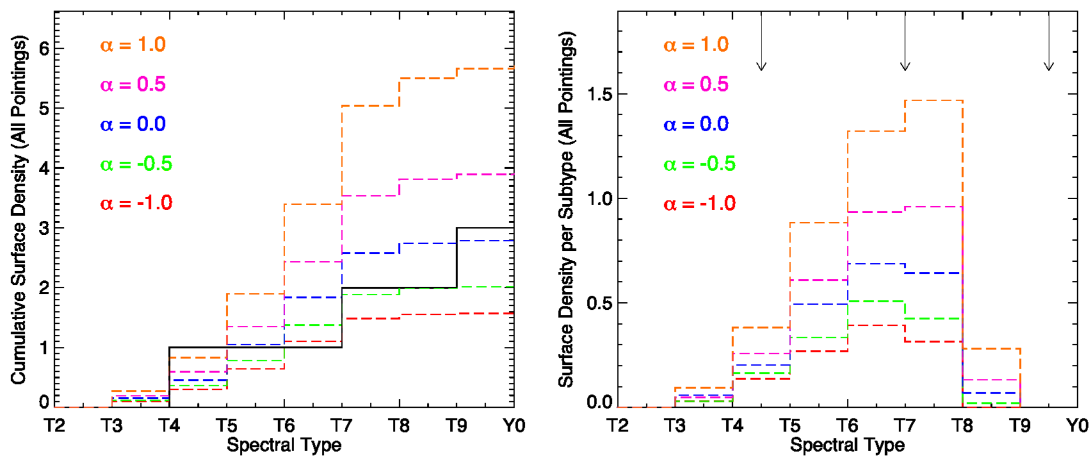

Figure 4.2 **Left:** Expected cumulative surface density of late-type dwarfs across all WISP fields for different values of α in the power-law stellar mass function $dN/dM \sim M^{-\alpha}$, from the simulations described in §6. The total number found (three, black line) is generally consistent with α=0.0–0.5. **Right:** The expected surface density of each spectral type across the entire WISP survey. The spectral types of the three dwarfs found are indicated with downward arrows. The discovery of a T9.5/Y0 dwarf is somewhat surprising; see §6 for a discussion of possible explanations.

Chapter 5

Conclusion

I have presented results from three different research projects carried out during my graduate work, ranging from the luminosity function of high redshift quasars and the physical properties of high redshift star-forming galaxies to brown dwarfs in our own galaxy. Despite the obvious differences, these topics are not as unrelated as they might seem. Evidence now suggests that supermassive black holes are important in regulating the growth of their host galaxies, making the evolution of the quasar luminosity function relevant to our understanding of early galaxy evolution. Moreover, both supermassive black hole and star formation depend on the ability of massive gas clouds to collapse under gravitation, the same physics that ultimately governs the formation of brown dwarfs. The number and distribution of brown dwarfs in our galaxy provide valuable clues regarding the low-mass end of the initial mass function of star formation. Brown dwarfs also represent "fossil records" of the chemical enrichment history of the galaxy, and thus may yield additional information regarding the star formation in the high-redshift universe.

In the following I give a concise summary of each of the research projects and the main results obtained, as well as limitations and possibilities for future work.

5.1 Summary of main results

In Chapter 2, we investigated the space density of faint optical quasars at $3 \lesssim z \lesssim 5$ using deep photometric and spectroscopic data from the COSMOS survey. Using the low-resolution spectrum afforded by the COSMOS intermediate and broad-band photometry, we developed a method to select and classify high-redshift quasars with high completeness and low contamination, using spectroscopically confirmed sources to check our results. We measured the faint-end slope of the quasar luminosity function at $z \sim 3$ and $z \sim 4$, finding $\beta \sim -1.7$ at both redshifts. This value is similar to those found at lower redshifts, indicating little or no evolution in the faint-end slope with redshift. We found that faint quasars, like bright quasars and X-ray sources, show a steep decline in overall space density with increasing redshift for $z \gtrsim 3$, after a peak around $z \sim 2-3$. This trend is analogous to the global star formation rate density, suggesting a link between the two processes. Based on a comparison of the UV and X-ray luminosity functions, we argue that the fraction of obscured quasars may increase to ~75% at $z \sim 4$. We used our results to demonstrate that quasars are not likely to contribute significantly to the ionizing radiation budget during the cosmic reionization of hydrogen at $z \sim 6-10$.

In Chapter 3, we presented results from a campaign of ground-based spectroscopy with the Magellan Baade telescope, aimed at investigating the physical properties of emission-line galaxies at $z \sim 2$. The sample was selected on the basis of clearly detected rest-frame optical emission lines from the WFC3 grism spectroscopy obtained by the WISP survey team. By measuring all of the important rest-frame optical emission lines for a large sample of high-redshift star-forming galaxies, we were able to derive detailed physical properties of such objects both individually and in a statistical sense. We find that the typical emission-line galaxy at $z \sim 2$ has low metallicity ($\lesssim 0.1 - 0.6$ $Z_\odot$), little dust reddening ($E(B-V) \sim 0.2$), low mass ($\sim 10^{8.5}$–$10^{9.5}$ $M_\odot$), rapid ongoing star formation (~ 30 $M_\odot$ yr^{-1}), and often shows signs of interaction. A strong positive correlation between metallicity and stellar mass is observed in the sample. Important differences in comparison with local star-forming galaxies emerge from our results. We find that the typical high redshift star-forming galaxy has a much higher ($\sim 3 - 10\times$) ionization parameter than local star-forming galaxies, which has been observed in prior studies of $z \gtrsim 1$ galaxies. As has also been noted previously, the high redshift galaxies fall well off of the star-forming locus in the conventional BPT diagram occupied by star-forming galaxies in the local universe. We present evidence that this effect is due, at least in part, to a nitrogen over-abundance in many high-redshift galaxies, which we interpret as being caused by the ejecta of Wolf-Rayet stars in such galaxies. With extremely hot surface temperatures, Wolf-Rayet stars could also naturally account for the elevated ionization parameters that seem to be ubiquitous in high redshift galaxies. It remains to be determined why Wolf-Rayet stars are as prevalent at high redshift as our results seem to suggest.

The final project I presented in this thesis pertained to the discovery of distant brown dwarfs in the WISP survey data. After the initial serendipitous discovery of a late-type T dwarf, we undertook a systematic search for such objects in the WISP fields. The selection function was quantified and the results compared with models of the expected population of brown dwarfs in the solar neighborhood. Our results favor a value of $\alpha = 0.0 - 0.5$ in the power-law mass function $dN/dM \sim M^{-\alpha}$ for low mass objects, although our discovery of a T9/Y0 dwarf is somewhat unexpected due to their intrinsic faintness. Follow-up observations on these objects could be used to determine proper motions, which would help to determine whether these objects are kinematically associated with the galactic halo.

5.2 Directions for future research

With regard to both the quasar luminosity function at high redshift and the distribution of brown dwarfs in our galaxy, it remains for future deep, wide surveys to put the results presented here on a more firm statistical footing. An open question to be explored is how supermassive black holes were able to form and grow as rapidly as observed, considering that black holes of mass $\sim 2\times10^9$ $M_\odot$ are known to exist as early as 800 million years after the big bang (Mortlock et al. 2011). The seeds of such black holes are also a matter of speculation at present; future studies pushing the frontiers further back in time may be able to address this question. Because brown dwarfs represent the most abundant interlopers in searches for high-redshift quasars, constraining their number density and distribution will be very important for these future studies. In addition, a detailed knowledge of the distribution and kinematics of ultracool dwarfs as a function of spectral type should prove invaluable as a probe of the early formation of our galaxy.

Perhaps the most interesting result to emerge from the spectroscopic campaign presented in Chapter 3 is that elevated nitrogen abundance may be responsible for the well-known offset of high-redshift galaxies in the conventional BPT diagram. Significant effort has recently been expended in trying to understand this shift (e.g., Kewley et al. 2013a; Trump et al. 2013), but the solution we propose has not been given significant consideration. The physical picture that emerges from this interpretation is one in which both the nitrogen enhancement and the higher ionization parameters seen in high redshift star-forming galaxies are driven by a population of Wolf-Rayet stars, which rapidly expel enriched material into the ISM through hot, radiation-driven winds.

One goal would be to verify the nitrogen enhancement result itself with independent data; this will likely happen in the near future with other large programs of near-infrared spectroscopy. Photoionization modeling can be used to simulate the likely environments in the star-forming regions of high redshift galaxies, in order to determine whether W-R star activity is consistent with all of the observed spectral properties. Modeling should also be used to test whether current calibrations for star formation rate and metallicity based on local H II regions are valid in the more extreme environments at high redshift, which seems unlikely.

Finally, more global implications can be investigated. For example, how many W-R stars are required to match the observations, and what does this imply regarding the initial mass function and/or the duration of the Wolf-Rayet phase for massive stars at high redshift? Are W-R stars important in terms of feedback and the ejection of metals into the circum-galactic medium? And what are the global physical properties of high redshift star-forming galaxies that differentiate them from the majority of star-forming galaxies in the local universe? A combination of theoretical work and further observations, particularly with the next generation of very large telescopes, will likely be needed to resolve these questions.

Bibliography

Abazajian, K., Adelman-McCarthy, J. K., Agüeros, M. A., et al. 2004, AJ, 128, 502

Abazajian, K. N., Adelman-McCarthy, J. K., Agüeros, M. A., et al. 2009, ApJS, 182, 543

Allende Prieto, C., Lambert, D. L., & Asplund, M. 2001, ApJ, 556, L63

Amorín, R. O., Pérez-Montero, E., & Vílchez, J. M. 2010, ApJ, 715, L128

Andrews, B. H., & Martini, P. 2013, ApJ, 765, 140

Arnouts, S., & Ilbert, O. 2011, in Astrophysics Source Code Library, record ascl:1108.009, 8009

Asplund, M., Grevesse, N., Sauval, A. J., & Scott, P. 2009, ARA&A, 47, 481

Atek, H., Malkan, M., McCarthy, P., et al. 2010, ApJ, 723, 104

Atek, H., Siana, B., Scarlata, C., et al. 2011, ApJ, 743, 121

Baldwin, J. A., Phillips, M. M., & Terlevich, R. 1981, PASP, 93, 5

Barkana, R., & Loeb, A. 2001, Phys. Rep., 349, 125

Barman, T. S., Hauschildt, P. H., & Allard, F. 2005, ApJ, 632, 1132

Beckwith, S. V. W., Stiavelli, M., Koekemoer, A. M., et al. 2006, AJ, 132, 1729

Bell, E. F., Wolf, C., Meisenheimer, K., et al. 2004, ApJ, 608, 752

Belli, S., Jones, T., Ellis, R. S., & Richard, J. 2013, ArXiv e-prints

Benson, A. J., Bower, R. G., Frenk, C. S., et al. 2003, ApJ, 599, 38

Berg, D. A., Skillman, E. D., & Marble, A. R. 2011, ApJ, 738, 2

Berg, D. A., Skillman, E. D., Marble, A. R., et al. 2012, ApJ, 754, 98

Bochanski, J. J., Burgasser, A. J., Simcoe, R. A., & West, A. A. 2011, AJ, 142, 169

Bolton, J. S., Haehnelt, M. G., Viel, M., & Carswell, R. F. 2006, MNRAS, 366, 1378

Bongiorno, A., Zamorani, G., Gavignaud, I., et al. 2007, A&A, 472, 443

Boulade, O., Charlot, X., Abbon, P., et al. 2003, in Society of Photo-Optical Instrumentation Engineers (SPIE) Conference Series, Vol. 4841, Society of Photo-Optical Instrumentation Engineers (SPIE) Conference Series, ed. M. Iye & A. F. M. Moorwood, 72–81

Bouwens, R. J., Illingworth, G. D., Franx, M., & Ford, H. 2007, ApJ, 670, 928

Bower, R. G., Benson, A. J., Malbon, R., et al. 2006, MNRAS, 370, 645

Boyle, B. J., Shanks, T., & Peterson, B. A. 1988, MNRAS, 235, 935

Brammer, G. B., Sanchez-Janssen, R., Labbe, I., et al. 2012, ArXiv e-prints

Brinchmann, J., Kunth, D., & Durret, F. 2008a, A&A, 485, 657

Brinchmann, J., Pettini, M., & Charlot, S. 2008b, MNRAS, 385, 769

Brusa, M., Comastri, A., Gilli, R., et al. 2009, ApJ, 693, 8

Brusa, M., Civano, F., Comastri, A., et al. 2010, ApJ, 716, 348

Bruzual, G., & Charlot, S. 2003, MNRAS, 344, 1000

Budavári, T., Csabai, I., Szalay, A. S., et al. 2001, AJ, 122, 1163

Burgasser, A. J. 2004, ApJS, 155, 191

—. 2007, ApJ, 659, 655

Burgasser, A. J. 2008, in Astronomical Society of the Pacific Conference Series, Vol. 384, 14th Cambridge Workshop on Cool Stars, Stellar Systems, and the Sun, ed. G. van Belle, 126

Burgasser, A. J., Cruz, K. L., Cushing, M., et al. 2010, ApJ, 710, 1142

Burgasser, A. J., Geballe, T. R., Leggett, S. K., Kirkpatrick, J. D., & Golimowski, D. A. 2006, ApJ, 637, 1067

Burgasser, A. J., Gelino, C. R., Cushing, M. C., & Kirkpatrick, J. D. 2012, ApJ, 745, 26

Burgasser, A. J., Kirkpatrick, J. D., Brown, M. E., et al. 2002, ApJ, 564, 421

Burgasser, A. J., Kirkpatrick, J. D., Burrows, A., et al. 2003, ApJ, 592, 1186

Burningham, B., Pinfield, D. J., Lucas, P. W., et al. 2010, MNRAS, 406, 1885

Burrows, A., Marley, M., Hubbard, W. B., et al. 1997, ApJ, 491, 856

Caballero, J. A., Burgasser, A. J., & Klement, R. 2008, A&A, 488, 181

Calzetti, D., Armus, L., Bohlin, R. C., et al. 2000, ApJ, 533, 682

Capak, P., Aussel, H., Ajiki, M., et al. 2007, ApJS, 172, 99

Cardamone, C., Schawinski, K., Sarzi, M., et al. 2009, MNRAS, 399, 1191

Cardelli, J. A., Clayton, G. C., & Mathis, J. S. 1989, ApJ, 345, 245

Chabrier, G. 2001, ApJ, 554, 1274

Charlot, S., & Longhetti, M. 2001, MNRAS, 323, 887

Chiu, K., Fan, X., Leggett, S. K., et al. 2006, AJ, 131, 2722

Chiu, K., Liu, M. C., Jiang, L., et al. 2008, MNRAS, 385, L53

Civano, F., Brusa, M., Comastri, A., et al. 2011, ArXiv e-prints

Civano, F., Elvis, M., Brusa, M., et al. 2012, ApJS, 201, 30

Colbert, J. W., Teplitz, H., Atek, H., et al. 2013, ArXiv e-prints

Conselice, C. J., Bershady, M. A., Dickinson, M., & Papovich, C. 2003, AJ, 126, 1183

Cowie, L. L., Barger, A. J., & Hu, E. M. 2011, ApJ, 738, 136

Cowie, L. L., Barger, A. J., & Trouille, L. 2009, ApJ, 692, 1476

Croom, S. M., Smith, R. J., Boyle, B. J., et al. 2004, MNRAS, 349, 1397

Croom, S. M., Boyle, B. J., Shanks, T., et al. 2005, MNRAS, 356, 415

Croom, S. M., Richards, G. T., Shanks, T., et al. 2009, MNRAS, 399, 1755

Crowther, P. A. 2007, ARA&A, 45, 177

Cullen, F., Cirasuolo, M., McLure, R. J., & Dunlop, J. S. 2013, ArXiv e-prints

Cushing, M. C., Kirkpatrick, J. D., Gelino, C. R., et al. 2011, ApJ, 743, 50

Daddi, E., Cimatti, A., Renzini, A., et al. 2004, ApJ, 617, 746

Daddi, E., Renzini, A., Pirzkal, N., et al. 2005, ApJ, 626, 680

Daddi, E., Dickinson, M., Morrison, G., et al. 2007, ApJ, 670, 156

Delorme, P., Willott, C. J., Forveille, T., et al. 2008, A&A, 484, 469

Digby, A. P., Hambly, N. C., Cooke, J. A., Reid, I. N., & Cannon, R. D. 2003, MNRAS, 344, 583

Domínguez, A., Siana, B., Henry, A. L., et al. 2013, ApJ, 763, 145

Dopita, M. A., Kewley, L. J., Heisler, C. A., & Sutherland, R. S. 2000, ApJ, 542, 224

Dopita, M. A., Sutherland, R. S., Nicholls, D. C., Kewley, L. J., & Vogt, F. P. A. 2013, ApJS, 208, 10

Dressler, A., Hare, T., Bigelow, B. C., & Osip, D. J. 2006, in Society of Photo-Optical Instrumentation Engineers (SPIE) Conference Series, Vol. 6269, Society of Photo-Optical Instrumentation Engineers (SPIE) Conference Series

Dupuy, T. J., & Liu, M. C. 2012, ArXiv e-prints

Elvis, M., Civano, F., Vignali, C., et al. 2009, ApJS, 184, 158

Erb, D. K., Pettini, M., Shapley, A. E., et al. 2010, ApJ, 719, 1168

Erb, D. K., Shapley, A. E., Pettini, M., et al. 2006, ApJ, 644, 813

Faber, S. M., Phillips, A. C., Kibrick, R. I., et al. 2003, in Society of Photo-Optical Instrumentation Engineers (SPIE) Conference Series, Vol. 4841, Society of Photo-Optical Instrumentation Engineers (SPIE) Conference Series, ed. M. Iye & A. F. M. Moorwood, 1657–1669

Fan, X. 1999, AJ, 117, 2528

Fan, X., Narayanan, V. K., Lupton, R. H., et al. 2001, AJ, 122, 2833

Fan, X., Strauss, M. A., Becker, R. H., et al. 2006, AJ, 132, 117

Ferrarese, L., & Merritt, D. 2000, ApJ, 539, L9

Fioc, M., & Rocca-Volmerange, B. 1997, A&A, 326, 950

Förster Schreiber, N. M., Genzel, R., Lutz, D., Kunze, D., & Sternberg, A. 2001, ApJ, 552, 544

Förster Schreiber, N. M., Genzel, R., Lehnert, M. D., et al. 2006, ApJ, 645, 1062

Franx, M., Labbé, I., Rudnick, G., et al. 2003, ApJ, 587, L79

Gallagher, S. C., Hines, D. C., Blaylock, M., et al. 2007, ApJ, 665, 157

Geballe, T. R., Knapp, G. R., Leggett, S. K., et al. 2002, ApJ, 564, 466

Gebhardt, K., Bender, R., Bower, G., et al. 2000, ApJ, 539, L13

Genzel, R., Burkert, A., Bouché, N., et al. 2008, ApJ, 687, 59

Giavalisco, M., Ferguson, H. C., Koekemoer, A. M., et al. 2004, ApJ, 600, L93

Gilli, R., Comastri, A., & Hasinger, G. 2007, A&A, 463, 79

Glikman, E., Bogosavljević, M., Djorgovski, S. G., et al. 2010, ApJ, 710, 1498

Glikman, E., Djorgovski, S. G., Stern, D., et al. 2011, ApJ, 728, L26+

Grazian, A., Salimbeni, S., Pentericci, L., et al. 2007, A&A, 465, 393

Green, J. C., Froning, C. S., Osterman, S., et al. 2012, ApJ, 744, 60

Haardt, F., & Madau, P. 1996, ApJ, 461, 20

—. 2012, ApJ, 746, 125

Haberzettl, L., Williger, G., Lehnert, M. D., Nesvadba, N., & Davies, L. 2012, ApJ, 745, 96

Haehnelt, M. G., & Rees, M. J. 1993, MNRAS, 263, 168

Hainline, K. N., Shapley, A. E., Kornei, K. A., et al. 2009, ApJ, 701, 52

Hartwick, F. D. A., & Schade, D. 1990, ARA&A, 28, 437

Hasinger, G. 2004, Nuclear Physics B Proceedings Supplements, 132, 86

—. 2008, A&A, 490, 905

Hasinger, G., Miyaji, T., & Schmidt, M. 2005, A&A, 441, 417

Hasinger, G., Cappelluti, N., Brunner, H., et al. 2007, ApJS, 172, 29

Hathi, N. P., Ryan, Jr., R. E., Cohen, S. H., et al. 2010, ApJ, 720, 1708

Henry, A., Scarlata, C., Domínguez, A., et al. 2013, ApJ, 776, L27

Henry, R. B. C., Edmunds, M. G., & Köppen, J. 2000, ApJ, 541, 660

Ho, L. C. 2008, ARA&A, 46, 475

Ho, L. C., Filippenko, A. V., & Sargent, W. L. W. 1997, ApJ, 487, 568

Holden, B. P., Oesch, P. A., Gonzalez, V. G., et al. 2014, ArXiv e-prints

Hopkins, P. F., Hernquist, L., Cox, T. J., et al. 2005a, ApJ, 630, 716

—. 2005b, ApJ, 632, 81

Hopkins, P. F., Somerville, R. S., Hernquist, L., et al. 2006, ApJ, 652, 864

Hunt, M. P., Steidel, C. C., Adelberger, K. L., & Shapley, A. E. 2004, ApJ, 605, 625

Ikeda, H., Nagao, T., Matsuoka, K., et al. 2011, ApJ, 728, L25+

—. 2012, ArXiv e-prints

Ilbert, O., Capak, P., Salvato, M., et al. 2009, ApJ, 690, 1236

Ilbert, O., Salvato, M., Le Floc'h, E., et al. 2010, ApJ, 709, 644

Jakobsen, P., Boksenberg, A., Deharveng, J. M., et al. 1994, Nature, 370, 35

Jannuzi, B. T., & Dey, A. 1999, in Astronomical Society of the Pacific Conference Series, Vol. 191, Photometric Redshifts and the Detection of High Redshift Galaxies, ed. R. Weymann, L. Storrie-Lombardi, M. Sawicki, & R. Brunner, 111

Jiang, L., Fan, X., Cool, R. J., et al. 2006, AJ, 131, 2788

Kakazu, Y., Cowie, L. L., & Hu, E. M. 2007, ApJ, 668, 853

Karim, A., Schinnerer, E., Martínez-Sansigre, A., et al. 2011, ApJ, 730, 61

Kashikawa, N., Aoki, K., Asai, R., et al. 2002, PASJ, 54, 819

Kauffmann, G., & Haehnelt, M. 2000, MNRAS, 311, 576

Kauffmann, G., Heckman, T. M., Tremonti, C., et al. 2003, MNRAS, 346, 1055

Kelson, D. D. 2003, PASP, 115, 688

Kennicutt, Jr., R. C. 1998, ARA&A, 36, 189

Kennicutt, Jr., R. C., & Hodge, P. W. 1986, ApJ, 306, 130

Kewley, L. J., & Dopita, M. A. 2002, ApJS, 142, 35

Kewley, L. J., Dopita, M. A., Leitherer, C., et al. 2013a, ApJ, 774, 100

Kewley, L. J., Dopita, M. A., Sutherland, R. S., Heisler, C. A., & Trevena, J. 2001, ApJ, 556, 121

Kewley, L. J., & Ellison, S. L. 2008, ApJ, 681, 1183

Kewley, L. J., Groves, B., Kauffmann, G., & Heckman, T. 2006, MNRAS, 372, 961

Kewley, L. J., Maier, C., Yabe, K., et al. 2013b, ArXiv e-prints

Kimble, R. A., MacKenty, J. W., O'Connell, R. W., & Townsend, J. A. 2008, in Society of Photo-Optical Instrumentation Engineers (SPIE) Conference Series, Vol. 7010, Society of Photo-Optical Instrumentation Engineers (SPIE) Conference Series

Kimura, M., Maihara, T., Iwamuro, F., et al. 2010, PASJ, 62, 1135

Kirkpatrick, J. D., Reid, I. N., Liebert, J., et al. 1999, ApJ, 519, 802

—. 2000, AJ, 120, 447

Kirkpatrick, J. D., Looper, D. L., Burgasser, A. J., et al. 2010, ApJS, 190, 100

Kirkpatrick, J. D., Cushing, M. C., Gelino, C. R., et al. 2011, ApJS, 197, 19

Kobulnicky, H. A., & Kewley, L. J. 2004, ApJ, 617, 240

Kobulnicky, H. A., Skillman, E. D., Roy, J.-R., Walsh, J. R., & Rosa, M. R. 1997, ApJ, 477, 679

Komiyama, Y., Miyazaki, S., Yagi, M., et al. 2003, in Society of Photo-Optical Instrumentation Engineers (SPIE) Conference Series, Vol. 4841, Society of Photo-Optical Instrumentation Engineers (SPIE) Conference Series, ed. M. Iye & A. F. M. Moorwood, 152–159

Koo, D. C., & Kron, R. G. 1982, A&A, 105, 107

Köppen, J., & Hensler, G. 2005, A&A, 434, 531

Kormendy, J., & Richstone, D. 1995, ARA&A, 33, 581

Law, D. R., Steidel, C. C., Erb, D. K., et al. 2009, ApJ, 697, 2057

Le Fèvre, O., Guzzo, L., Meneux, B., et al. 2005, A&A, 439, 877

Leauthaud, A., Massey, R., Kneib, J.-P., et al. 2007, ApJS, 172, 219

Leitherer, C. 2008, in IAU Symposium, Vol. 255, IAU Symposium, ed. L. K. Hunt, S. C. Madden, & R. Schneider, 305–309

Lelli, F., Verheijen, M., Fraternali, F., & Sancisi, R. 2012, A&A, 537, A72

Lequeux, J., Peimbert, M., Rayo, J. F., Serrano, A., & Torres-Peimbert, S. 1979, A&A, 80, 155

Levesque, E. M., Kewley, L. J., & Larson, K. L. 2010, AJ, 139, 712

Levesque, E. M., Leitherer, C., Ekstrom, S., Meynet, G., & Schaerer, D. 2012, ApJ, 751, 67

Levesque, E. M., & Richardson, M. L. A. 2013, ArXiv e-prints

Liang, Y. C., Yin, S. Y., Hammer, F., et al. 2006, ApJ, 652, 257

Lilly, S. J., Le Fèvre, O., Renzini, A., et al. 2007, ApJS, 172, 70

Liu, M. C., Dupuy, T. J., & Leggett, S. K. 2010, ApJ, 722, 311

Liu, M. C., & Leggett, S. K. 2005, ApJ, 634, 616

Liu, X., Shapley, A. E., Coil, A. L., Brinchmann, J., & Ma, C.-P. 2008, ApJ, 678, 758

Lodieu, N., Pinfield, D. J., Leggett, S. K., et al. 2007, MNRAS, 379, 1423

López-Sánchez, Á. R., & Esteban, C. 2010, A&A, 517, A85

Lucas, P. W., Tinney, C. G., Burningham, B., et al. 2010, MNRAS, 408, L56

Ly, C., Malkan, M. A., Hayashi, M., et al. 2011, ApJ, 735, 91

Ly, C., Malkan, M. A., Nagao, T., et al. 2013, ArXiv e-prints

Madau, P. 1995, ApJ, 441, 18

Madau, P., Ferguson, H. C., Dickinson, M. E., et al. 1996, MNRAS, 283, 1388

Madau, P., Haardt, F., & Rees, M. J. 1999, ApJ, 514, 648

Madau, P., Pozzetti, L., & Dickinson, M. 1998, ApJ, 498, 106

Magorrian, J., Tremaine, S., Richstone, D., et al. 1998, AJ, 115, 2285

Mannucci, F., Cresci, G., Maiolino, R., Marconi, A., & Gnerucci, A. 2010, MNRAS, 408, 2115

Marconi, A., Risaliti, G., Gilli, R., et al. 2004, MNRAS, 351, 169

Marinoni, C., Davis, M., Coil, A. L., & Finkbeiner, D. 2001, ArXiv Astrophysics e-prints

Markwardt, C. B. 2009, in Astronomical Society of the Pacific Conference Series, Vol. 411, Astronomical Society of the Pacific Conference Series, ed. D. A. Bohlender, D. Durand, & P. Dowler, 251–+

Maseda, M. V., van der Wel, A., da Cunha, E., et al. 2013, ArXiv e-prints

Massey, R., Rhodes, J., Leauthaud, A., et al. 2007, ApJS, 172, 239

Masters, D., & Capak, P. 2011, PASP, 123, 638

Masters, D., McCarthy, P., Burgasser, A. J., et al. 2012a, ApJ, 752, L14

Masters, D., Capak, P., Salvato, M., et al. 2012b, ApJ, 755, 169

McCarthy, P. J., Le Borgne, D., Crampton, D., et al. 2004, ApJ, 614, L9

McGaugh, S. S. 1991, ApJ, 380, 140

McNamara, B. R., & Nulsen, P. E. J. 2007, ARA&A, 45, 117

Metchev, S. A., Kirkpatrick, J. D., Berriman, G. B., & Looper, D. 2008, ApJ, 676, 1281

Miyaji, T., Griffiths, R. E., & C-COSMOS Team. 2008, in AAS/High Energy Astrophysics Division, Vol. 10, AAS/High Energy Astrophysics Division #10, #04.01–+

Mobasher, B., Capak, P., Scoville, N. Z., et al. 2007, ApJS, 172, 117

Momcheva, I. G., Lee, J. C., Ly, C., et al. 2013, AJ, 145, 47

Mortlock, D. J., Warren, S. J., Venemans, B. P., et al. 2011, Nature, 474, 616

Moster, B. P., Somerville, R. S., Newman, J. A., & Rix, H.-W. 2011, ApJ, 731, 113

Nakajima, K., Ouchi, M., Shimasaku, K., et al. 2013, ApJ, 769, 3

Nakajima, T., Oppenheimer, B. R., Kulkarni, S. R., et al. 1995, Nature, 378, 463

Newman, S. F., Buschkamp, P., Genzel, R., et al. 2013, ArXiv e-prints

Noeske, K. G., Weiner, B. J., Faber, S. M., et al. 2007, ApJ, 660, L43

O'Donnell, J. E. 1994, ApJ, 422, 158

Oke, J. B., Cohen, J. G., Carr, M., et al. 1995, PASP, 107, 375

Oppenheimer, B. R., Kulkarni, S. R., Matthews, K., & Nakajima, T. 1995, Science, 270, 1478

Osterbrock, D. E., & Ferland, G. J. 2006, Astrophysics of gaseous nebulae and active galactic nuclei

Pagel, B. E. J., Edmunds, M. G., Blackwell, D. E., Chun, M. S., & Smith, G. 1979, MNRAS, 189, 95

Pagel, B. E. J., Terlevich, R. J., & Melnick, J. 1986, PASP, 98, 1005

Pannella, M., Carilli, C. L., Daddi, E., et al. 2009, ApJ, 698, L116

Peng, Y.-j., Lilly, S. J., Kovač, K., et al. 2010, ApJ, 721, 193

Pérez-Montero, E., & Contini, T. 2009, MNRAS, 398, 949

Pettini, M., & Pagel, B. E. J. 2004, MNRAS, 348, L59

Pettini, M., Shapley, A. E., Steidel, C. C., et al. 2001, ApJ, 554, 981

Pickles, A. J. 1998, PASP, 110, 863

Pilyugin, L. S., Vílchez, J. M., & Contini, T. 2004, A&A, 425, 849

Pirzkal, N., Burgasser, A. J., Malhotra, S., et al. 2009, ApJ, 695, 1591

Polletta, M., Tajer, M., Maraschi, L., et al. 2007, ApJ, 663, 81

Probst, R. G., Montane, A., Warner, M., et al. 2003, in Society of Photo-Optical Instrumentation Engineers (SPIE) Conference Series, Vol. 4841, Society of Photo-Optical Instrumentation Engineers (SPIE) Conference Series, ed. M. Iye & A. F. M. Moorwood, 411–419

Quadri, R., Marchesini, D., van Dokkum, P., et al. 2007, AJ, 134, 1103

Reddy, N. A., Erb, D. K., Steidel, C. C., et al. 2005, ApJ, 633, 748

Reichard, T. A., Richards, G. T., Schneider, D. P., et al. 2003, AJ, 125, 1711

Reid, I. N., Kirkpatrick, J. D., Liebert, J., et al. 1999, ApJ, 521, 613

Reimers, D., Kohler, S., Wisotzki, L., et al. 1997, A&A, 327, 890

Renzini, A., & Voli, M. 1981, A&A, 94, 175

Richard, J., Jones, T., Ellis, R., et al. 2011, MNRAS, 413, 643

Richards, G. T., Croom, S. M., Anderson, S. F., et al. 2005, MNRAS, 360, 839

Richards, G. T., Strauss, M. A., Fan, X., et al. 2006, AJ, 131, 2766

Richards, G. T., Myers, A. D., Gray, A. G., et al. 2009, ApJS, 180, 67

Richardson, M. L. A., Levesque, E. M., McLinden, E. M., et al. 2013, ArXiv e-prints

Richstone, D., Ajhar, E. A., Bender, R., et al. 1998, Nature, 395, A14+

Rigby, J. R., Wuyts, E., Gladders, M. D., Sharon, K., & Becker, G. D. 2011, ApJ, 732, 59

Robertson, B. E., Ellis, R. S., Dunlop, J. S., McLure, R. J., & Stark, D. P. 2010, Nature, 468, 49

Ryan, R. E., Thorman, P. A., Yan, H., et al. 2011, ApJ, 739, 83

Salvato, M., Hasinger, G., Ilbert, O., et al. 2009, ApJ, 690, 1250

Salvato, M., Ilbert, O., Hasinger, G., et al. 2011, ApJ, 742, 61

Sanders, D. B., Salvato, M., Aussel, H., et al. 2007, ApJS, 172, 86

Scarlata, C., Carollo, C. M., Lilly, S. J., et al. 2007, ApJS, 172, 494

Schmidt, M. 1963, Nature, 197, 1040

—. 1968, ApJ, 151, 393

Schmidt, M., & Green, R. F. 1983, ApJ, 269, 352

Schneider, D. P., Richards, G. T., Hall, P. B., et al. 2010, AJ, 139, 2360

Scholz, R.-D., Bihain, G., Schnurr, O., & Storm, J. 2011, A&A, 532, L5

Scoville, N., Aussel, H., Brusa, M., et al. 2007, ApJS, 172, 1

Scoville, N., Arnouts, S., Aussel, H., et al. 2013, ApJS, 206, 3

Shankar, F., & Mathur, S. 2007, ApJ, 660, 1051

Shapley, A. E., Coil, A. L., Ma, C.-P., & Bundy, K. 2005, ApJ, 635, 1006

Shapley, A. E., Steidel, C. C., Pettini, M., & Adelberger, K. L. 2003, ApJ, 588, 65

Shen, Y., Strauss, M. A., Oguri, M., et al. 2007, AJ, 133, 2222

Sheth, K., Elmegreen, D. M., Elmegreen, B. G., et al. 2008, ApJ, 675, 1141

Shim, H., Chary, R.-R., Dickinson, M., et al. 2011, ApJ, 738, 69

Shirazi, M., Brinchmann, J., & Rahmati, A. 2013, ArXiv e-prints

Shull, J. M., France, K., Danforth, C. W., Smith, B., & Tumlinson, J. 2010, ApJ, 722, 1312

Siana, B., Polletta, M. d. C., Smith, H. E., et al. 2008, ApJ, 675, 49

Silverman, J. D., Green, P. J., Barkhouse, W. A., et al. 2008, ApJ, 679, 118

Simcoe, R. A., Burgasser, A. J., Bernstein, R. A., et al. 2008, in Society of Photo-Optical Instrumentation Engineers (SPIE) Conference Series, Vol. 7014, Society of Photo-Optical Instrumentation Engineers (SPIE) Conference Series

Simcoe, R. A., Burgasser, A. J., Bochanski, J. J., et al. 2010, in Society of Photo-Optical Instrumentation Engineers (SPIE) Conference Series, Vol. 7735, Society of Photo-Optical Instrumentation Engineers (SPIE) Conference Series

Skillman, E. D. 1989, ApJ, 347, 883

Smith, L. J., Westmoquette, M. S., Gallagher, J. S., et al. 2006, MNRAS, 370, 513

Sobral, D., Best, P. N., Matsuda, Y., et al. 2012, MNRAS, 420, 1926

Sokasian, A., Abel, T., & Hernquist, L. 2002, MNRAS, 332, 601

Stark, D. P., Schenker, M. A., Ellis, R. S., et al. 2012, ArXiv e-prints

Steffen, A. T., Barger, A. J., Cowie, L. L., Mushotzky, R. F., & Yang, Y. 2003, ApJ, 596, L23

Steffen, A. T., Strateva, I., Brandt, W. N., et al. 2006, AJ, 131, 2826

Steidel, C. C., Giavalisco, M., Pettini, M., Dickinson, M., & Adelberger, K. L. 1996, ApJ, 462, L17

Steidel, C. C., Shapley, A. E., Pettini, M., et al. 2004, ApJ, 604, 534

Stern, D., Moran, E. C., Coil, A. L., et al. 2002, ApJ, 568, 71

Stern, D., Eisenhardt, P., Gorjian, V., et al. 2005, ApJ, 631, 163

Straughn, A. N., Kuntschner, H., Kümmel, M., et al. 2011, AJ, 141, 14

Strauss, M. A., Fan, X., Gunn, J. E., et al. 1999, ApJ, 522, L61

Sumi, T., Kamiya, K., Bennett, D. P., et al. 2011, Nature, 473, 349

Telfer, R. C., Zheng, W., Kriss, G. A., & Davidsen, A. F. 2002, ApJ, 565, 773

Teplitz, H. I., Capak, P., Hanish, D., et al. 2012, in American Astronomical Society Meeting Abstracts, Vol. 219, American Astronomical Society Meeting Abstracts, 428.06

Thurston, T. R., Edmunds, M. G., & Henry, R. B. C. 1996, MNRAS, 283, 990

Treister, E., & Urry, C. M. 2006, ApJ, 652, L79

Treister, E., Urry, C. M., Chatzichristou, E., et al. 2004, ApJ, 616, 123

Tremonti, C. A., Heckman, T. M., Kauffmann, G., et al. 2004, ApJ, 613, 898

Trump, J. R., Impey, C. D., McCarthy, P. J., et al. 2007, ApJS, 172, 383

Trump, J. R., Impey, C. D., Elvis, M., et al. 2009, ApJ, 696, 1195

Trump, J. R., Weiner, B. J., Scarlata, C., et al. 2011, ApJ, 743, 144

Trump, J. R., Konidaris, N. P., Barro, G., et al. 2012, ArXiv e-prints

—. 2013, ApJ, 763, L6

Ueda, Y., Akiyama, M., Ohta, K., & Miyaji, T. 2003, ApJ, 598, 886

van der Wel, A., Straughn, A. N., Rix, H.-W., et al. 2011, ApJ, 742, 111

van Zee, L., & Haynes, M. P. 2006, ApJ, 636, 214

van Zee, L., Salzer, J. J., Haynes, M. P., O'Donoghue, A. A., & Balonek, T. J. 1998, AJ, 116, 2805

Vanden Berk, D. E., Richards, G. T., Bauer, A., et al. 2001, AJ, 122, 549

Veilleux, S., & Osterbrock, D. E. 1987, ApJS, 63, 295

Villar, V., Gallego, J., Pérez-González, P. G., et al. 2008, ApJ, 677, 169

Vrba, F. J., Henden, A. A., Luginbuhl, C. B., et al. 2004, AJ, 127, 2948

Walsh, J. R., & Roy, J.-R. 1987, ApJ, 319, L57

Welch, G. A. 1970, ApJ, 161, 821

Westmoquette, M. S., James, B., Monreal-Ibero, A., & Walsh, J. R. 2013, A&A, 550, A88

Wittman, D. M., Tyson, J. A., Dell'Antonio, I. P., et al. 2002, in Society of Photo-Optical Instrumentation Engineers (SPIE) Conference Series, Vol. 4836, Society of Photo-Optical Instrumentation Engineers (SPIE) Conference Series, ed. J. A. Tyson & S. Wolff, 73–82

Wolf, C., Wisotzki, L., Borch, A., et al. 2003, A&A, 408, 499

Woodgate, B. E., Kimble, R. A., Bowers, C. W., et al. 1998, PASP, 110, 1183

Wright, E. L., Eisenhardt, P. R. M., Mainzer, A. K., et al. 2010, AJ, 140, 1868

Wuyts, E., Rigby, J. R., Gladders, M. D., et al. 2012, ApJ, 745, 86

Wyithe, J. S. B., & Loeb, A. 2003, ApJ, 595, 614

Xia, L., Malhotra, S., Rhoads, J., et al. 2012, AJ, 144, 28

York, D. G., Adelman, J., Anderson, Jr., J. E., et al. 2000, AJ, 120, 1579

Young, M., Elvis, M., & Risaliti, G. 2010, ApJ, 708, 1388

Yu, Q., & Tremaine, S. 2002, MNRAS, 335, 965

Zahid, H. J., Bresolin, F., Kewley, L. J., Coil, A. L., & Davé, R. 2012, ApJ, 750, 120

Zaritsky, D., Kennicutt, Jr., R. C., & Huchra, J. P. 1994, ApJ, 420, 87

Appendix A

SpecPro Software

We present an interactive IDL program for viewing and analyzing astronomical spectra in the context of modern imaging surveys. SpecPro's interactive design lets the user simultaneously view spectroscopic, photometric, and imaging data, allowing for rapid object classification and redshift determination. The spectroscopic redshift can be determined with automated cross-correlation against a variety of spectral templates or by overlaying common emission and absorption features on the 1-D and 2-D spectra. Stamp images as well as the spectral energy distribution (SED) of a source can be displayed with the interface, with the positions of prominent photometric features indicated on the SED plot. Results can be saved to file from within the interface. In this paper we discuss key program features and provide an overview of the required data formats.

A.1 Introduction

Modern imaging surveys such as the Cosmic Evolution Survey (COSMOS) (Scoville et al. 2007)) and the Great Observatories Origins Deep Survey (GOODS) (Giavalisco et al. 2004) contain a wealth of galaxy information in the form of stamp images and multiwavelength photometry across the electromagnetic spectrum. Spectroscopy adds to preexisting survey data through, among other information, precise redshift determination and firm galaxy classification based on spectral features. While spectral analysis can be automated in some cases, human examination is often necessary. This is especially true when the spectroscopic targets are faint or unusual sources for which automated redshift determination is not reliable.

Imaging and photometric data from a multiwavelength survey can play a vital role in deciphering difficult spectra. For example, a high-redshift galaxy is expected to have a strong photometric break (the "Lyman break") at rest-frame λ1216 Å, with essentially no flux short of the rest-frame λ912 Å Lyman limit. The presence of this spectral break in the SED can suggest an initial redshift guess and validate a high-redshift assignment based on weak spectral features. Conversely, photometric detections blueward of the Lyman limit can preclude a high-redshift assignment. As another example, passive galaxies typically show a peak in the SED near rest-frame 1.6 μm and a spectral break near rest-frame λ4000 Å, while their spectra reveal little more than faint absorption features. Again, the photometric characteristics can be used to inform the redshift assignment. Stamp images of a source can also be very helpful in resolving puzzling spectra, as they reveal the morphology and spatial extent of a source as well as possible sources of photometric or spectroscopic contamination. High-resolution imaging can thus help to distinguish stars from galaxies and reveal nearby or coincident systems giving rise to anamolous spectra.

With the large numbers of spectra taken in survey fields, it is necessary to have a means of rapid spectral analysis. SpecPro was developed to analyze faint spectra of high-redshift galaxies and active galactic nuclei (AGN) in the COSMOS field, where the available photometric data effectively provides low-resolution spectra covering 0.1 to 8 μm. The spectra, taken with the Keck II DEIMOS multislit spectrometer (Faber et al. 2003), often show few strong features. By incorporating the SED and postage stamp images from COSMOS in the SpecPro interface we have significantly improved our ability to find redshifts and understand our galaxy sample. In addition to facilitating the analysis of faint sources, the cross-correlation capability makes redshift determination for bright sources extremely fast.

Since SpecPro was originally designed to examine spectra taken with a multislit spectrometer, data structures are organized around the idea of a slit mask. Data directories contain files for sources on a mask, the files within the mask directory being differentiated by slit number. Aside from this general structure, we have made the input formats quite flexible in order to accommodate data from other instruments/surveys. In addition to DEIMOS, the code has to date been used successfully with data from the IMACS multislit spectrometer on Magellan (Dressler et al. 2006) as well as the FMOS fiber spectrometer and FOCAS multisplit spectrometer, both on Subaru (Kashikawa et al. 2002; Kimura et al. 2010). Any spectroscopic data can be viewed with SpecPro after conforming to the simple formats outlined in Section 3.

The structure of this paper is as follows. In Section 2 we provide an overview of the interface and discuss the motivation behind its design. In Section 3 we discuss the inputs to the program. Section 4 concludes with a summary and a brief discussion of possible further development.

The code with installation instructions as well as example data, an overview of data formats, and a brief tutorial are available at http://specpro.caltech.edu.

A.2 SpecPro Overview

The SpecPro interface is shown in Figures A.1 and A.2. Figure A.1 shows the full interface, while Figure A.2 shows a smaller version that can be invoked for use on smaller monitors. A galaxy with strong emission lines from the COSMOS survey is displayed.

Surrounding the data displays are widgets allowing the user to perform various tasks, such as navigate through spectra in the mask directory, adjust the current redshift guess, bin and smooth the 1-D spectrum, overlay galaxy templates, plot the redshifted positions of common emission and absorption features, change stamp image and 2-D spectrum contrast, and save results to an external file. In the following sections we outline the key capabilities of the interface, emphasizing how they assist in spectral analysis.

It is worth emphasizing that the SpecPro interface does not require all of the various pieces of information (2-D spectrum, stamp images, SED) to run. It can be used with a subset of this information and the windows for which there is no data are left blank. Therefore the interface can be used to view and analyze spectra for which the data associated with a multiwavelength survey is absent, or to pre-select targets for spectroscopy using just photometric and imaging data.

A.2.1 Stamp images

Available stamp images of the source are displayed on the left side of the interface in 100x100 pixel windows. Under the final window is a scroll list containing the names of overflow images. The user can click entries in this list to display them in the final stamp window, allowing an arbitrary number of stamp images to be stored and viewed with the interface. The images are displayed in the order in which they are stored in the structure array, beginning with the upper left stamp window and going down.

The displayed images are signal-to-noise (S/N) plots generated by dividing the image flux by the average error in the image. This maximizes the dynamic range in order to display both bright sources and faint counterparts blueward of a spectral break. By viewing the stamps the user can quickly determine the source of a serendipitous spectrum and whether photometric points in the source SED correspond to real detections or artifacts.

Selecting the "Show extraction" button (located underneath the 2-D plot window) causes the scale in arcseconds to be displayed on the stamps. In addition, if the slit information (RA, DEC, length, width, and angle) is provided, it is plotted over the stamp images, as in Figures A.1 and A.2.

A.2.2 Spectrum Display

The one-dimensional spectrum is displayed in the upper right window of the display. The spectrum is shown in white, with overlaid spectral templates shown in blue. Regions of significant atmospheric absorption are indicated with horizontal blue lines. The residual error, which can help determine whether a weak feature is real or an artifact due to sky subtraction, can be overlaid on the plot by clicking the "Show sky" button on the second row down from the 1-D display.

The 1-D spectrum can be binned and smoothed to bring out features in low S/N spectra. Binning combines pixels, reducing the resolution of the spectrum to increase the S/N, while smoothing performs an inverse variance weighted average in the vicinity of each pixel to reduce the noise. In Figure A.1 the spectrum has been binned and smoothed, clearly revealing prominent emission features.

The 2-D spectrum is displayed beneath the 1-D spectrum, binned, if necessary, to fit the display. The 2-D spectrum can be helpful to: (1) verify the fidelity of the 1-D spectrum, (2) determine whether features observed in the 1-D spectrum are real or artifacts, (3) identify serendipitous objects, and (4) examine the spatial morphology of emission features. As described in Section 2.3, the user has the ability to reextract the 1-D spectrum from the 2-D, which can be very useful in cases in which there was a problem with 1-D extraction or the 1-D spectrum of a serendipitous source is desired.

The contrast of the 2-D spectrum can be adjusted with a slider widget. Next to the contrast slider is a droplist widget labeled "Max sigma:". This is set to 10 by default, which indicates that contrast scaling has an upper limit of 10σ, so that pixels 10σ from the mean are rescaled to the maximum pixel value of 255. Lowering this value can help in cases in which the spectrum of interest is being drowned out by the light of bright serendipitous sources.

The positions (observed-frame) of emission and absorption features of different galaxy types can be displayed over both the 1-D and the 2-D spectrum by selecting the buttons above the 2-D display. Typical lines from star-forming galaxies, passive galaxies, quasistellar objects (QSOs), Seyferts, and high-redshift galaxies can be selected. Redshifts can be found manually by overlaying the appropriate lines on the spectrum and adjusting the redshift until they line up with observed spectral features. These lines can also be used to identify absorption and emission features in the various spectral templates.

Both the 1-D and the 2-D spectrum can be zoomed on by clicking, dragging and releasing around the region of interest. In the case of the 2-D, this action causes the zoomed region to be displayed in its unbinned state in a separate window. This can be helpful, for instance, to determine whether an emission feature is [OII] or Lyα, which can often be deduced from the morphology of the emission line.

A.2.3 Reextraction of 1-D spectrum

It is often necessary to reextract the 1-D spectrum from the 2-D, particularly in order to recover serendipitously observed sources that fall in the slit. We have provided a method of easily reextracting the 1-D spectrum from the 2-D, adapting the routine extract1d.pro from the DEIMOS DEEP2 pipeline code (Marinoni et al. 2001) for this purpose. To reextract, the user places the cursor over the 2-D spectrum at the vertical position desired, then clicks, drags horizontally (by any amount, in either direction) and releases. This triggers the reextraction, and when it is complete the 1-D plot is updated with the newly extracted spectrum. A dialog box lets the user save the extracted 1-D spectrum in .fits format.

A.2.4 SED

The source SED is displayed in the bottom right window of the interface. The information for this plot comes from the photometry file, described in Section 3.5. The plot extends from 0.1 to 10 μm and displays photometric AB magnitudes with errors. The effective widths of the photometric bands are indicated with horizontal bars and errors in the magnitude estimates are indicated with vertical bars. Observed-frame positions of important SED features are indicated with vertical blue lines. These features include the Lyman limit at 912 Å, Lyα at 1216 Å, the 4000 Å break, and the typical SED peak of evolved galaxies at 1.6 μm. The wavelength coverage of the spectrum is indicated with vertical green lines.

A.2.5 Cross-Correlation

Automated redshift determination by convolution against spectral templates is a powerful and time-saving capability. We have adapted cross-correlation routines originally written for the SDSS spectral reduction package for use in SpecPro, with a library of spectral templates available to correlate against (see Table 1). The templates span a broad range of galaxy types. We have also included some stellar templates to help identify high-redshift selected sources that are actually stars.

The user is expected to be able to choose an appropriate template based on the spectrum and other information about the source. When one of the galaxy templates from the template library is selected, the six best redshift matches are computed and the best solution is displayed. The droplist "Auto-z solution:" under the 1-D spectrum contains all of the solutions for examination. Clicking an alternate solution will switch to the new redshift guess and move the template accordingly. Because the spectral template is overplotted on the 1-D spectrum, the accuracy of the result can be easily checked. The template can be scaled via the "Template scaling:" button to provide a better visual match to the spectrum.

In some cases cross-correlation fails to find the solution, even though the correct answer is apparent to the user. In this case the redshift can be adjusted manually to find the answer, but finding the exact solution can be time consuming. Therefore we added an "Auto center" button that cross-correlates against the currently selected galaxy template in a small region (z $\pm$ 0.05) around the current redshift guess.

In some very difficult cases cross-correlation will fail to find the correct redshift, even using auto-centering. In these unusual instances the user must resort to adjusting the redshift manually to the correct answer.

Table A.1. Spectral templates available for cross-correlation in SpecPro.

Template	**Description**
VVDS LBG	Lyman-break galaxy template from the VIRMOS-VLT Deep Survey
VVDS Elliptical	Passive galaxy template, strong absorption, no emission
VVDS S0	S0 classification template, weak emission, absorption
VVDS Early Spiral	Stronger emission, less absorption
VVDS Spiral	Typical spiral spectrum, with strong emission features
VVDS Starburst	Extremely strong nebular emission features
SDSS Quasar	Typical broad-line quasar spectrum from the Sloan Digital Sky Survey
Red Galaxy	Passive galaxy template from PEGASE spectral evolution model
Green Galaxy	Early spiral/spiral template from PEGASE
Blue Galaxy	Spiral/Starburst template from PEGASE
LBG Shapley	Lyman-break galaxy template from Shapley et al. (2003)
SDSS LoBAL	Low-ionization broad absorption line (BAL) quasar template
SDSS HiBAL	High-ionization BAL quasar template
A0-M6	Stellar templates from the Pickles catalog (Pickles 1998)

A.2.6 Output

The interface allows the user to rapidly record results to a formatted file. To the left of the SED plot window are four output fields with which the user can save the redshift, a confidence associated with it, their initials, and notes on the spectrum. The output is saved in ascii format and contains the mask name, source name, slit number, RA, and DEC as well as the redshift result. Results are always appended to the end of the selected output file and multiple entries for a single source can be added. Once an output file has been selected, it is the default output location for the rest of the SpecPro session.

The "Save Spec1D" button saves the displayed 1-D spectrum (wavelength and flux at the current zoom, bin, and smooth level) to an ascii file for plotting in other programs. In addition, images in .tif format of any of the data windows can be saved by double-clicking on them.

A.3 Data Formats

We have attempted to make the required formats simple and general so that data from any instrument/survey can be easily adapted for use with SpecPro. While the files are expected to be arranged by slit number, any sequential numbering scheme can be used to differentiate sources. None of the inputs accepted by SpecPro are actually required for the program to run; if one is missing, the corresponding field in the interface is left blank. The program accepts the following five files:

- 1-D spectrum file (fits)
- 2-D spectrum file (fits)

- Stamp image file (fits)
- Photometry file (ascii)
- Information file (ascii)

These are briefly described in the rest of this section. More detailed descriptions are given on the website, and example data is provided with the program download.

A.3.1 1-D Spectrum

The 1-D spectrum is a stored as a structure with three fields: *flux*, *ivar*, and *lambda*. Each field holds a one-dimensional double array. The *flux* field is the spectrum, the *ivar* field is the inverse variance of the flux, and *lambda* is the wavelength at each pixel, in angstroms. Note that the units of flux are arbitrary, but values proportional to F_ν are preferable because this matches the units of the spectral templates. The structure must be saved in FITS format.

A.3.2 2-D Spectrum

The 2-D spectrum is also stored in a structure with the three fields *flux*, *ivar*, and *lambda*. However, each field here is a two-dimensional double array, including the *lambda* field, which contains the wavelength solution for each pixel in the 2-D spectrum. The 2-D spectrum is stored in FITS format.

A.3.3 Stamp Images

Stamp images of the source are stored in a single FITS file, with the data stored as an array of structures. Each element in the array contains a stamp image and ancillary information, with the size of the array determined by how many stamps are available. The stamp structures must all be of the same form, with fields as follows:

- *name* - string giving name of the image, e.g. “U band”
- *flux* - 100x100 double array
- *ivar* - 100x100 double array
- *RA* - image center in degrees, double
- *DEC* - image center in degrees, double
- *pixscale* - arcseconds per pixel, double

The stamps should be oriented with north up. If the inverse variance for the image is not available then it should either be approximated in some way or set to all zeros.

A.3.4 Information File

The information file contains ancillary information about a source displayed by the interface and/or used in some of its functionality. This information includes source RA and DEC, slit information, photometric redshift estimate, and other quantities (see the website for a detailed description). If the user only has a subset of the information they can omit the missing values, or set them to zero.

A.3.5 Photometry

The photometry file is a space delimited file with five columns: filter name, filter central wavelength, effective filter bandwidth, AB magnitude, and AB magnitude error. Both the filter central wavelength and effective filter bandwith should be expressed in angstroms. Non-detections are indicated with an AB magnitude of -99, with the AB magnitude error set to the lower bound on the AB magnitude established by the non-detection. Any photometric point can be included, but the program's SED plot extends from 0.1 to 10.0 μm.

A.4 Summary

SpecPro is an interactive IDL-based interface particularly suited to viewing astronomical spectra in the context of multiwavelength surveys. In addition to 1-D and 2-D spectra, the interface can display stamp images and the spectral energy distribution of the source. Having all of this information in one display makes it much easier to identify the nature and redshift of faint spectral targets.

We have made an effort to make the data formats required by the program both simple and general. The program could potentially incorporate wrappers for various instrument's data or allow more flexible inputs; however, the effort required to achieve this flexibility is probably too high considering the relative ease with which data can be made to conform with the formats outlined in Section 3.

One possibility for future development is to incorporate tools for more detailed spectroscopic analysis (line-fitting, determination of equivalent widths, etc.) from within the interface. This was not the intention when designing SpecPro, but the addition of such functionality would make it a much more general tool for spectral analysis. Another related possibility would be to allow the user to interactively fit the source SED from within the interface, in order to determine galaxy stellar mass, age, and other parameters. However, at present the interface is optimized for spectral classification and redshift determination and we have no concrete plans for further development.

We have found the program valuable in our own analysis of DEIMOS spectra of targets in the COSMOS survey field. In addition to making the identification of redshifts very fast, it has also allowed us to efficiently characterize our sample and identify particularly interesting galaxies for follow-up study. We feel that SpecPro will prove useful to others working with spectroscopic samples as well.

The authors would like to thank Dr. Yuko Kakazu, Dr. Hai Fu, Dr. Lin Yan, and Dr. Nick Scoville from the California Institute of Technology for their helpful comments and suggestions during the development of the software. In addition, we would like to acknowledge and thank Dr. Mara Salvato of the Max Planck Institute for Plasma Physics and Dr. Francesca Civano of the Harvard-Smithsonian Center for Astronomy for providing useful feedback on early versions of the code. We also thank Dr. Bahram Mobasher of the University of California, Riverside for carefully reading a draft of this paper and making suggestions that significantly improved its content.

SpecPro makes use of IDL code written and maintained by others. We thank Wayne Landsman at NASA/GSFC for his work maintaining the IDL Astronomy User's Library. We also thank the authors of code we have used for our implementation of automated cross-correlation, including David Schlegel, Doug Finkbeiner, Michael Cooper, and John Johnson. We thank Craig Markwardt, whose MPFIT least-squares fitting package (Markwardt 2009) is integral to the cross-correlation functionality.

Finally, we thank an anonymous referee for carefully reading this manuscript and providing very constructive feedback both in terms of content and with regard to the distribution of the software on the web.

This work was supported in part by a visiting graduate student fellowship at the Caltech Infrared Processing and Analysis Center (IPAC).

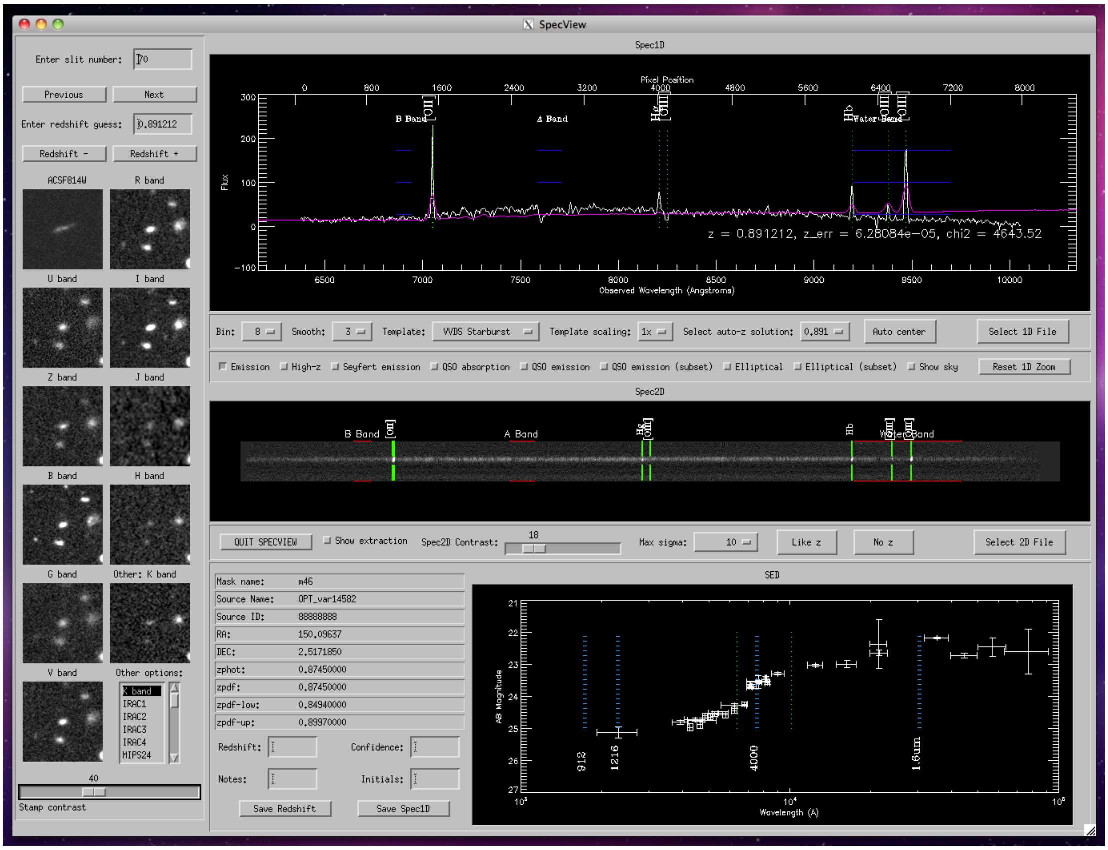

Figure A.1 The SpecPro widget interface. The object shown is a star-forming galaxy at redshift 0.89. Stamp images of the source are displayed on the left side of the interface, and the 1-D spectrum is displayed in the upper right window. On the 1-D plot, vertical lines mark the positions of prominent emission features, and a spectral template is overlaid in blue. Under the 1-D spectrum is the corresponding 2-D spectrum, binned to fit the display. The same emission lines plotted over the 1-D spectrum are indicated in the 2-D spectrum. Emission lines ([OII], Hγ, Hβ, [OIII]) are easily visible in the binned 2-D image. The window on the bottom right shows the SED of the source from the ultraviolet to the mid-infrared. The AB magnitude (increasing downwards) is plotted against filter wavelength. The observed-frame positions of important photometric indicators, including the Lyman limit at λ912 Å, Lyα at λ1216 Å, the 4000 Å break, and 1.6 μm are indicated with vertical dashed lines.

Figure A.2 The SpecPro widget interface, small version. In this image, the "Show extraction" button has been selected, causing the slit to be overlaid on the stamp images.

Appendix B

Supplemental WFC3 data and FIRE 1D spectra

Here we show the WFC3 grism spectra, direct H-band images, and measured lines from FIRE spectroscopy for the $z \sim 2$ sample presented in Chapter 3. For each object we show the WFC3 direct image and grism spectrum on top and the 1D emission lines measured from the FIRE spectroscopy on the bottom. The error spectra are shown in the lower panels. Fits to the emission lines are shown in green. Non-detections of [N II]λ6583 are indicated with down arrows. When lines are not shown they typically were not measurable due to interference from OH sky emission lines.

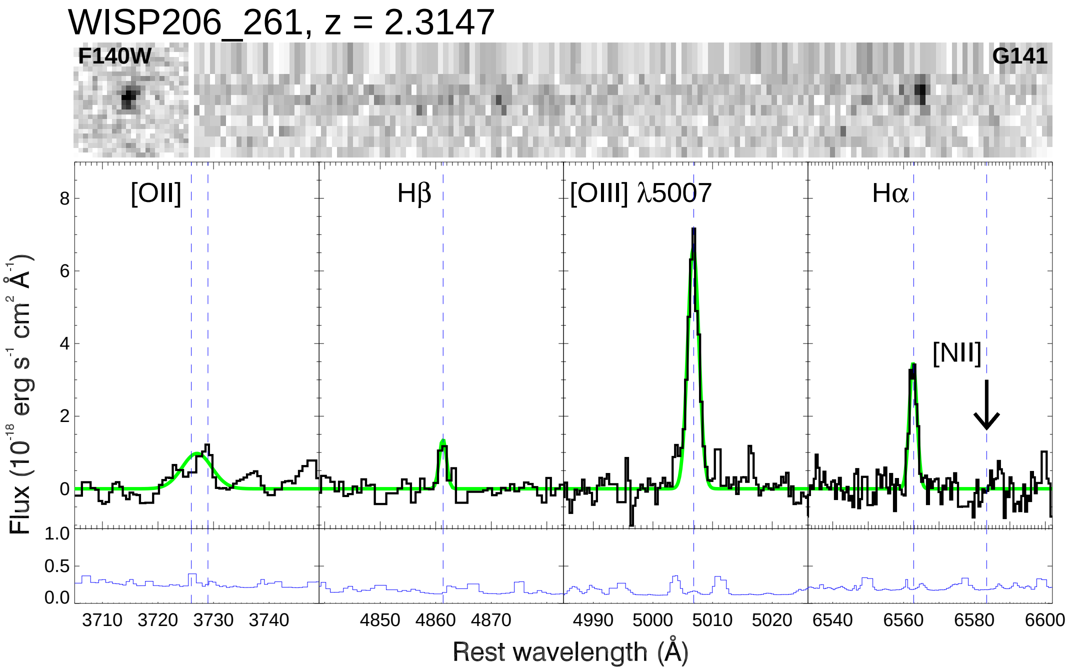

WISP206_261, z = 2.3147
F140W
G141
[OII]
Hβ
[OIII] λ5007
Hα
[NII]
Flux (10^{-18} erg s^{-1} cm^{2} $Å^{-1}$)
Rest wavelength (Å)

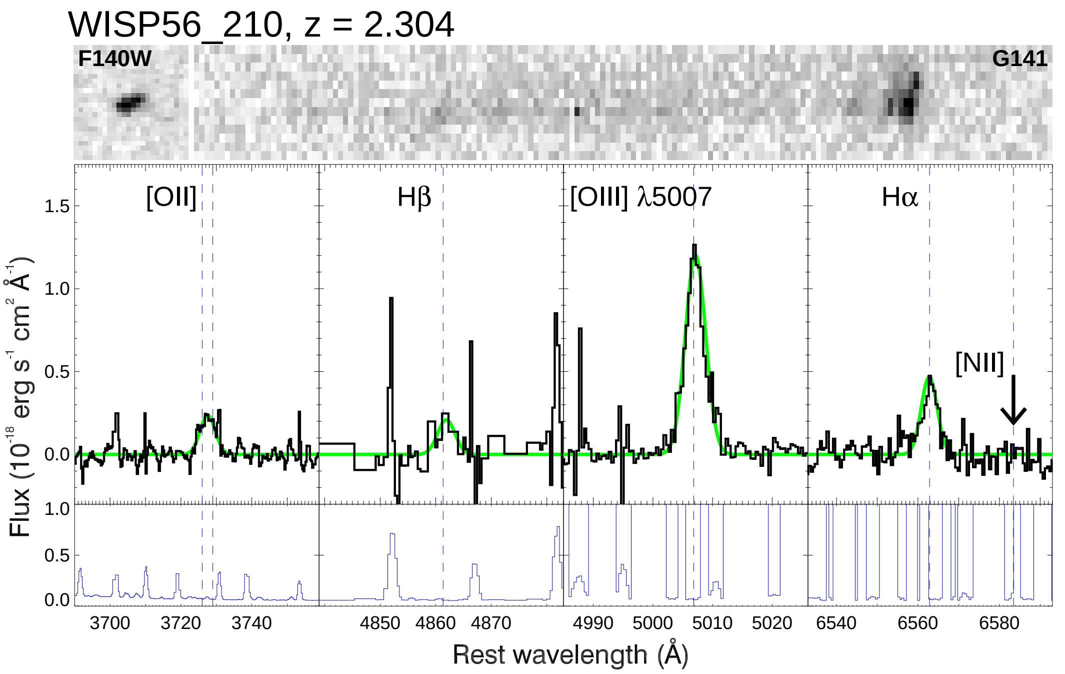

WISP56_210, z = 2.304
F140W
G141
[OII]
Hβ
[OIII] λ5007
Hα
[NII]
Flux (10^{-18} erg s^{-1} cm^{2} $Å^{-1}$)
Rest wavelength (Å)

Figure B.1

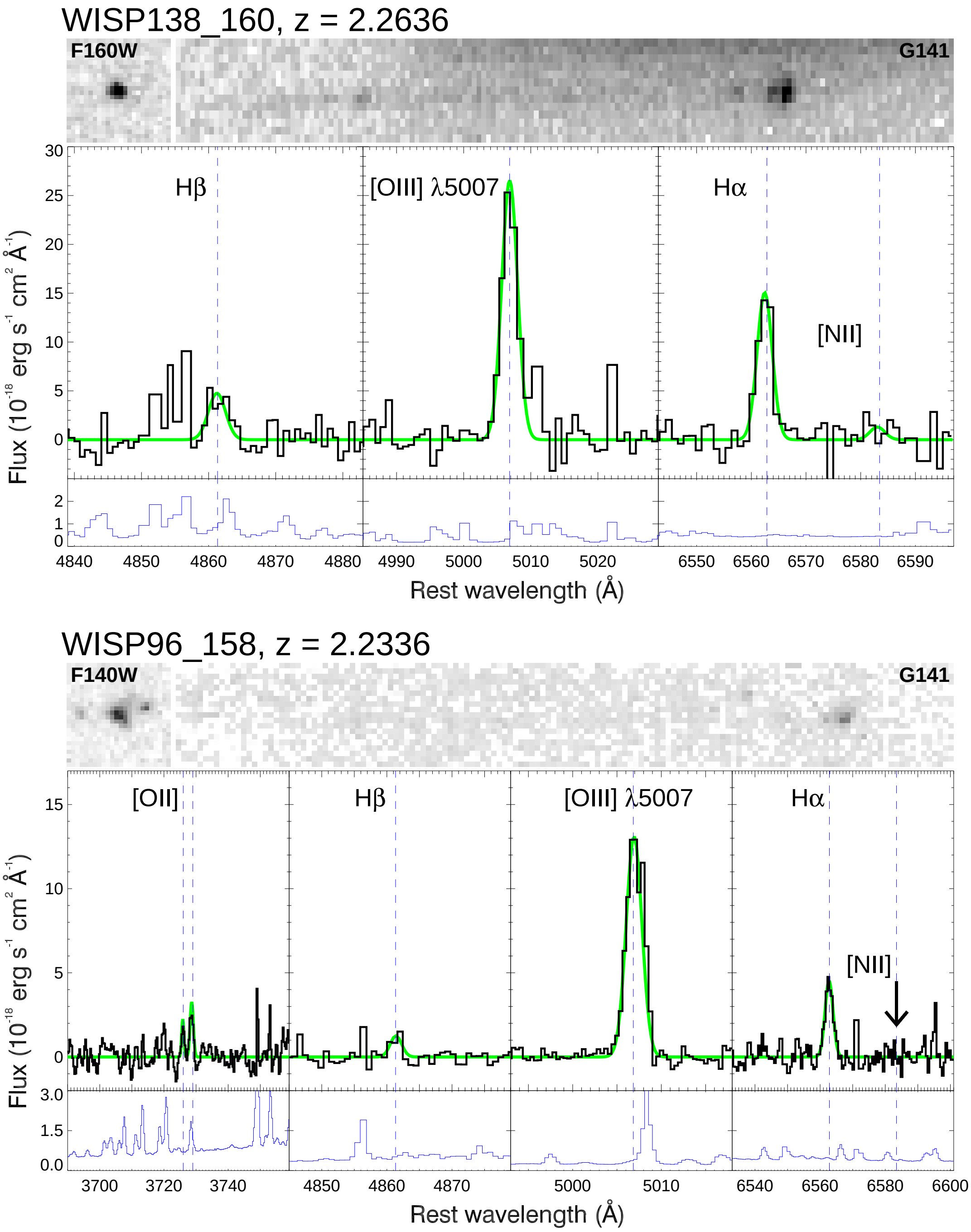
WISP138_160, z = 2.2636
F160W
G141
Hβ
[OIII] λ5007
Hα
[NII]
Flux (10^-18 erg s^-1 cm^2 Å^-1)
Rest wavelength (Å)
WISP96_158, z = 2.2336
F140W
G141
[OII]
Hβ
[OIII] λ5007
Hα
[NII]
Flux (10^-18 erg s^-1 cm^2 Å^-1)
Rest wavelength (Å)

Figure B.2

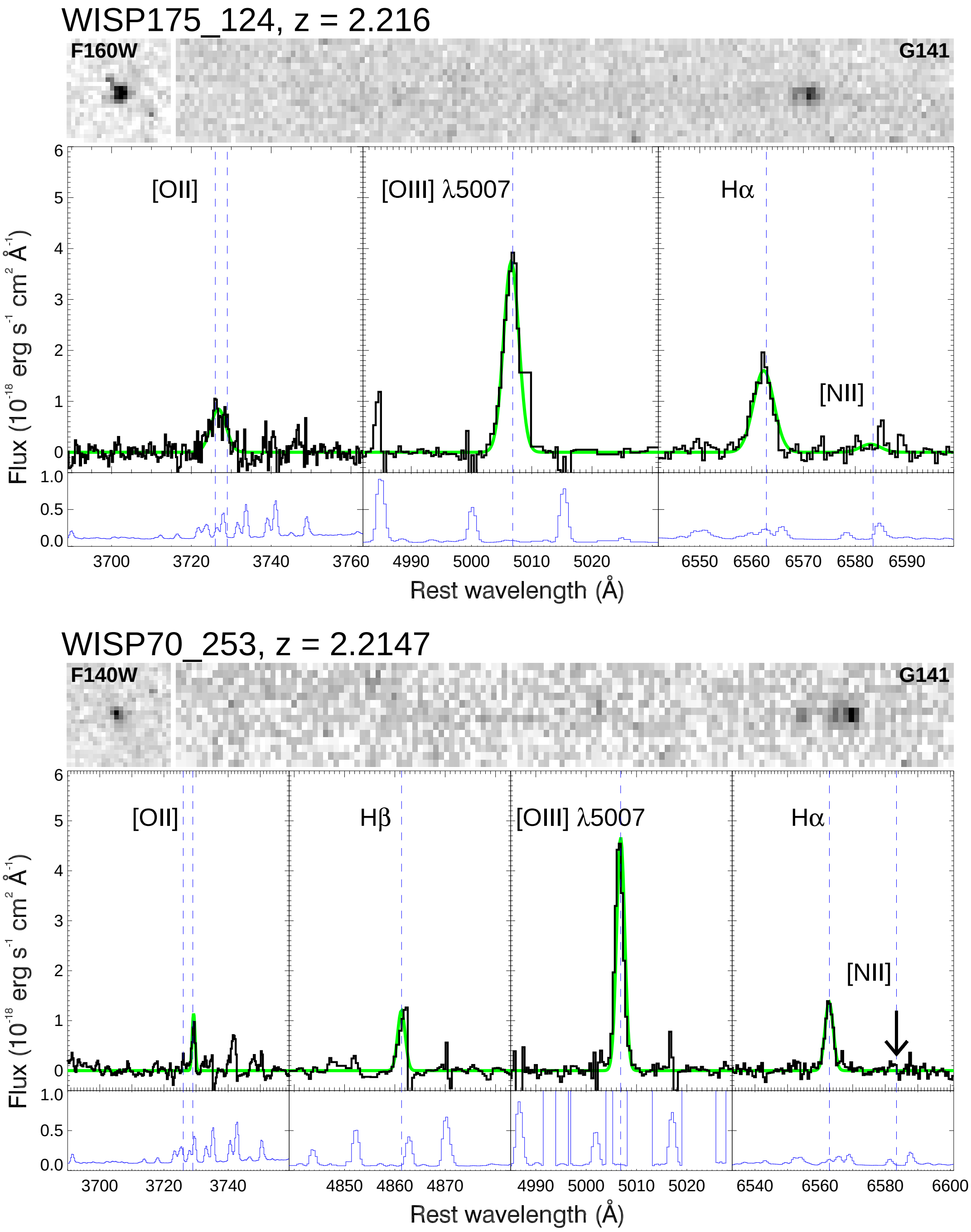
WISP175_124, z = 2.216
F160W
G141
[OII]
[OIII] λ5007
Hα
[NII]
Flux (10^-18 erg s^-1 cm^2 Å^-1)
Rest wavelength (Å)
WISP70_253, z = 2.2147
F140W
G141
[OII]
Hβ
[OIII] λ5007
Hα
[NII]
Flux (10^-18 erg s^-1 cm^2 Å^-1)
Rest wavelength (Å)

Figure B.3

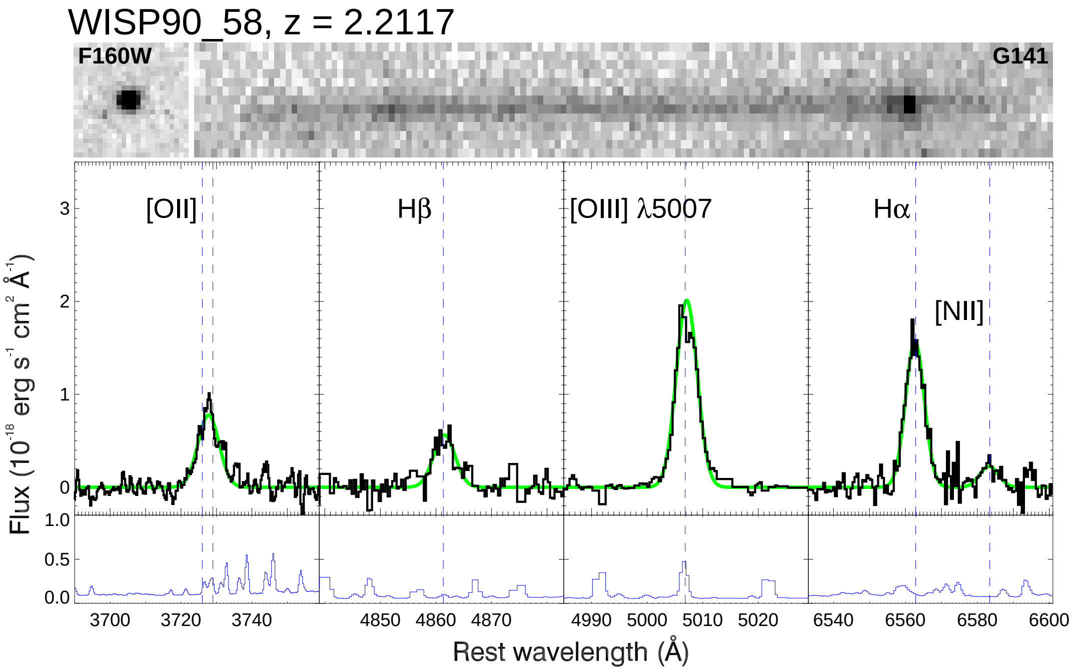

WISP90_58, z = 2.2117
F160W
G141
[OII]
Hβ
[OIII] λ5007
Hα
[NII]
Flux (10^-18 erg s^-1 cm^2 Å^-1)
Rest wavelength (Å)

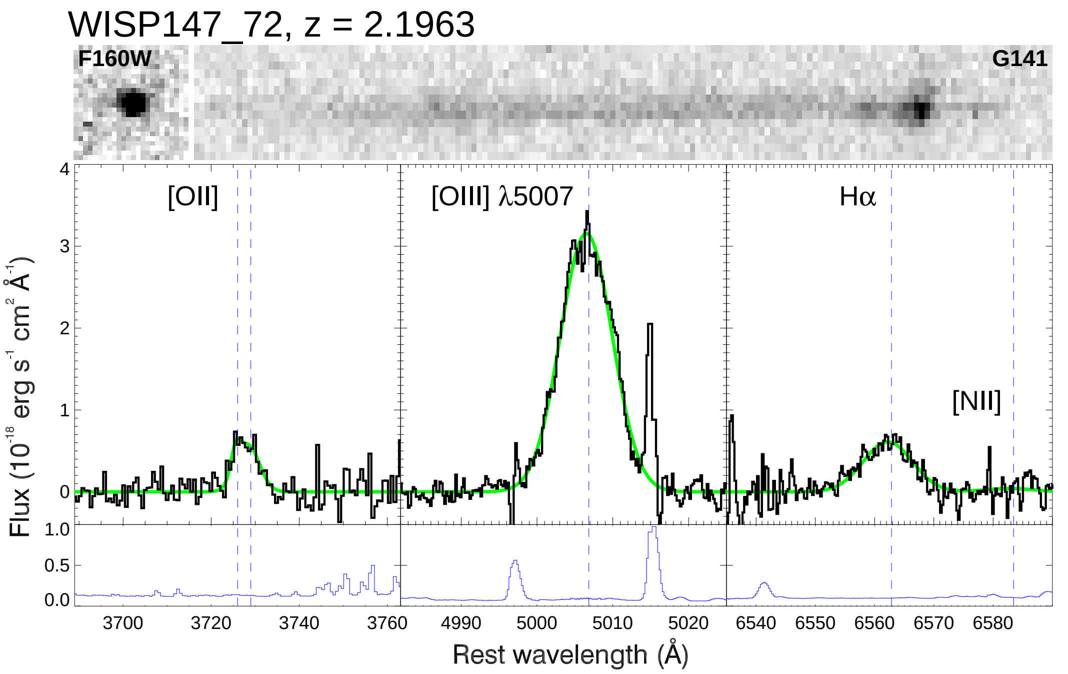

WISP147_72, z = 2.1963
F160W
G141
[OII]
[OIII] λ5007
Hα
[NII]
Flux (10^-18 erg s^-1 cm^2 Å^-1)
Rest wavelength (Å)

Figure B.4

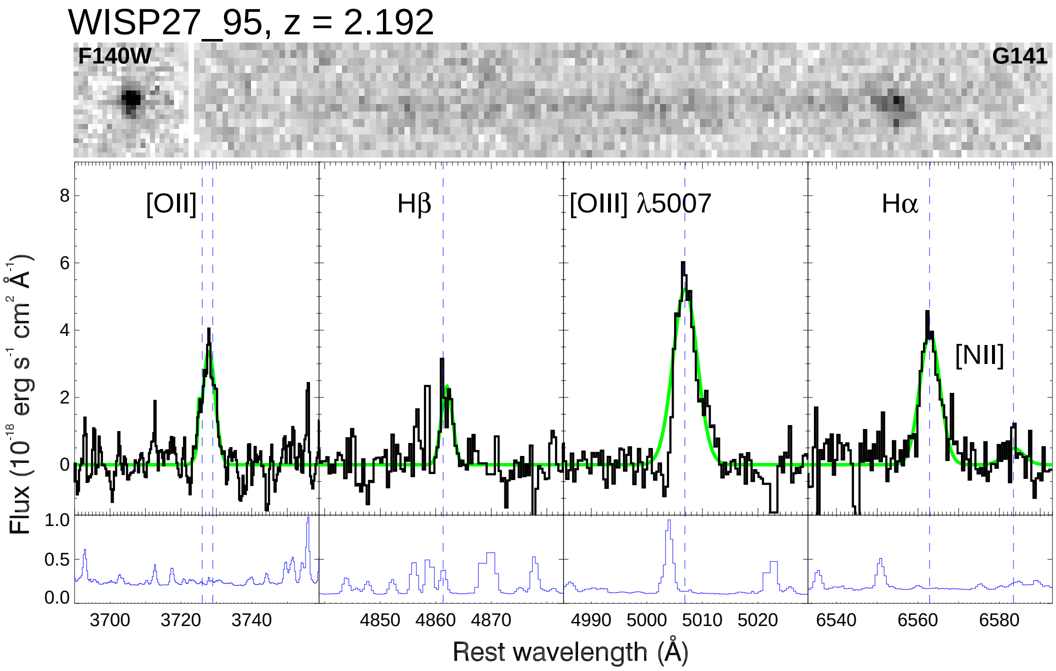
WISP27_95, z = 2.192
F140W
G141
[OII]
Hβ
[OIII] λ5007
Hα
[NII]
Flux (10^{-18} erg s^{-1} cm^{2} Å^{-1})
Rest wavelength (Å)

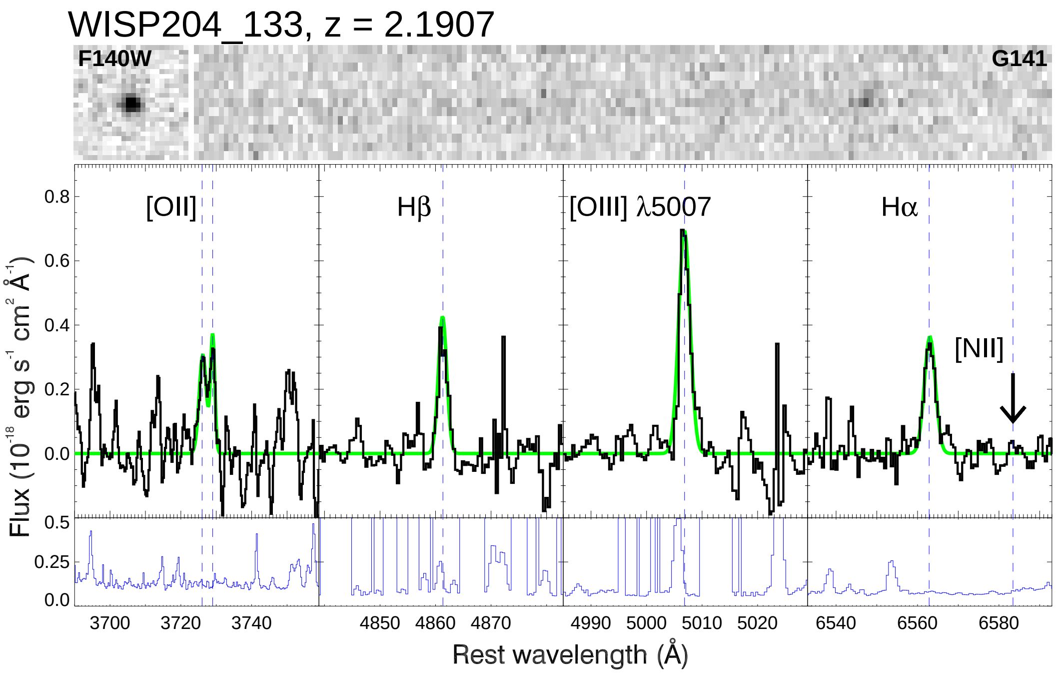
WISP204_133, z = 2.1907
F140W
G141
[OII]
Hβ
[OIII] λ5007
Hα
[NII]
Flux (10^{-18} erg s^{-1} cm^{2} Å^{-1})
Rest wavelength (Å)

Figure B.5

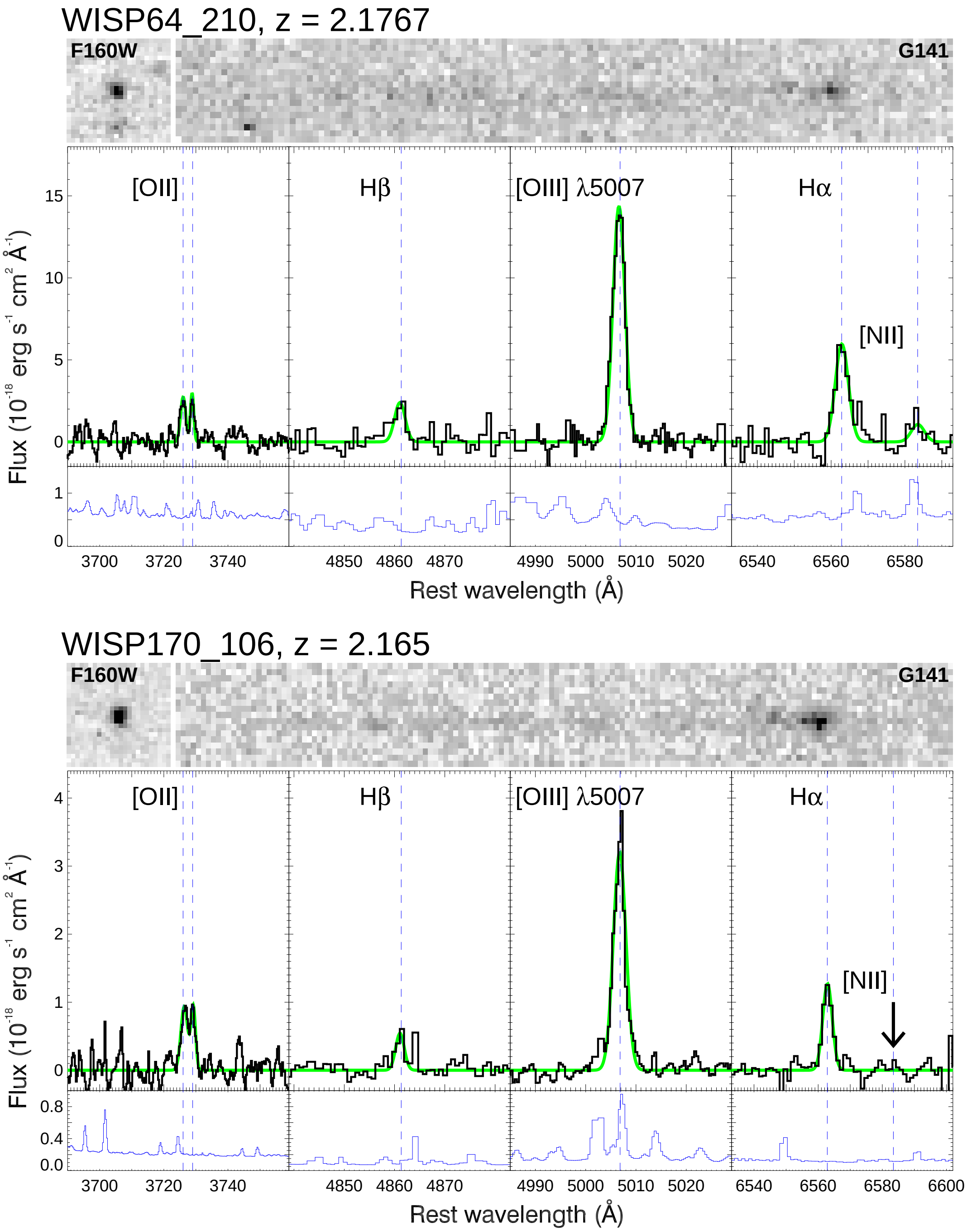

WISP64_210, z = 2.1767
F160W
G141
[OII]
Hβ
[OIII] λ5007
Hα
[NII]
Flux (10^-18 erg s^-1 cm^2 Å^-1)
Rest wavelength (Å)
WISP170_106, z = 2.165
F160W
G141
[OII]
Hβ
[OIII] λ5007
Hα
[NII]
Flux (10^-18 erg s^-1 cm^2 Å^-1)
Rest wavelength (Å)

Figure B.6

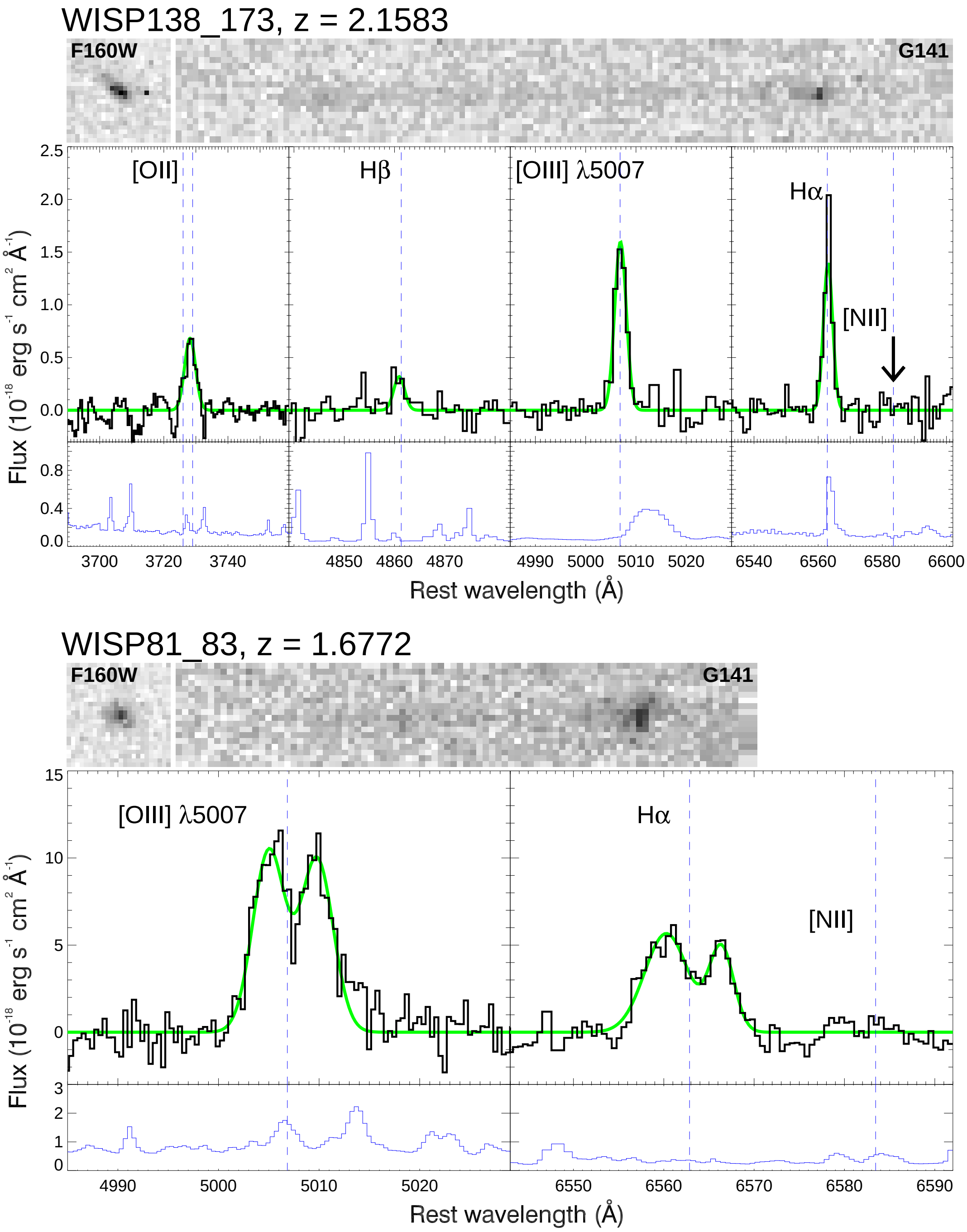
WISP138_173, z = 2.1583
F160W
G141
[OII]
Hβ
[OIII] λ5007
Hα
[NII]
Flux (10^-18 erg s^-1 cm^2 Å^-1)
Rest wavelength (Å)
WISP81_83, z = 1.6772
F160W
G141
[OIII] λ5007
Hα
[NII]
Flux (10^-18 erg s^-1 cm^2 Å^-1)
Rest wavelength (Å)

Figure B.7

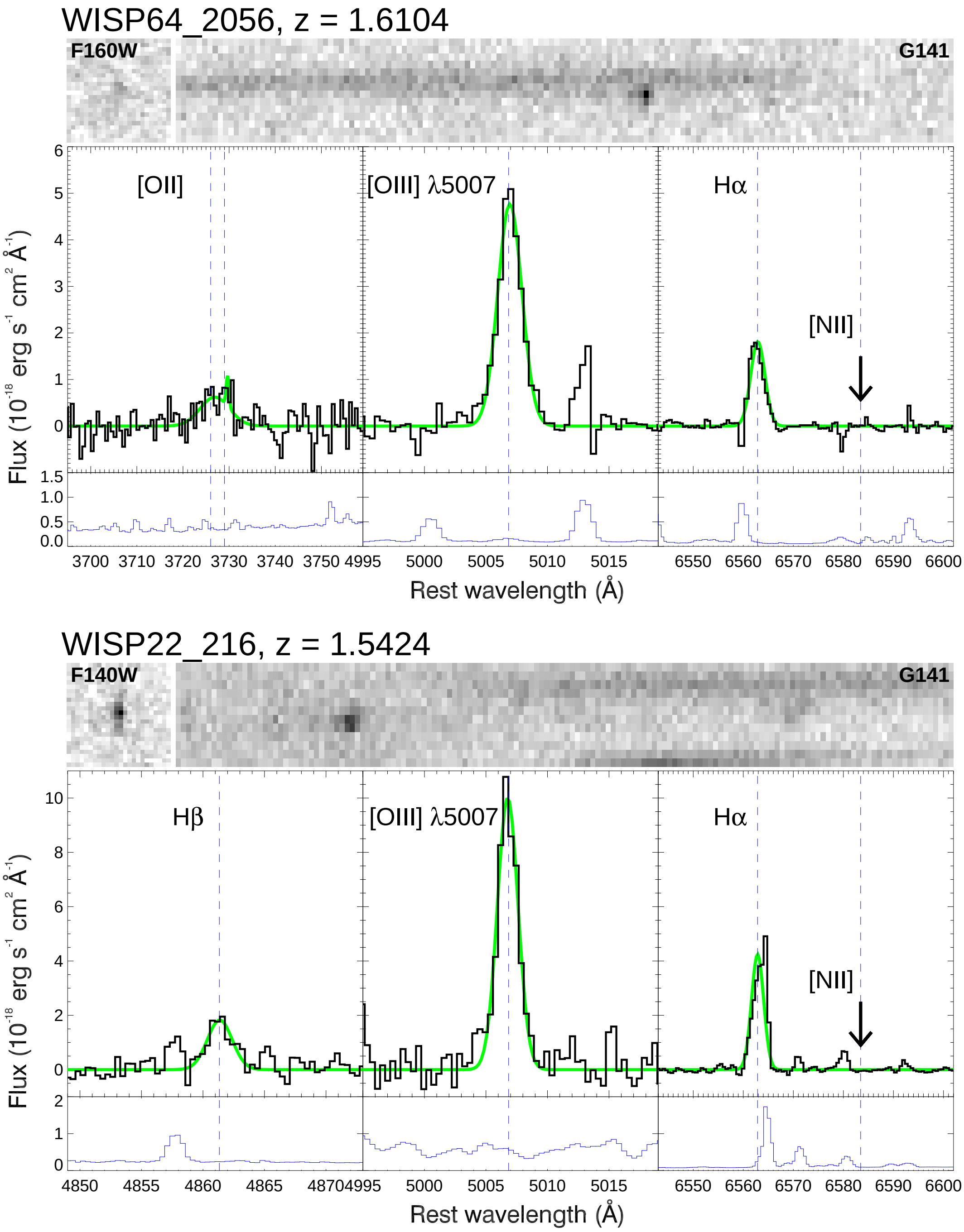
WISP64_2056, z = 1.6104
F160W
G141
[OII]
[OIII] λ5007
Hα
[NII]
Flux (10^-18 erg s^-1 cm^2 Å^-1)
Rest wavelength (Å)
WISP22_216, z = 1.5424
F140W
G141
Hβ
[OIII] λ5007
Hα
[NII]
Flux (10^-18 erg s^-1 cm^2 Å^-1)
Rest wavelength (Å)

Figure B.8

Hα

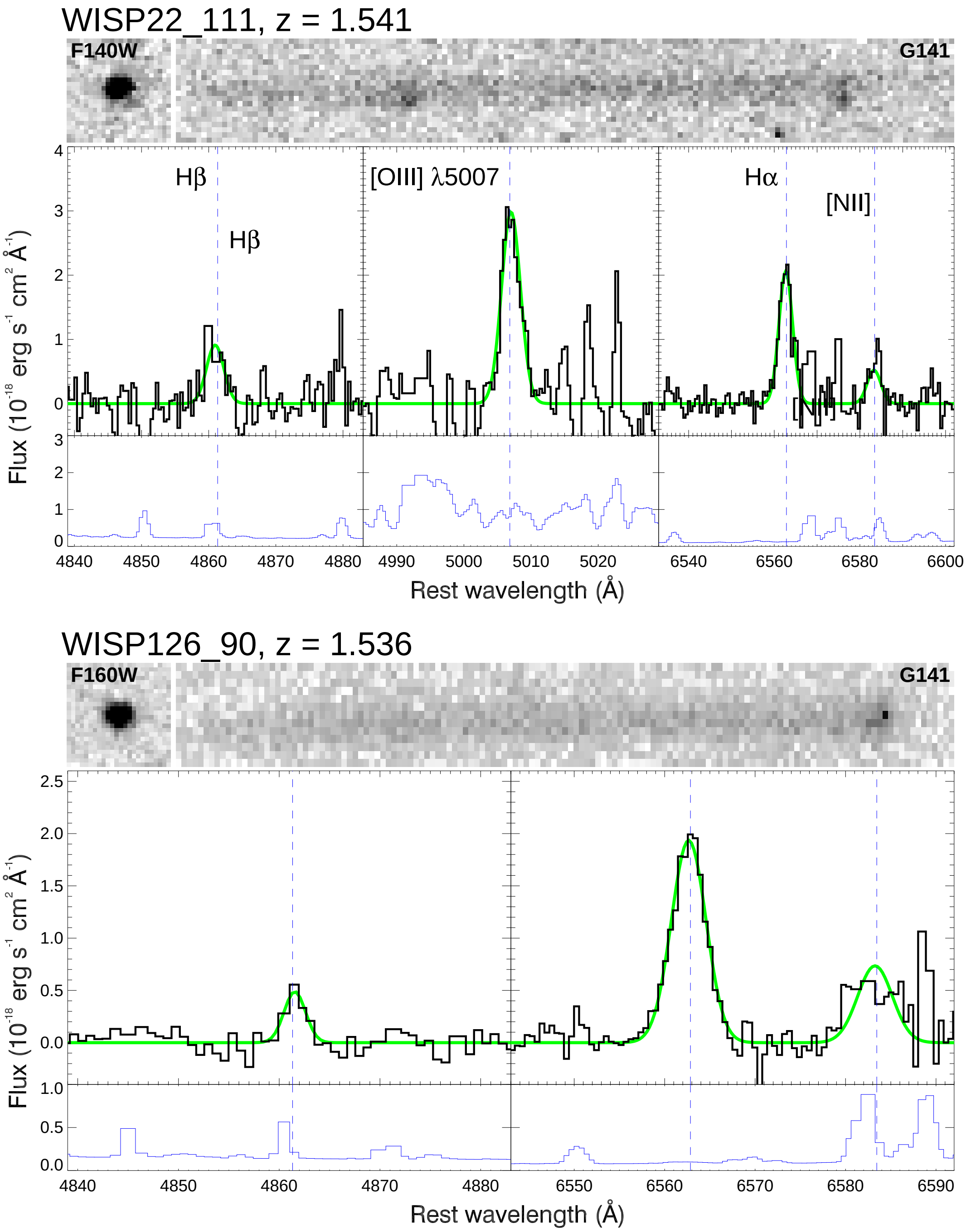
WISP22_111, z = 1.541
F140W
G141
Hβ
Hβ
[OIII] λ5007
Hα
[NII]
Flux (10^-18 erg s^-1 cm^2 Å^-1)
Rest wavelength (Å)
WISP126_90, z = 1.536
F160W
G141
Flux (10^-18 erg s^-1 cm^2 Å^-1)
Rest wavelength (Å)

Figure B.9

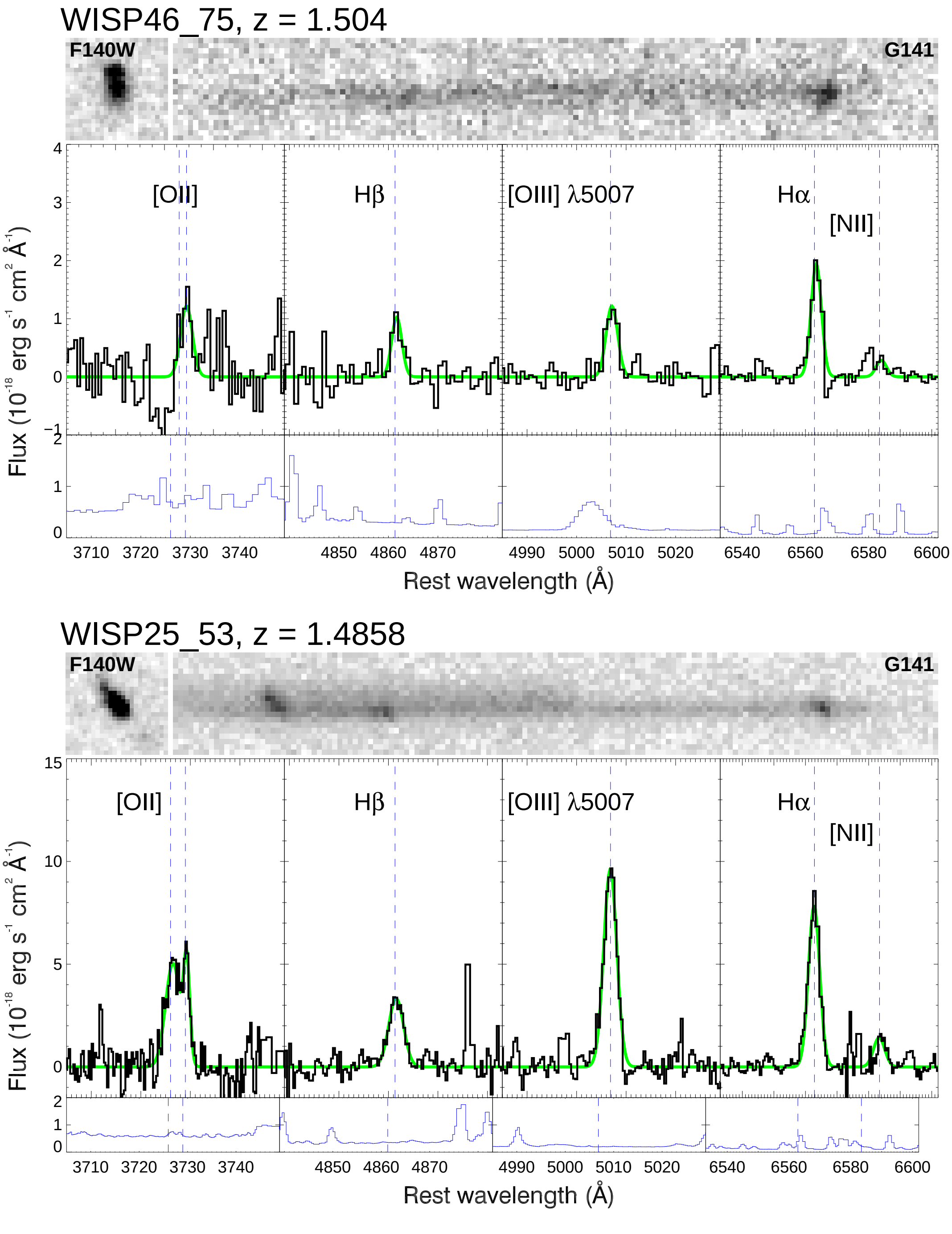

WISP46_75, z = 1.504
F140W
G141
[OII]
Hβ
[OIII] λ5007
Hα
[NII]
Flux (10⁻¹⁸ erg s⁻¹ cm² Å⁻¹)
Rest wavelength (Å)
WISP25_53, z = 1.4858
F140W
G141
[OII]
Hβ
[OIII] λ5007
Hα
[NII]
Flux (10⁻¹⁸ erg s⁻¹ cm² Å⁻¹)
Rest wavelength (Å)

Figure B.10

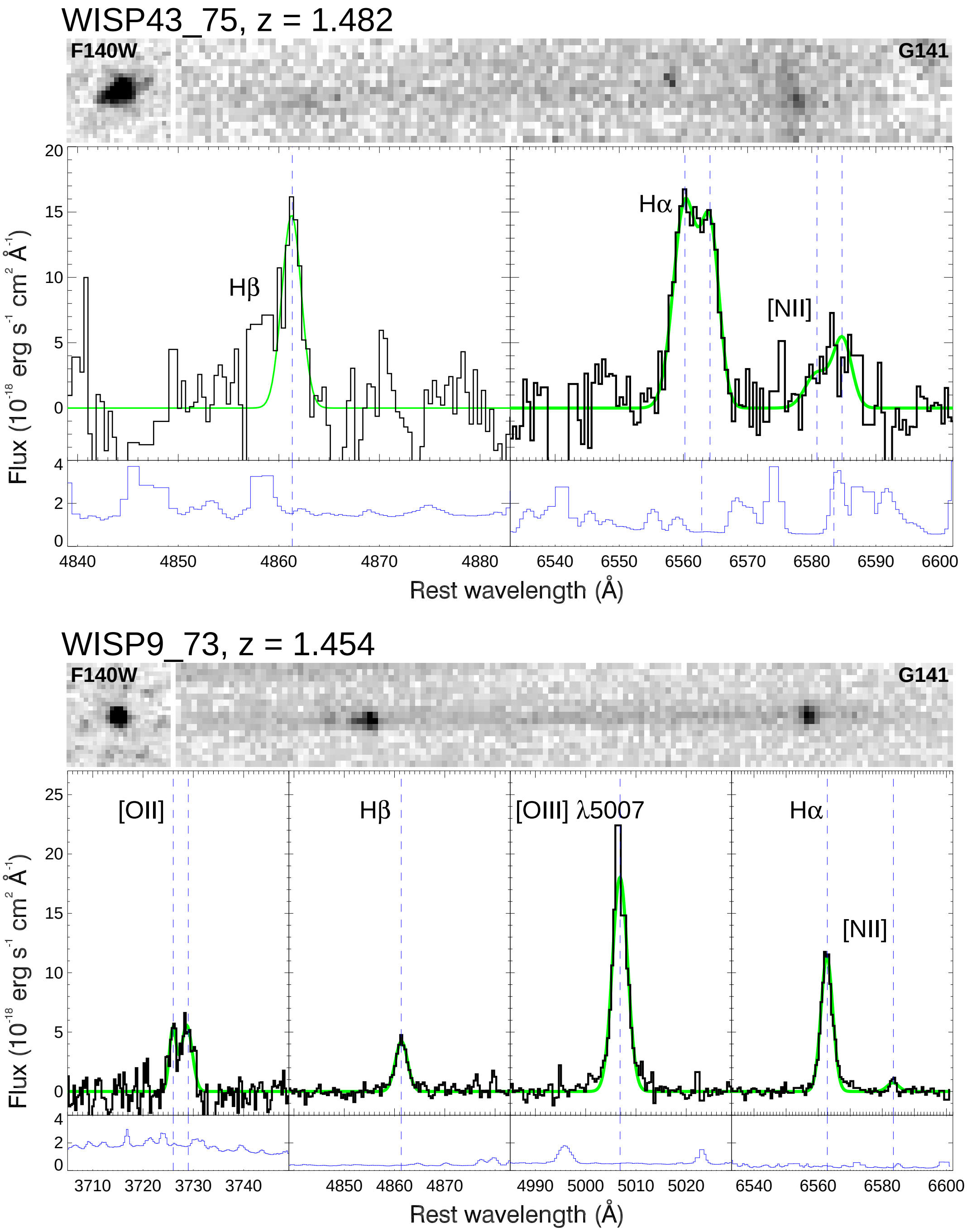
WISP43_75, z = 1.482
F140W
G141
Hβ
Hα
[NII]
Flux (10^-18 erg s^-1 cm^2 Å^-1)
Rest wavelength (Å)
WISP9_73, z = 1.454
F140W
G141
[OII]
Hβ
[OIII] λ5007
Hα
[NII]
Flux (10^-18 erg s^-1 cm^2 Å^-1)
Rest wavelength (Å)

Figure B.11

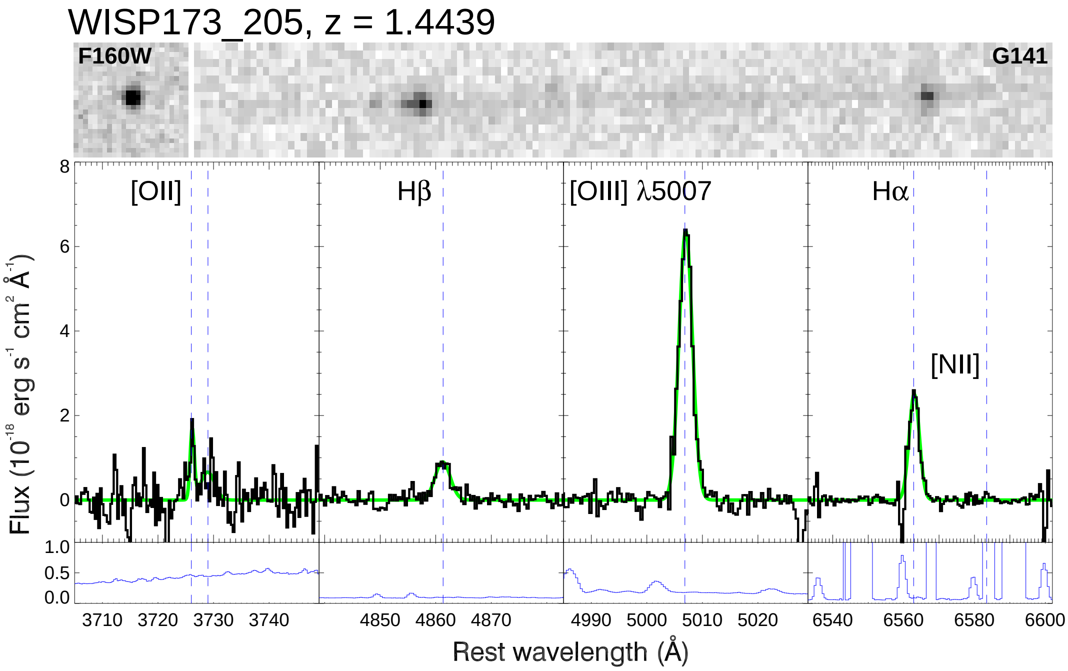
WISP173_205, z = 1.4439
F160W
G141
[OII]
Hβ
[OIII] λ5007
Hα
[NII]
Flux (10^-18 erg s^-1 cm^2 Å^-1)
Rest wavelength (Å)

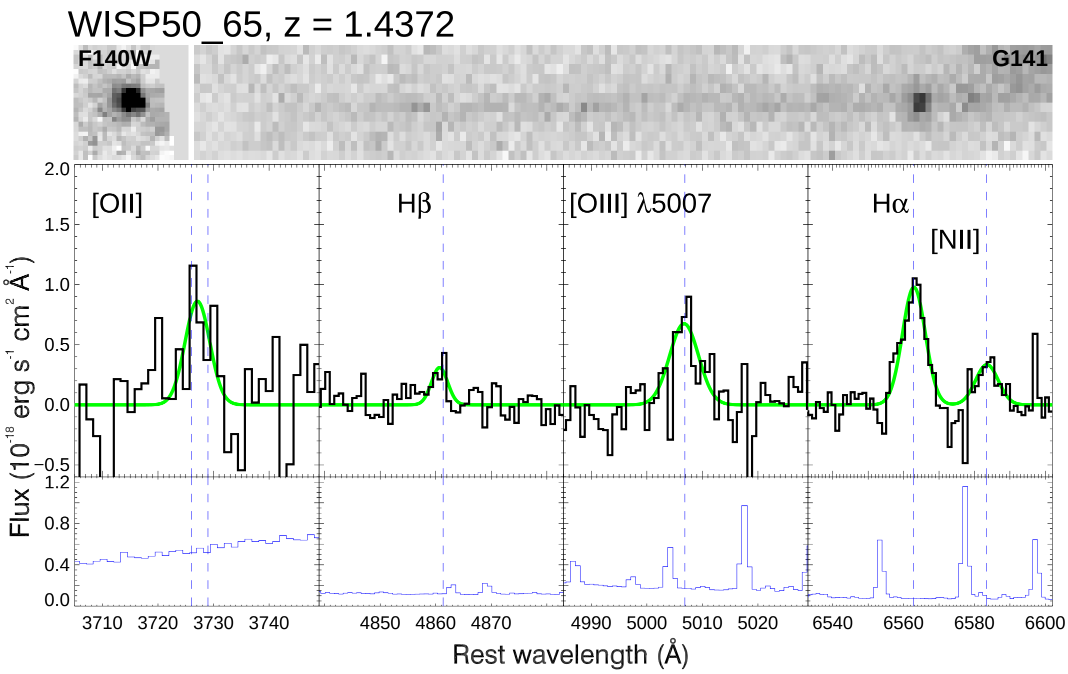
WISP50_65, z = 1.4372
F140W
G141
[OII]
Hβ
[OIII] λ5007
Hα
[NII]
Flux (10^-18 erg s^-1 cm^2 Å^-1)
Rest wavelength (Å)

Figure B.12

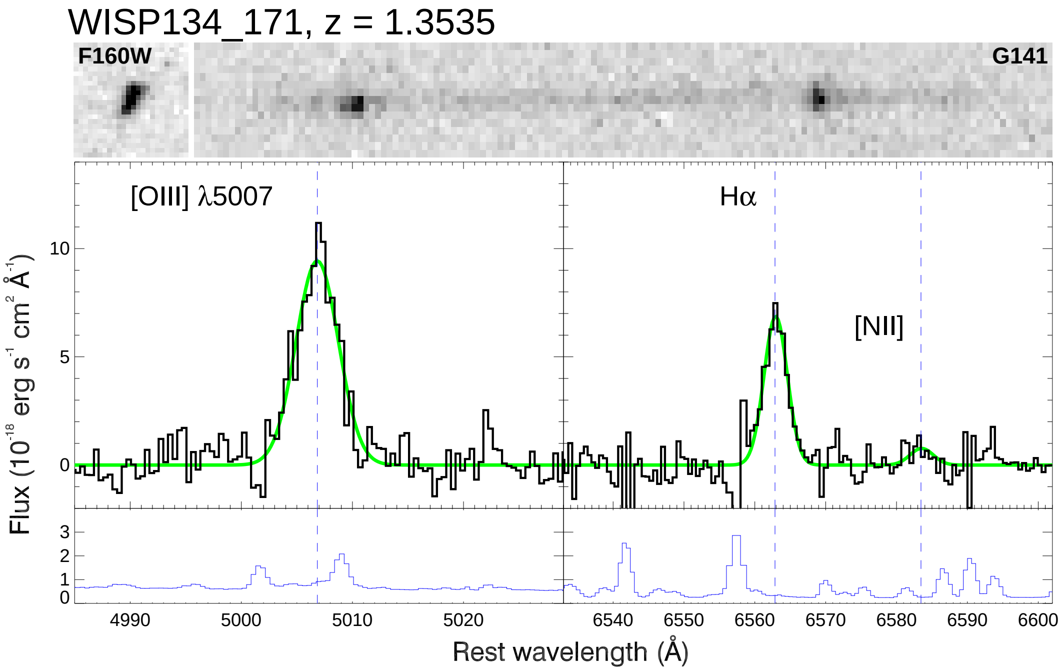
WISP134_171, z = 1.3535
F160W
G141
[OIII] λ5007
Hα
[NII]
Flux (10^-18 erg s^-1 cm^2 Å^-1)
Rest wavelength (Å)

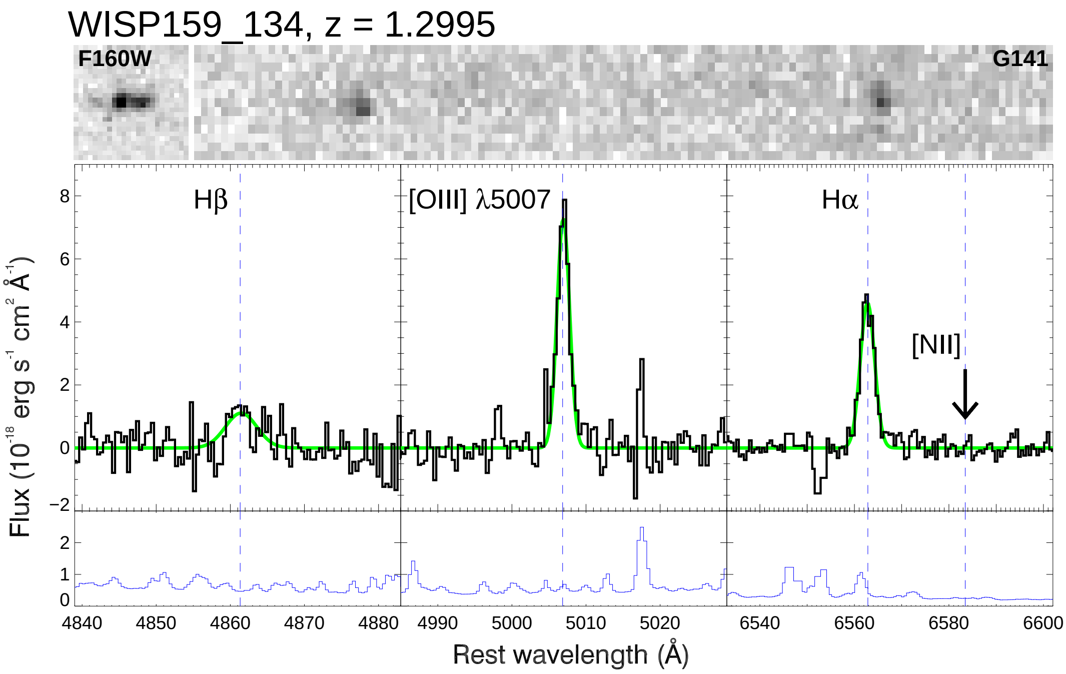
WISP159_134, z = 1.2995
F160W
G141
Hβ
[OIII] λ5007
Hα
[NII]
Flux (10^-18 erg s^-1 cm^2 Å^-1)
Rest wavelength (Å)

Figure B.13